MODEL PREDICTIVE CONTROL OF ENERGY SYSTEMS FOR HEAT AND

POWER APPLICATIONS

By

Chethan Ramakrishna Reddy

A DISSERTATION

Submitted in partial fulfillment of the requirements for the degree of

DOCTOR OF PHILOSOPHY

In Mechanical Engineering-Engineering Mechanics

MICHIGAN TECHNOLOGICAL UNIVERSITY

2022

This dissertation has been approved in partial fulfillment of the requirements for the Degree of DOCTOR OF PHILOSOPHY in Mechanical Engineering-Engineering Mechanics.

Department of Mechanical Engineering-Engineering Mechanics

Dissertation Co-advisor: *Dr. Mahdi Shahbakhti*

Dissertation Co-advisor: *Dr. Wayne W. Weaver*

Committee Member: *Dr. Rush D. Robinett III*

Committee Member: *Dr. Kuilin Zhang*

Department Chair: *Dr. William W. Predebon*

Dedication

To Sowmya

without whom I would neither be who I am nor would this work be what it is today.

Contents

List of Figures

List of Tables

Preface

The manuscript and the results of this dissertation are mainly based on four published journal papers, one journal paper being prepared and four conference papers (Appendix C). Publishers of these papers have granted the permissions found in Appendix E. The contribution of the author of this dissertation as well as the contributions of the co-authors for each of the papers are as follows:

† Contribution for Chapter 2 [1, 2, 3, 4, 5, 6]: The energy based models of the MicroCSP was partly developed and validated by the author of this dissertation Chethan R Reddy. While, the rest of the energy based model development and validation was done by Dr Mohamed Toub, alumni of Mohammed V University (Advised by Dr. Ghassane Aniba) in Morocco and a former visiting scholar to MTU (Co-hosted by Dr. Mahdi Shahbakhti and Dr. Rush Robinett). The energy based building HVAC system model was developed and validated by Dr. Meysam Razmara, alumni of MTU (Co-advised by Dr. Mahdi Shahbakhti and Dr. Rush Robinett). Energy based model predictive control and the energy cost based model predictive control of the combined building HVAC + MicroCSP system was collaboratively designed and analysed by Chethan R. Reddy and Dr. Mohamed Toub.

The exergy based models of the building HVAC system and MicroCSP was developed by Chethan R Reddy. Additionally, the exergy based model predictive control of the combined building HVAC + MicroCSP system was designed and analysed by Chethan R. Reddy. Dr. Mahdi Shahbakhti and Dr. Rush Robinett were paramount in directing the research. Additionally, Dr. Mahdi Shahbakhti and Dr. Rush Robinett were involved in giving technical, and non-technical comments during the course of writing the papers.

† Contribution for Chapter 3 [7, 8]: The energy and exergy based models of the dual fuel ICE and WHR systems was developed and validated by Chethan R Reddy. The data required for the model development and validation of the dual fuel ICE was set-up, measured and provided by Vinicius Bonfochi Vinhaes, a PhD student at MTU (Co-advised by Dr. Mahdi Shahbakhti and Dr. Jeffery D. Naber). Valuable technical know-how of the dual fuel ICE was input from Dr. Mahdi Shahbakhti and Vinicius Bonfochi Vinhaes. Energy based model predictive control and the exergy based model predictive control of the combined ICE + WHR system was designed and analysed by Chethan R. Reddy. Finally, Dr. Mahdi Shahbakhti and Dr. Rush Robinett gave valuable technical, and non-technical comments during the course of writing the papers.

Acknowledgments

I gratefully thank many wonderful individuals who supported me in successful completion of my doctoral dissertation during years of studying at Michigan Tech.

My principal gratitude goes to my PhD advisors, Drs. Mahdi Shahbakhti and Rush D. Robinett III. My advisors provided me with the encouragement, guidance, and mentorship and gave me the opportunity to develop my research background in the field of controls and optimization of energy systems. Dr Mahdi Shahbakhti's enthusiasm for research have motivated me to publish the research results in journal and conference articles. I thank Dr. Rush for his vision, and perpetual zeal for research which motivated me to explore new ideas. Both my PhD advisors facilitated my study by providing financial support during the course of my studies and I am grateful for the same.

Special thanks to Dr. Wayne W. Weaver for agreeing to be my PhD advisor for administrative purposes. I thank Dr. Kuilin Zhang for agreeing to serve on my Dissertation Committee.

I thank Dr. Mohamed Toub (alumni of Mohammed V University in Morocco and a former visiting scholar to MTU (Co-hosted by Dr. Mahdi Shahbakhti and Dr. Rush D. Robinett III)) for his collaboration with me during the initial phases of my research.

Nomenclature

Abbreviations

AHU   Air Handling Unit

CMPC   Energy Cost Based MPC

COP   Coefficient of Performance

CSP   Concentrated Solar Power

DER   Distributed Energy Resource

DNI   Direct Normal Irradiance

DPF   Diesel Particulate Filter

EIA   United States Energy Information Administration

EMPC   Energy Based MPC

EGR   Exhaust Gas Recirculation

ERV   Energy Recovery Ventilator

FLT   First Law of Thermodynamics

GHG   Greenhouse Gas

HE   Heat Exchanger

HP   Heat Pump

HTF   Heat Transfer Fluid

HVAC   Heating, Ventilation, and Air Conditioning

ICE	Internal Combustion Engine
IEA	International Energy Agency
LMP	Locational Marginal Price
MicroCSP	Micro-scale CSP
MPC	Model Predictive Control
MCS	Monte-Carlo Simulations
NG	Natural Gas
ORC	Organic Rankine Cycle
PTC	Parabolic Trough Collectors
PV	Photovoltaic
RBC	Rule Based Control
RCCI	Reactivity Controlled Compression Ignition
SLT	Second Law of Thermodynamics
SOC	State of Charge
TC	Turbocharger
TEG	Thermo-Electric Generator
TES	Thermal Energy Storage
WF	Working Fluid
WHR	Waste Heat Recovery
XMPC	Exergy-based MPC

Symbols

θ Incidence angle (rad)

δ Declination angle (rad)

ω Hour angle (rad)

θ_z Zenith angle (rad)

ϕ Latitude angle (rad)

n Day number (-)

L Meridian (rad)

ET Equation of time (rad)

$\dot{Q}$ Thermal power (W)

η Efficiency (-)

IAM Incidence angle modifier (-)

A_p Area of aperture of collector in PTC (m^2)

k Heat loss co-efficient of PTC (-)

T Temperature (K)

P Power (W)

E Energy (J)

ρ Density (kg/m^3)

C Capacity of TES (J)

Tq Torque (Nm)

p	Pressure (Pa)
γ	Compression Ratio (-)
A_s	Surface area of HE (m^2)
α	Weight factor for optimizing soft constraints (-)
$\dot{m}$	Mass flow rate (kg/s)
h	Specific enthalpy (J/kg.K)
s	Specific entropy (J/kg.K)
c_p	Constant pressure specific heat (J/kg.K)
c_v	Constant volume specific heat (J/kg.K)
$\dot{X}$	Rate of exergy (W)
X	Exergy (J)
I_e	Energy consumed (J)
λ_F	Power coefficient of HVAC ventilation fan (W.s^3/kg^3)
N_{zones}	Number of zones (-)
ERE	Energy recovery effectiveness (-)
r_p	Pressure ratio (-)
$[k]$	Time index "k" (-)
HV	Heating Value (J/kg)
AFR	Air-Fuel Ratio (-)
$DIPr$	Diesel Injection Pressure (MPa)

DSR Diesel Substitution Ratio (%)

MAP Manifold Absolute Pressure (kPa)

SOI Diesel Start of Injection (^{o}bTDC)

ω Angular Speed (rad/s)

U Overall Heat Transfer Co-efficient (W/m^2.K)

Subscripts

o   Optics for Parabolic Trough Collectors (PTC)

gain   Gained by the PTC

loss   Losses in the PTC

gen   Generator

in   Inlet

amb   Ambient

out   Outlet

ev   Evaporator in the ORC

con   Condenser in the ORC

i   Thermal zone number

dest   Destruction

rec   Recovered

sup   Supplied

t   Time

t+k|t k^{th} prediction evaluated at time t

gb   Gearbox

elec   Electrical

int   Intake of engine

exh   Exhaust of engine

amb   Ambient

isen   Isentropic

mech   Mechanical

Superscripts

r   Room

v   Ventilation

H   Heating

b   Building

F   Fan

Su   Supply to room

in   Inlet

out   Outlet

c   Compressor in TC

tb   Turbine in TC

e   Expander in ORC

pu   Pump in ORC

Abstract

Building and transportation sectors together account for two-thirds of the total energy consumption in the US. There is a need to make these energy systems (i.e., buildings and vehicles) more energy efficient. One way to make grid-connected buildings more energy efficient is to integrate the heating, ventilation and air conditioning (HVAC) system of the building with a micro-scale concentrated solar power (MicroCSP) system. Additionally, one way to make vehicles driven by internal combustion engine (ICE) more energy efficient is by integrating the ICE with a waste heat recovery (WHR) system. But, both the resulting energy systems need a smart supervisory controller, such as a model predictive controller (MPC), to optimally satisfy the energy demand. Consequently, this dissertation centers on development of models and design of MPCs to optimally control the combined (i) building HVAC system and the MicroCSP system, and (ii) ICE system and the WHR system.

In this PhD dissertation, MPCs are designed based on the (i) First Law of Thermodynamics (FLT), and (ii) Second Law of Thermodynamics (SLT) for each of the two energy systems. Maximizing the FLT efficiency of an energy system will minimise energy consumption of the system. MPC designed based on FLT efficiency are denoted as energy based MPC (EMPC). Furthermore, maximizing the SLT efficiency of the energy system will maximise the available energy for a given energy input and

a given surroundings. MPC designed based on SLT efficiency are denoted as exergy based MPC (XMPC).

Optimal EMPC and XMPC are designed and applied to the combined building HVAC and MicroCSP system. In order to evaluate the designed EMPC and XMPC, a common rule based controller (RBC) was designed and applied to the combined building HVAC and MicroCSP system. The results show that the building energy consumption reduces by 38% when EMPC is applied to the combined MicroCSP and building HVAC system instead of using the RBC. XMPC applied to the combined MicroCSP and building HVAC system reduces the building energy consumption by 45%, compared to when RBC is applied.

Optimal EMPC and XMPC are designed and applied to the combined ICE and WHR system. The results show that the fuel consumption of the ICE reduces by 4% when WHR system is added to the ICE and when RBC is applied to both ICE and WHR systems. EMPC applied to the combined ICE and WHR system reduces the fuel consumption of the ICE by 6.2%, compared to when RBC is applied to ICE without WHR system. XMPC applied to the combined ICE and WHR system reduces the fuel consumption of the ICE by 7.2%, compared to when RBC is applied to ICE without WHR system.

Chapter 1

Introduction

One of the major challenges that the world is facing today is climate change. The repercussions of climate change are expected to be devastating in the future compared to what several countries are experiencing currently. Indeed, heat waves, with very high and unprecedented temperatures, struck several countries breaking records and reaching up to 41 °C in South Korea in 2018 [9] and 48 °C in Portugal in 2003 [10]. On the other hand, the lowest temperature ever recorded on earth (-93.2 °C) was reported in Antarctica in 2010 [11]. These extreme weather conditions cause high energy consumption in buildings due to the increased demand for both cooling and heating in order to ensure the temperature comfort of the users. In addition, the increase in world's population [12] and increasing urbanization [12] of the world's population cause high energy consumption in the transportation sector. These lead to

a vicious cycle and a snowball effect that, if not addressed quickly and appropriately, could have drastic consequences on our planet in the near future.

Need for Energy Efficient Programs for Building Sector: The International Energy Agency (IEA) reported that building direct emissions contributed to 28% of the global fossil fuel-based greenhouse gas (GHG) emissions in 2019 [13]. About 45% of the world's primary energy resources are consumed by buildings [14]. Heating, ventilation, and air-conditioning (HVAC) systems are among the most energy-consuming loads in a building and are responsible for 40% of its energy consumption [14]. Furthermore, United States Energy Information Administration (EIA) reports [15] that building sector accounted for two-thirds of the electricity consumed in 2019 in the US. The report further shows that internal combustion engines (ICEs) used for customer-owned electricity generation accounted for 6% of the total electricity used by buildings. The report further predicts that the customer-owned electricity generation in buildings is only going to increase from now till 2050. In addition, authors in reference [16] argue in favor of customer-owned electricity generation when considering the economic feasibility of off-grid electricity usage in rural areas where the grid is not yet extended. Furthermore, ICE based power generators are used as the main back-up electricity source in grid connected buildings [17]. Increasing environmental calamities causing disruption to the power grid makes the 12 billion USD global generator industry stronger [18, 19]. All these demand for optimizing energy usage in (i) building HVAC systems, and (ii) ICE systems and make them energy efficient as

much as possible.

Need for Energy Efficient Programs for Transportation Sector: According to the recent EIA report [15], 31% of the total CO_2 emissions in the US in 2019 was caused by the transportation sector. Furthermore, over 75% of the transportation sector is primarily driven by ICEs (Fig. 1.1(a)). This includes ICEs used in over 90% of light-duty vehicles in 2019 in the US (Fig. 1.1(b)). The report further predicts that in 2050, over 65% of the transportation sector would be primarily driven by ICEs (Fig. 1.1(a)). Hence, minimizing energy usage in ICEs makes an important contribution for energy efficiency programs.

1.1 Building HVAC + Micro-scale Concentrated Solar Power (MicroCSP) System

Solar energy is the principal and most abundant source of clean energy on the planet [20]. Indeed, the total annual energy consumption of the entire world can be met by solar collectors with 20% efficiency, covering a thousandth of the terrestrial sphere [21]. The three main solar-based technologies utilized to harvest solar power are: (i) the photovoltaic (PV) cell technology commonly employed to generate electrical power; (ii) the solar thermal power technology which is mainly used for heat generation; and (iii) the concentrated solar power (CSP) technology that generates

(a) Transportation sector consumption (by fuel).
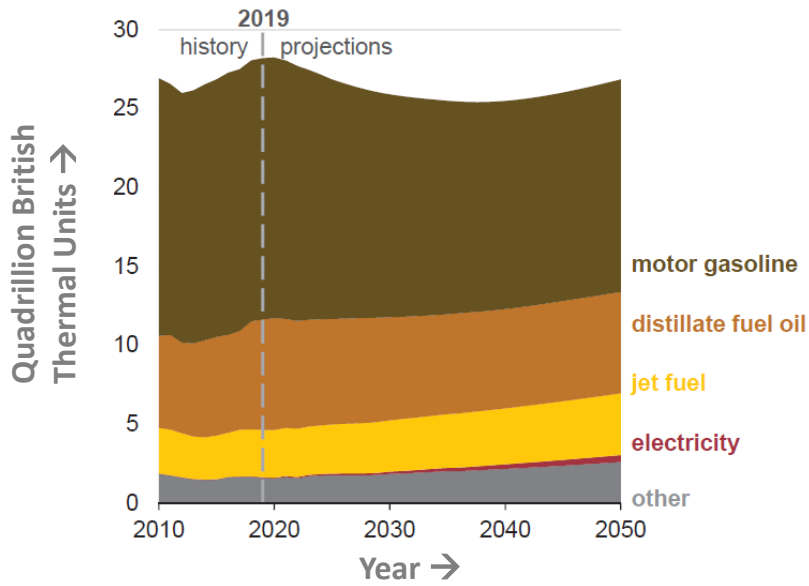
(b) Light-duty vehicle sales by fuel type.
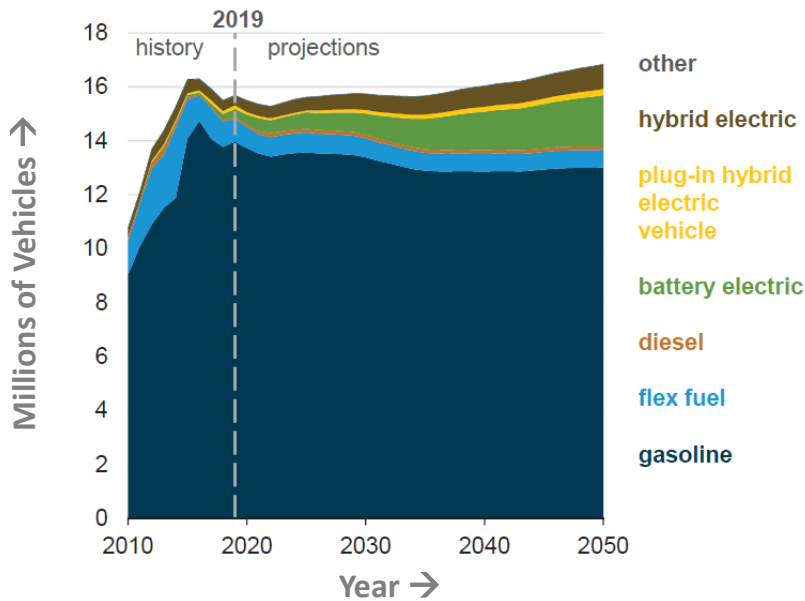
Figure 1.1: Demographics of energy systems in the transportation sector in the USA showing: (a) the contribution of ICE in the transportation sector, (b) the contribution of ICE in light-duty vehicles. (Reprinted from [15]).

both electrical and thermal energy. Figure 1.2 categorizes the solar-assisted HVAC systems into three main categories, based on the solar energy technology utilized in

the system.
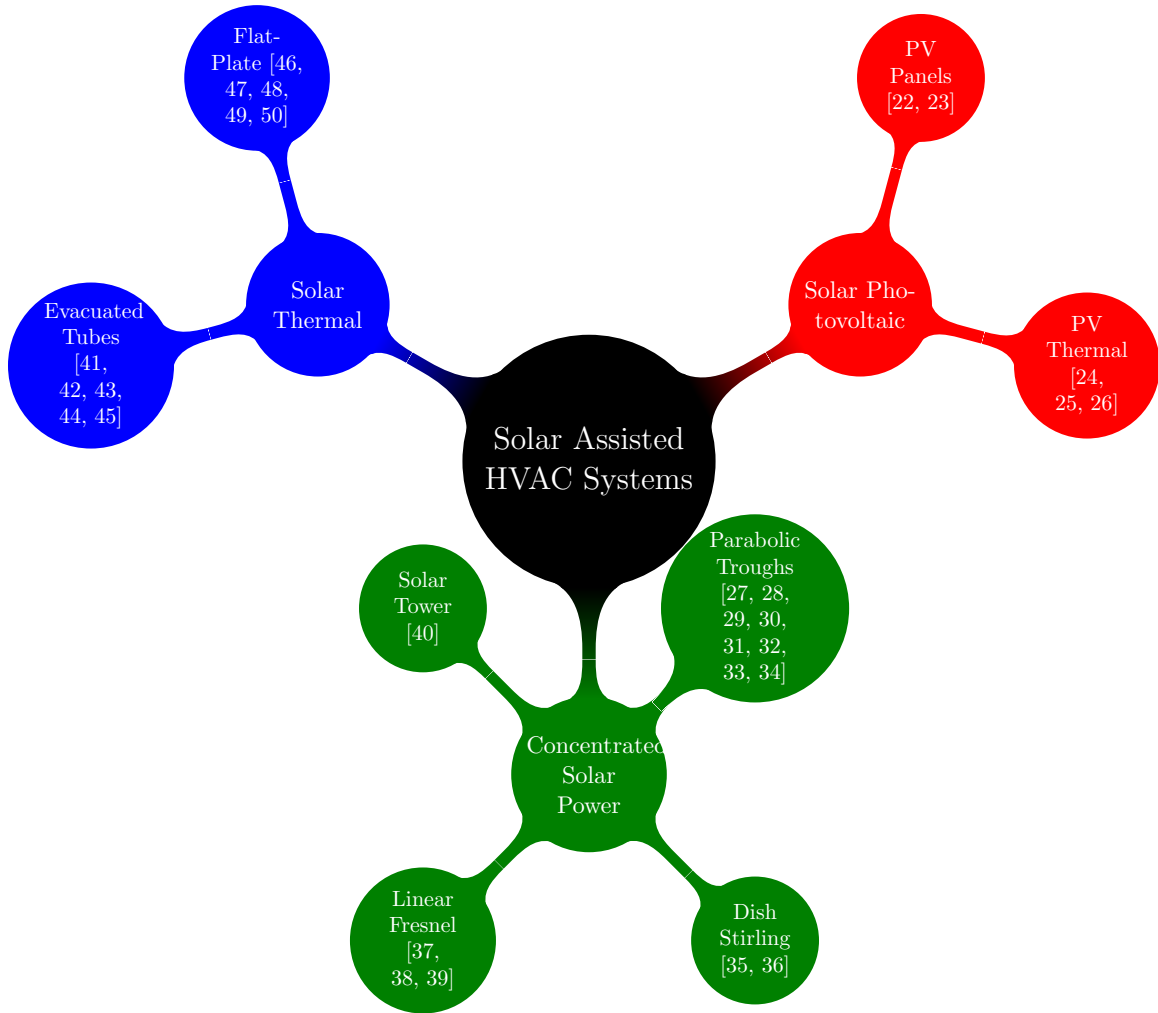
Figure 1.2: Types of solar-assisted HVAC systems for buildings.

CSP systems can provide both electrical power and heating source that offer the most versatility when integrated to building HVAC systems. In addition, downsizing the CSP technology into micro-scale concentrated solar power (MicroCSP) systems with a rated power up to 1 MW [51] offers the advantageous of a distributed energy resource (DER). Indeed, the power engines used in MicroCSP systems are, in most cases, based on the organic Rankine cycle (ORC) that imitates the conventional

Rankine cycle; but, instead of using water as a working fluid, it utilizes an organic fluid to convert low-grade thermal energy into electrical energy [52]. Even though the thermal efficiency of the ORC engine is intrinsically low, the building can harvest the low-grade waste heat of the ORC engine to fulfill the required thermal energy, hence improving the overall efficiency [53]. Moreover, the combination of ORC engines with solar collectors is a good candidate for renewable energy integration into buildings as they are becoming more competitive with PV panels in terms of energy pricing [54]. The authors in reference [3] show that, by integrating MicroCSP into the HVAC system, buildings can save 8% more energy than what they could have saved by using PV.

In a MicroCSP system, solar energy is converted into thermal energy by the parabolic trough collectors (PTC). This collected thermal energy is then stored in the thermal energy storage (TES) before being dispatched into the ORC to be converted into electrical and thermal energies that are used to assist the HVAC system to supply heating or cooling to the building. Figure 1.3 shows the different architectures of the MicroCSP integration into the building HVAC system depending on the use case and heating/cooling demand of the building.

Heating Cogeneration: The MicroCSP system is inherently capable of producing both electricity and heat. This capability can be leveraged for heating applications in buildings by integrating the MicroCSP system into the building HVAC system.
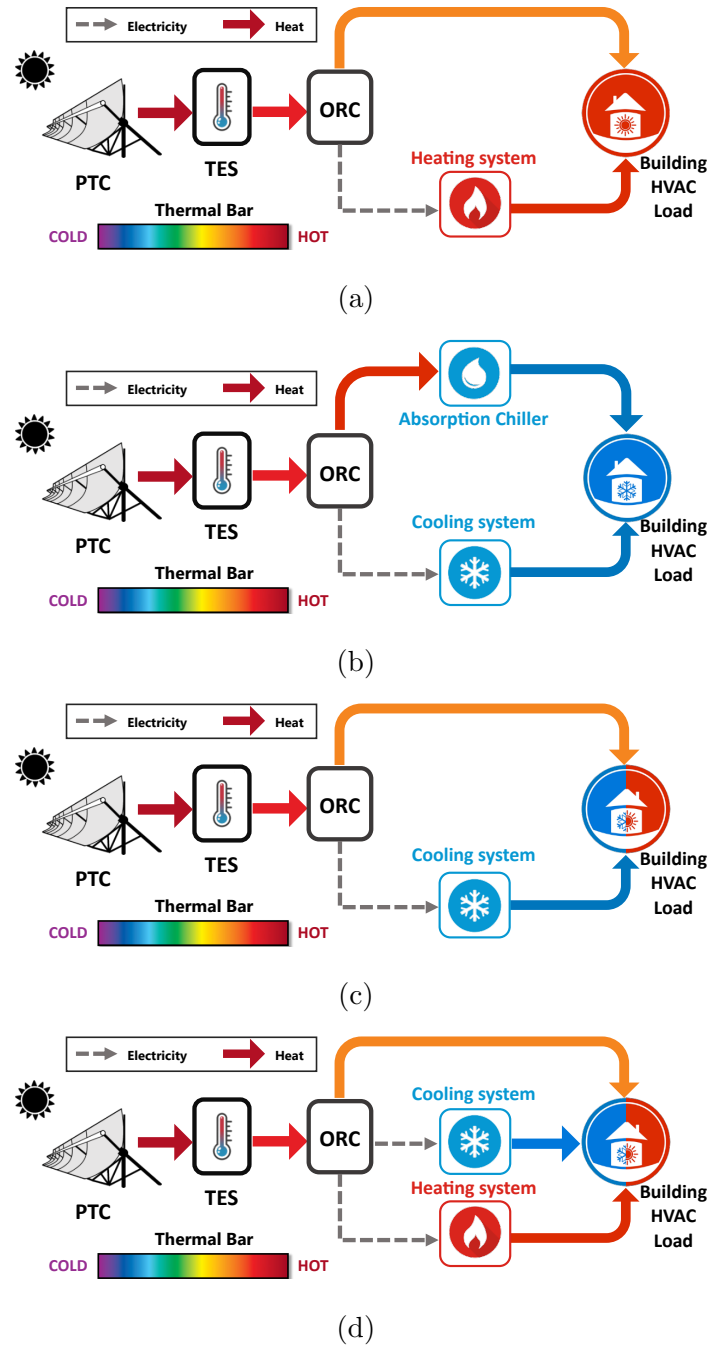
Figure 1.3: Architectures for MicroCSP system integration into building HVAC systems: (a) heating cogeneration architecture, (b) cooling cogeneration architecture, (c) combined heat and cooling cogeneration architecture, and (d) trigeneration architecture.

Indeed, as we can see in Architecture (a) in Figure 1.3, the energy produced in the solar field is stored in the TES before being dispatched to the ORC engine following a specific control strategy. The ORC engine converts the high-temperature heat into electrical energy and cogenerated low-grade thermal energy. The electrical energy can supply heat pumps (HPs) of the HVAC system to provide heating to the building. As per the low-grade cogenerated energy, depending on the set points of the ORC engine, it is either injected directly to heat the building or utilized to preheat the supply air to the HPs.

Cooling Cogeneration: The combined MicroCSP and building HVAC system can also supply cooling to the building, as shown in Architecture (b) in Figure 1.3. In this application, the power produced by the ORC is supplied to the cooling system, while the low-grade heat is used by the absorption chiller [55] to provide cooling to the building.

This architecture tries to exploit the MicroCSP heat cogeneration to increase its overall efficiency. However, to avoid dependency of the cooling loads on the MicroCSP system and solar irradiation, an electricity-driven cooling system is also used and can be supplied by the electricity grid.

Combined Heat and Cooling Cogeneration: In some cases, buildings require both heating and cooling simultaneously. For instance, office buildings with on-premises computer servers and data centers would need cooling for the computing

8

systems and heating for the office rooms in winter. In such a case, the MicroCSP system can be integrated into the building HVAC, as shown in Architecture (c) in Figure 1.3, so that the electricity produced by the ORC is supplied to the HVAC cooling system, while the heat is directly supplied to the building. However, the sizing of the MicroCSP and TES in this application is critical as the heating loads of the building will be entirely dependent on the MicroCSP production and consequently relying on solar irradiation.

Trigeneration: Architecture (d) is proposed as an alternative that improves Architecture (c) and provides both heating and cooling without being completely dependent on MicroCSP production. Indeed, as can be seen in Figure 1.3d, an electricity-driven heating system is added to the system so that the system can be supplied through the electricity grid in case the MicroCSP is not generating sufficient heat.

The four architectures presented in this section are the main system configurations that are employed to leverage the integration of a MicroCSP system into the building HVAC system depending on its applications or needs (heating, cooling, or both). Each architecture is composed of several components that interact with each other and these components need to be controlled so that they can operate optimally.

1.2 Internal Combustion Engine (ICE) + Waste Heat Recovery (WHR) System
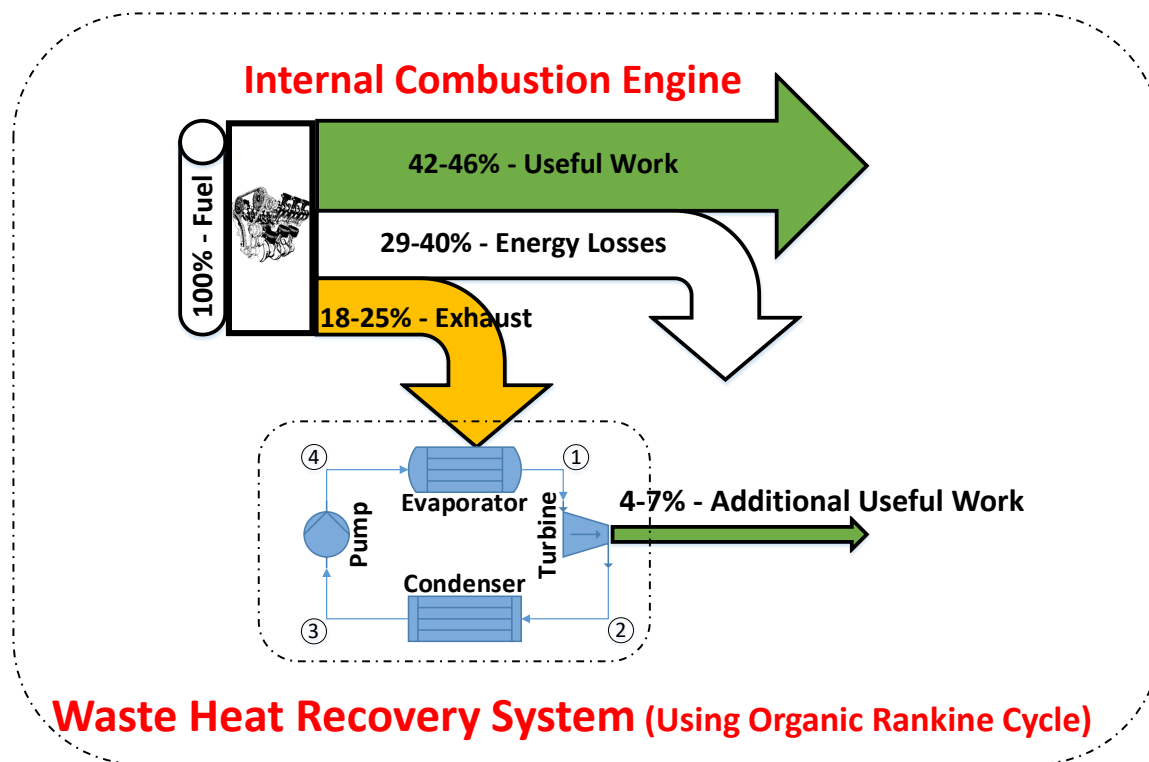
Figure 1.4: Energy balance for a sample combined ICE and WHR system.

Figure 1.4 shows that in an ICE, about one fourth of the input fuel energy is wasted as thermal energy by the exhaust gases leaving the ICE [56]. A waste heat recovery (WHR) system converts this wasted thermal energy to a usable form of energy [57]. In a WHR system, a heat exchanger (HE) transfers the thermal energy from exhaust gas to a heat engine [58] or a thermo-electric generator (TEG) [59]. In a TEG, thermal energy is directly converted to electricity using semi-conductors. The heat

engine generally used in WHRs is an ORC device which converts thermal energy to mechanical energy. The choice of the prime mover in a WHR system is mainly dictated by the size and the operating temperatures of the ICE [60]. This dissertation focuses on an ORC driven WHR system owing to the size of the ICE used in this work.

1.3 Model Predictive Control (MPC) of Energy Systems

Optimal control strategies are required to fully utilize the potential of the two energy systems including building HVAC integrated with MicroCSP, and IC engine with WHR. Model predictive controller (MPC) is an optimal controller which offers versatility in the control of energy systems [61, 62].

Figure 1.5(a) shows the general structure of an MPC framework for an energy system like an ICE or an HVAC system. Additionally, Figure 1.5(b) shows control strategy of the MPC. Figure 1.5 shows that the MPC framework provides a real-time and future optimal solutions to the energy system. The optimal solutions are calculated such that (i) the predicted error between the reference input and the plant output is reduced, (ii) the predicted objective function reaches the minimum (or maximum) value; and (iii) the actuator, and system limits are not breached.
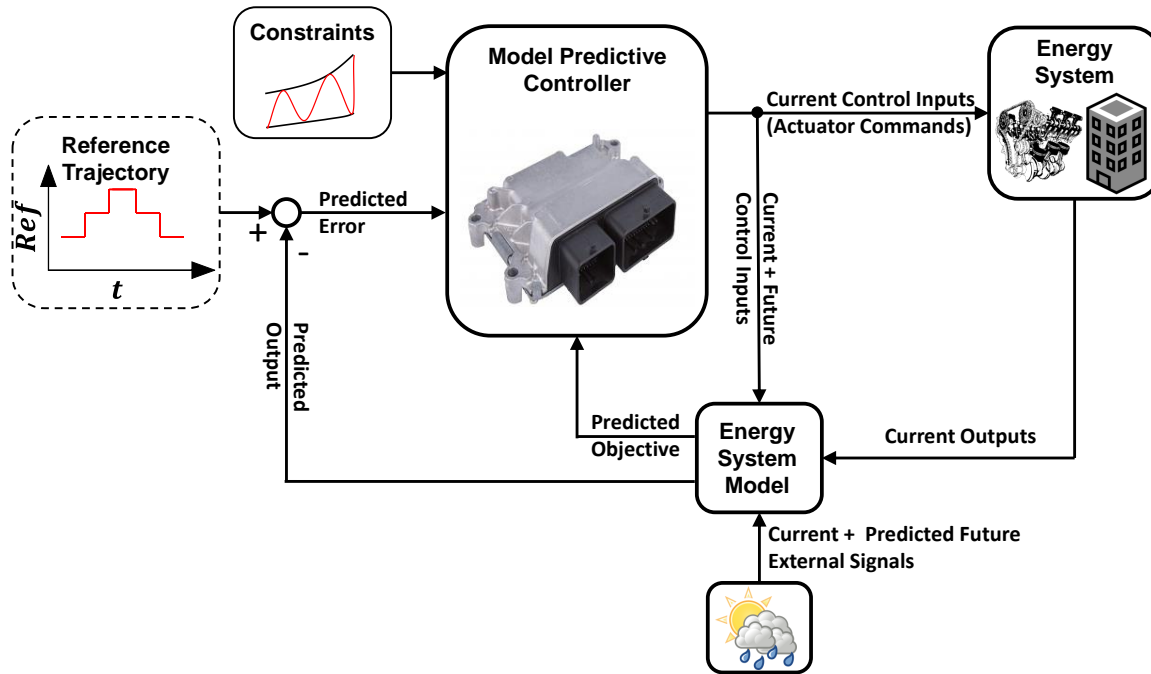
(a)
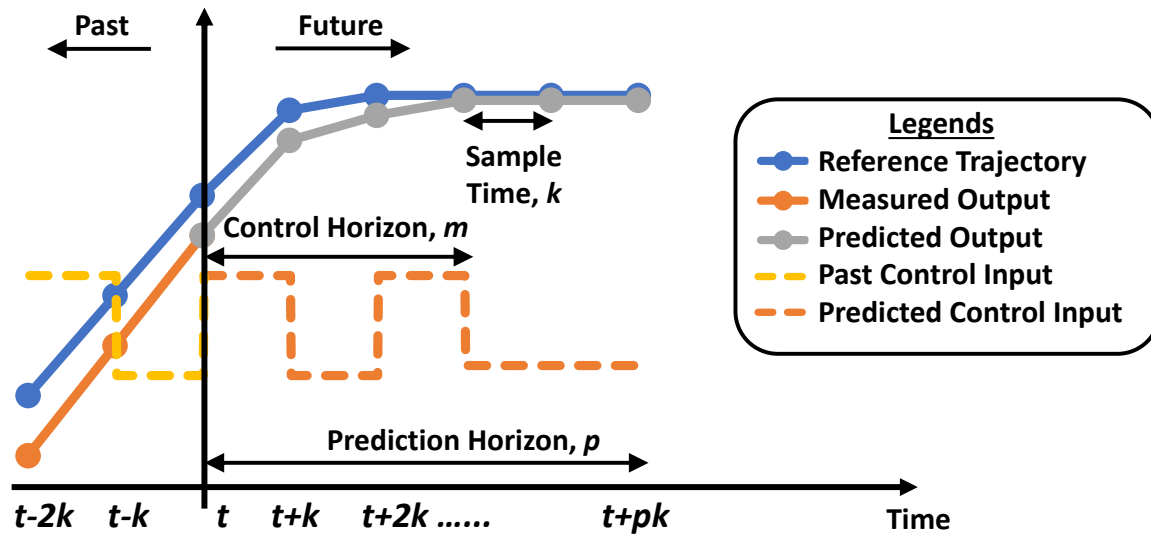
(b)

Figure 1.5: Fundamentals of MPC showing: (a) the general schematic of an MPC framework for an ICE or an HVAC system, (b) the graphical representation of MPC principles with key indicators.

The predicted error is calculated as the difference between the current + future predicted reference trajectory and the predicted plant output. The predicted energy system output and the predicted objective function is calculated in the energy system model. The energy system model considers the (i) current system outputs, (ii) current + future predictions of the control inputs, (iii) current + future predictions of external signals (e.g., solar irradiation, ambient temperature, etc). It is worth noting that, the prediction time of the reference trajectory and the external signals dictates the time for the output, error, objective, and control inputs predictions. This time is termed as the "prediction horizon" denoted by p in Fig. 1.5(b). The time for MPC to reach the optimal control value is termed as the "control horizon" denoted by m in Fig. 1.5(b). The time between two subsequent MPC calculations is termed as the "sample time" denoted by k.

Different MPC methods have been developed to cater to a broad range of industry applications of MPC control. Figure 1.6 shows the different types of MPC methods depending on the (i) solution method [63, 64, 65], (ii) uncertainties in the system [66, 67, 68, 69], (iii) dynamics of the system [70, 71, 72], and (iv) scale of the system [73, 74]. Additionally, MPCs have been successfully utilized for optimal control of building HVAC systems [75] with heat pumps [76], vapor compression systems [77], chillers [78], PV panels and batteries [22, 79]. MPC has also been used for the optimal control of IC engines [80] in spark ignition [81], compression ignition (diesel) [82, 83],

reactivity controlled compression ignition (RCCI) [84] combustion modes. Additionally, a detailed literature review for the application of MPC for building HVAC, ICE, and WHR systems are provided in Chapters 2 and 3.
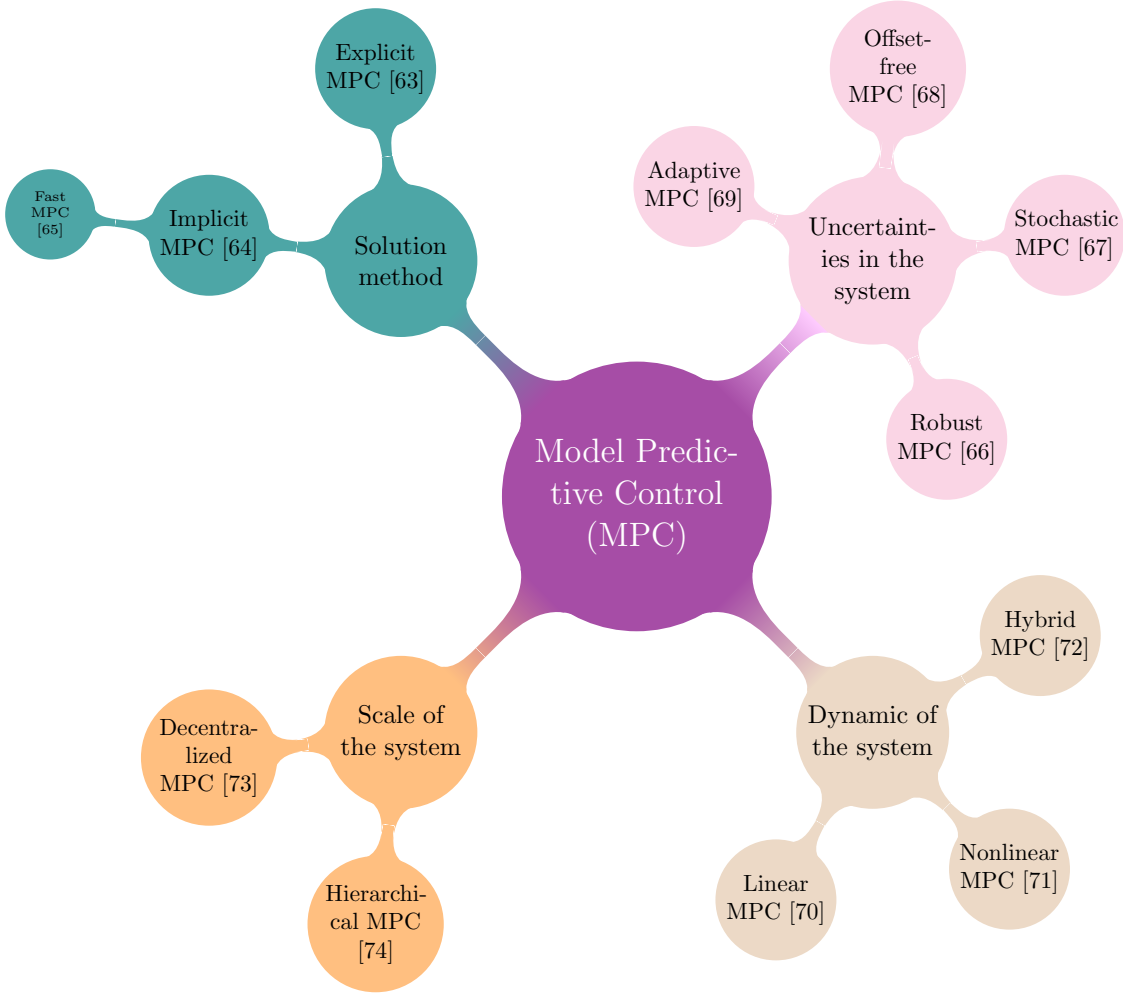
Figure 1.6: MPC categories and corresponding MPC methods.

1.4 Challenges and Research Gaps in State-of-the-art

In this section, the two research gaps in the state-of-the-art which this PhD dissertation aims to fill are detailed.

1. Integrated MPC for energy systems: Section 1.3 shows the suitability and advantages of MPC for energy systems. A comprehensive review of the literature shows that studies have been carried out in the area of MPC for building HVAC, ICE, and WHR systems individually; but there is a clear gap in studies on MPC which optimizes the combined building HVAC + MicroCSP system and the combined ICE + WHR systems. This thesis presents the first study to control an integrated building HVAC and MicroCSP systems by using MPC. Similarly, this thesis presents the first study for an integrated control of ICE and WHR, by using MPC. This allows for the optimal performance of the whole system, and achieves better performance compared to optimizing each component individually.

2. "Exergy"-wise control design: In order to optimize the energy usage in real-time, the designed MPC framework needs to define the energy flow and availability in an energy system. First Law of Thermodynamics (FLT) defines a state function which provides a statement of energy conservation [85]. Energy analysis can determine the

energy flows in a system. But, energy analysis does not quantify the irreversibilities in the system. The Second Law of Thermodynamics (SLT) defines entropy which is used to calculate exergy, or availability, as the portion of energy that can do useful work in a specific environment [85]. Exergy analysis can determine sources of entropy production and irreversibilities that cause the loss of work potential (i.e., exergy destruction) during a process [86, 87]. Compared to energy analysis, exergy analysis provides much more insight for control of a system to obtain the maximum efficiency in a specific environment [88]. In particular, exergy-based analysis and exergy-wise real time optimization is essential when dealing with systems with different energy conversions. Majority of the controllers in the literature are FLT based, while SLT based controllers can offer superior performance for systems with energy conversions. This thesis presents the first SLT-based controllers for HVAC + MicroCSP systems and ICE + WHR systems.

1.5 Contribution of this Dissertation

The PhD dissertation aims to address the research gaps identified in Section 1.4. In tune with that, the work in this PhD dissertation is divided in three stages. They are,

1. Model Development

† Control oriented models based on the FLT and SLT are developed and/or validated for both of the energy systems. The energy systems studied are (i) the combined MicroCSP and building HVAC system and (ii) the combined ICE and WHR system.

2. Design of MPC Framework

† MPC frameworks are designed for the two energy systems to provide real-time optimal solutions to the system actuators. The objectives of the designed MPCs are to:

- minimize the energy consumption of the system;

- minimize the energy cost of the system; and/or

- minimize the exergy destruction of the system.

3. Analysis of the Designed MPC Framework

† The results show that the designed MPC frameworks can:

- reduce the building HVAC energy consumption by 38% and 45% when optimal energy based MPC (EMPC) and exergy based MPC (XMPC) is applied to the combined MicroCSP and building HVAC system instead of a rule based controller (RBC);

- reduce the building HVAC energy cost by 70% when optimal energy cost based MPC (CMPC) is applied to the combined MicroCSP and building

HVAC system instead of the applied RBC; and

- – reduce the ICE fuel consumption by 6% and 7% when optimal EMPC and XMPC is applied to the combined ICE and WHR system; compared to when RBC is applied to ICE system without WHR.

1.6   Organisation of this Dissertation

The dissertation is organised as follows. Chapter 2 presents the modeling and optimal control of the combined MicroCSP and building HVAC system. In Chapter 2, the experimental testbed of the combined MicroCSP and building HVAC system is introduced. Then in Chapter 2, the mathematical models of the combined MicroCSP and building HVAC system are described. In addition, three different optimal control strategies are designed and applied to the combined MicroCSP and building HVAC system in Chapter 2. The three optimal controllers are (i) EMPC, (ii) CMPC, and (iii) XMPC. Finally in Chapter 2, the key results of the three designed MPC frameworks are analysed and compared.

Chapter 3 presents the modeling and optimal control of the combined ICE with WHR system. In Chapter 3, the experimental testbed of the combined ICE with WHR system system is introduced. Then in Chapter 3, the mathematical models of the combined ICE with WHR system are described. In Chapter 3, EMPC and

XMPC are designed and analysed for the combined ICE with WHR system. Finally, this dissertation is concluded, and possible future work is discussed in Chapter 4. The organization of this dissertation is summarized in Fig. 1.7.
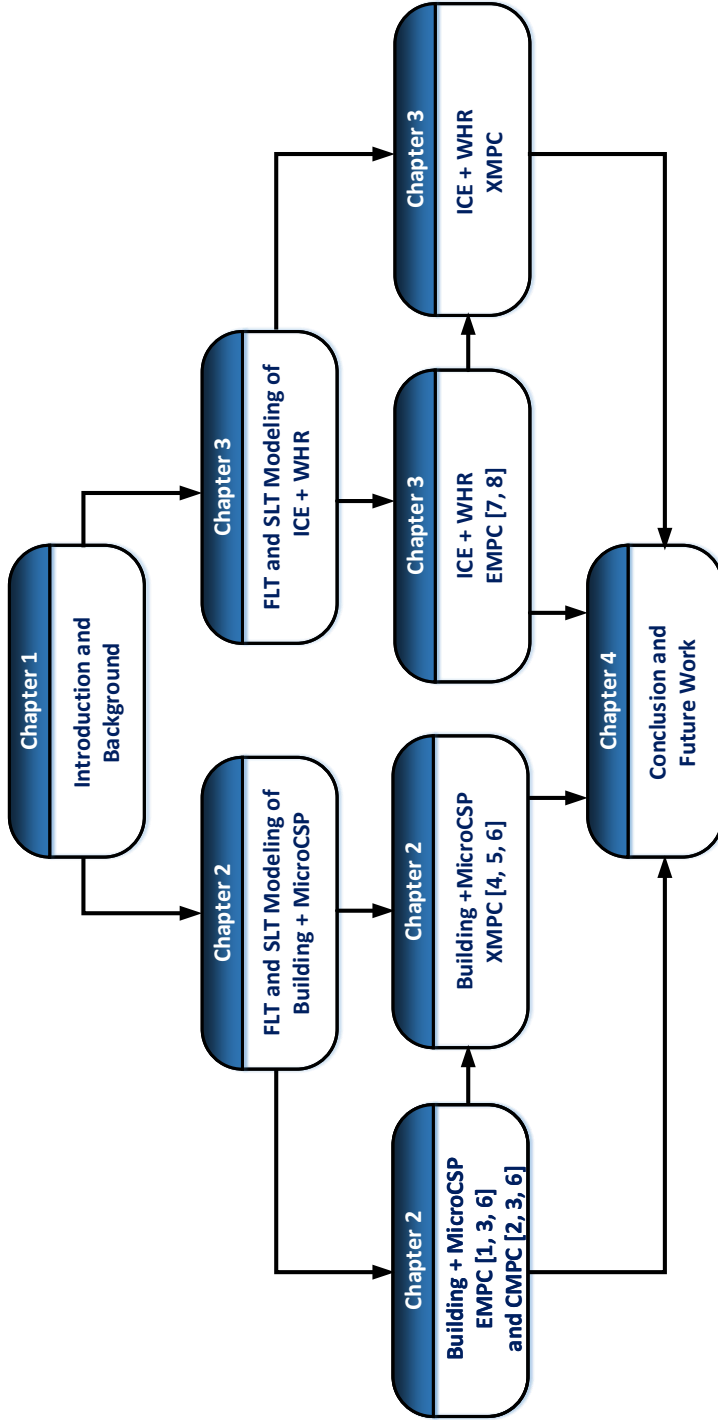
Figure 1.7: Organization of this dissertation. The numbers in the brackets show the publications from this work. EMPC, CMPC, and XMPC stand for energy based MPC, energy cost based MPC, and exergy based MPC, respectively.

Chapter 2

Model Predictive Control for Micro-scale Concentrated Solar Power and Building HVAC System[1]

2.1   Introduction

The United States Energy Information Agency (EIA) [89] reported that 38% of the total energy consumed, and 35% of the total CO_2 emissions in the US in 2017 were contributed by electricity consumption. In addition, 35% of the total electricity consumption was caused by commercial buildings; while, the heating, ventilation, and

---

[1]The results from this chapter are based Reddy et al. publications on (1) Energy Based MPC in [1, 3], (2) Energy Cost Based MPC in [2, 3], (3) Exergy Based MPC in [4, 5], and Optimal Integration and Control in [6].

air-conditioning (HVAC) systems were responsible for 42% of electricity consumption in commercial buildings in the US. This highlights the significance of the HVAC systems in commercial buildings and the need for developing methods to reduce HVAC energy consumption.

The integration of solar renewable energy into building HVAC system reduces the energy consumption from non-renewable sources like fossil fuels and thereby reduces CO_2 emissions caused by building HVAC systems. One common approach is to collect renewable solar energy and convert it to thermal energy using parabolic trough collectors (PTC). Next, the conversion of stored thermal energy to electrical energy is done using an organic Rankine cycle (ORC) in a concentrated solar power (CSP) system [90]. CSP systems that have a power output of less than 1 MW have recently gained popularity due to their energy saving potential [51] and are termed as microscale CSP (MicroCSP) systems. MicroCSP shows great promise for integration into building HVAC systems [2, 91]. But MicroCSP is driven by solar energy, which is limited to daylight hours and needs to be stored in order to be dispatched optimally in accordance with the building HVAC system energy demand.

This thesis investigates the control of the combined building HVAC and MicroCSP system. In the MicroCSP system in this thesis, the solar energy is converted to thermal energy by the PTC. The thermal energy from the PTC is then stored in a thermal energy storage (TES) and dispatched to the ORC when demanded by the

building HVAC system. The ORC co-generates electrical energy and thermal energy. The thermal energy from the ORC is used for heating purposes in the HVAC system in the building. In addition, electrical energy from the ORC reduces the electrical energy consumption from the grid in the HVAC system.

A controller is required to optimally operate the combined HVAC system in the building and the MicroCSP system. Authors in reference [76] show the suitability of model based design approach and model predictive controllers (MPC) to optimally control the HVAC systems in the building. Furthermore, authors in reference [92] show the advantages of MPC when applied to a domestic micro-grid system integrated with a photo-voltaic system for both management of power flow and thermal comfort. In another study in reference [93], authors discuss a robust MPC strategy to improve air control in an air-conditioning systems in the presence of model uncertainties while handling the constraints of the air handling units directly. MPC can provide real-time optimal solution based on the present value and the future predictions of ambient conditions, and solar irradiation while (i) handling constraints on TES, ORC, and heat pumps in this study, and (ii) maintaining the comfort temperature bounds in the thermal zones of the building. Hence in this thesis, control-oriented models of the building and MicroCSP are developed; then, an MPC framework is designed to optimally control the TES usage, ORC operation, along with the thermal energy flow from the heat pumps to the building. It is worth noting that, the building thermal model and HVAC model are based on a real test setup at Michigan Technological

University and the MicroCSP model is based on a recently purchased system [94, 95].

First law of thermodynamics (FLT) defines the energy conservation [85]. Energy analysis can determine the energy flows in a system. But, energy analysis does not quantify the irreversibilities. The second law of thermodynamics (SLT) defines exergy, or availability, as the portion of energy that can do useful work in a specific environment [85]. Exergy analysis can determine sources of entropy production and irreversibilities that cause the loss of work potential (i.e., exergy destruction) during a process [86, 87]. Compared to energy analysis, exergy analysis increases the computational complexity of the system [6]. Additionally, the growth in electrical energy consumption and time-varying power demand by consumers have motivated energy utility companies to set variable energy cost, called the locational marginal price (LMP), according to the daily temporal energy demand and supply [96]. Therefore, an optimal reduction in energy consumption might not translate to optimal reduction in energy cost due to varying LMP.

Hence in this thesis, the optimality of the designed MPC framework is based on either the energy, operational cost or the exergy of the combined MicroCSP and the building HVAC system. The organization of the remainder of the Chapter is as follows.

Detailed description of the building and the MicroCSP test-beds are given in Section 2.2. Energy and exergy models of the sub-systems are described in Section 2.3. The problem formulation, design, and control results of the optimal energy-based

MPC (EMPC) and energy cost-based MPC (CMPC) for the combined building HVAC and MicroCSP system are explained in Section 2.4. In addition, the problem formulation, design, and control results of the optimal exergy-based MPC (XMPC) for the combined building HVAC and MicroCSP system are discussed in Section 2.5. In particular, in Sections 2.4 and 2.5:

† the designed EMPC, CMPC, and XMPC are compared to a heuristically designed rule-based controller (RBC);

† a sizing study of the TES and/or the number of HVAC zones is carried out to determine the optimal integration of the MicroCSP and the building HVAC system;

† a probabilistic analysis using Monte Carlo simulations (MCS) is carried out to account for the prediction uncertainties and/or seasonal variations of the weather.

2.2 Testbed

The building considered in this study is the Lakeshore Center building at Michigan Technological University. This is an office building with three stories and it has an area of 5,700 m^2. Each room has its own heat pump (HP) for heating room air. Each

room is equipped with a temperature sensor with a ±0.2°C accuracy and is considered as an individual thermal zone in this study. The temperature data is measured at a sampling period of 1 minute. In this study, coefficient of performance (COP) of all the HPs for heating conditions is 3.2 and the heat exchangers in the ORC and HPs are assumed to be 100% efficient.
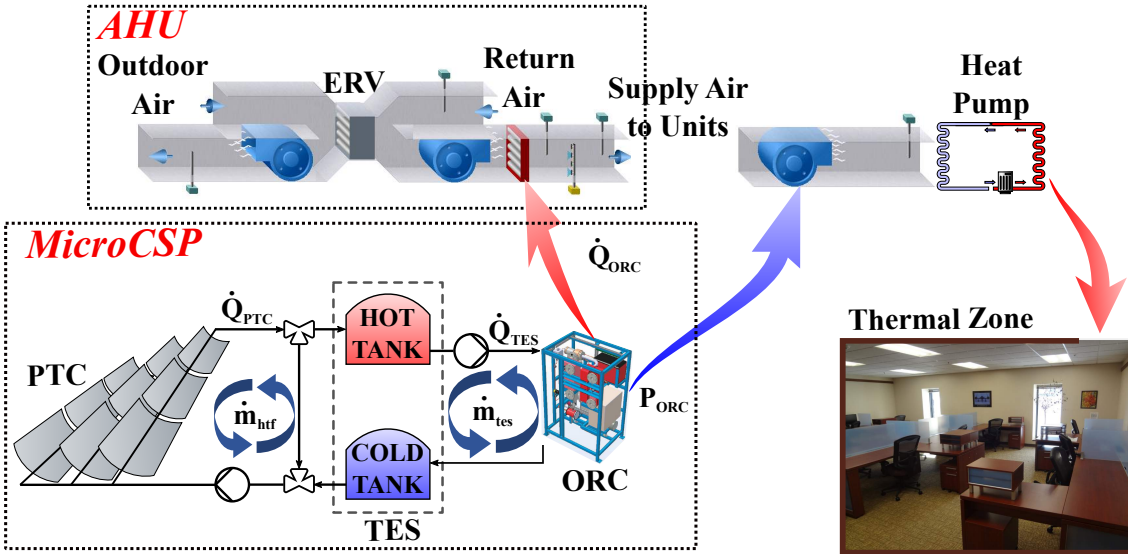
Figure 2.1: Schematic of the MicroCSP system and the HVAC system in the building considered in this study.

Table 2.1 provides the specifications of the MicroCSP sub-systems in this study. The MicroCSP system through collaboration with Mohammed V University of Rabat in Morocco. This thesis uses the experimental data from the manufacturers of the MicroCSP components to develop a physics-based experimentally validated MicroCSP model.

Structure of the test-bed in this work is depicted in Fig. 2.1. There are four sections

including MicroCSP, air handling unit (AHU), HP, and thermal zone. The building includes a total of 72 thermal zones. Fig. 2.1 shows that the AHU supplies air to the HPs in each HVAC zone in the building. During the unoccupied time in the room, the air from all the thermal zones is recirculated to AHU and this air is heated by the co-generated thermal power ($\dot{Q}_{ORC}$) of the ORC while the energy recovery ventilator (ERV) is turned off. During the occupied time in the room, the ERV is turned on. Fresh air comes from outside through the ERV and is mixed with air from all the thermal zones. This total air is heated by the $\dot{Q}_{ORC}$ of the ORC.

Table 2.1
MicroCSP sub-system specifications in this study.

Component	Parameter	Value	Manufacturer
PTC	Aperture area	54 m^2 each row	Soltigua
	Number of rows	3	PTMx24
TES	Heat transfer fluid	Therminol VP-1	Azolis Direct
	Working temperatures	140°C-180°C	Two-tank
	Storage capacity	48 kWh	
ORC	Working fluid	R245fa	ENOGIA
	Thermal power input	18 to 60 kW	ENO-10LT

2.3   Mathematical Models

This section introduces the mathematical models of PTC, TES, ORC, building thermal network and HVAC system, and AHU based on FLT analysis. Next, the models based on SLT analysis of ORC and building thermal network are discussed in this

section. In the MicroCSP system in the current study, ORC is the only energy conversion system whose exergy destruction is minimized. This is because exergy content of solar energy input, which is converted to thermal energy in PTC, and stored as thermal energy in TES, is fixed for given solar irradiation conditions that are not controlled. In addition, the exergy destruction of the building thermal network is minimized.

2.3.1 Parabolic Trough Collectors (PTC)

The MicroCSP setup includes a 3-row PTC with an aperture area of 54 m² per row. Each row of PTC has 4 collectors. The PTC receives solar energy and converts it to thermal energy. The thermal power ($\dot{Q}_{PTC}$) produced by the PTC is given by:

$$\dot{Q}_{PTC} = (\dot{Q}_{PTC,gain} - \dot{Q}_{PTC,loss}) \cdot NR \qquad (2.1)$$

where, $\dot{Q}_{PTC,gain}$ and $\dot{Q}_{PTC,loss}$ are the solar power absorbed and the heat loss in each row of the PTC, respectively; and NR is the number of rows which is equal to 3 for

this study. Next, $\dot{Q}_{PTC,gain}$ is calculated by:

$$\dot{Q}_{PTC,gain} = \eta_o \cdot IAM \cdot \cos(\theta) \cdot A_p \cdot DNI \tag{2.2}$$

where, η_o is the PTC's optical efficiency and is specified by the manufacturer [95] to be 0.7; IAM is the incident angle modifier which relates the losses due to the imperfections of the reflectors; θ is the angle between the line normal to the tracking plane and the solar beam; A_p is the aperture area; DNI is the direct normal irradiation. While, $\dot{Q}_{PTC,loss}$ is predicted by the following correlation [97]:

$$\dot{Q}_{PTC,loss} = k \cdot (T_{htf} - T_{amb}) \cdot \Delta L \tag{2.3}$$

where, k is the heat loss coefficient and is given by the PTC manufacturer [95] to be 0.64 W/[m°C]; T_{htf} is calculated as the arithmetic mean temperature of the HTF in the PTC; T_{amb} is the ambient temperature; ΔL is the length of each row of PTC given to be 27.2 m by the manufacturer [95].

Experimental data from the manufacturer Soltigua [98] was used to validate the
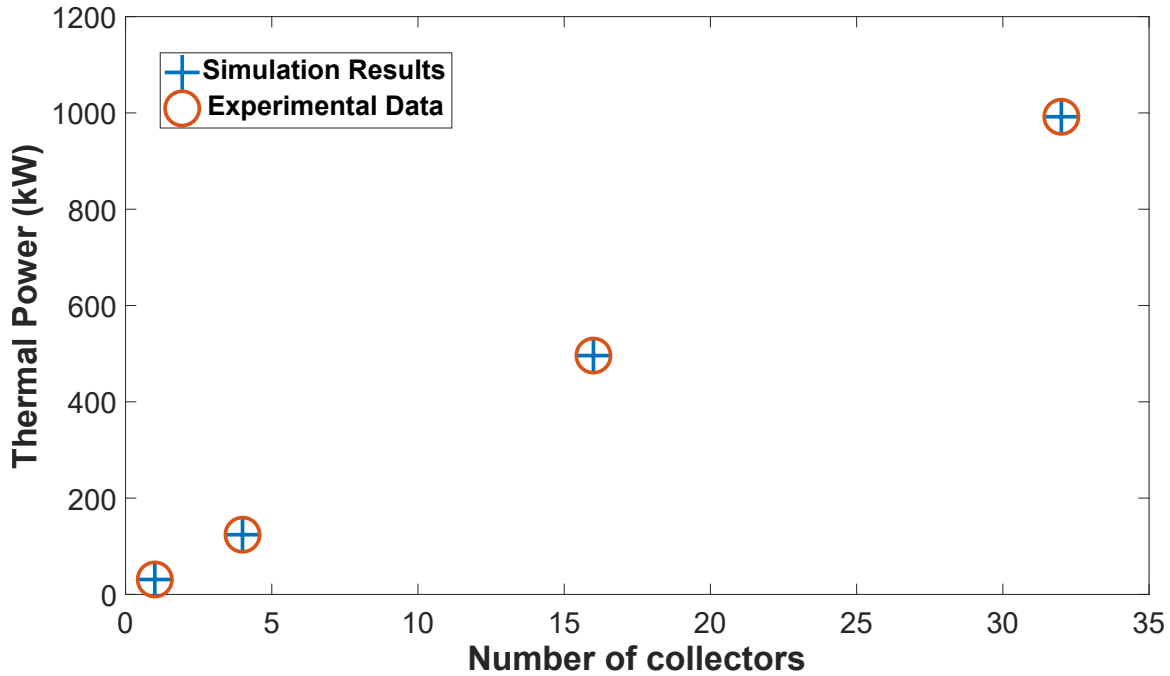
Figure 2.2: PTC model validation with manufacturer thermal power data [98] for different number of collectors.

PTMx-24 collector model in this work. In Fig. 2.2, the control-oriented model of the PTC was used to estimate the generated thermal power, at the nominal operating point, with respect to the number of collectors. The results show that the PTC model is in good agreement with the manufacturer data.

2.3.2 Thermal Energy Storage (TES)

The TES in this study is a two-tank direct system (Fig. 2.1) with operating temperature of 140^oC to 180^oC. During charging of the TES, low-temperature HTF from the cold tank passes through the PTC as it accumulates thermal energy from the PTC and goes to the hot tank. During discharging of the TES, the high-temperature HTF

from the hot tank passes through the ORC as it transfers thermal energy to the ORC and returns to the cold tank. The TES has its control system to maintain the HTF temperature between 140^oC and 180^oC before sending HTF from the hot tank to the ORC.

The TES state of charge (SOC) is determined by:

$$SOC[k] = SOC[k-1] + \frac{(\dot{Q}_{PTC}[k] - \dot{Q}_{TES}[k]) \cdot t_{sample}}{C_{TES}} \qquad (2.4)$$

where, [.] indicates the time index i.e., [k] represents the value at the current time step and [k-1] represents the value at the previous time step; $\dot{Q}_{PTC}$ is the thermal power produced by the PTC; $\dot{Q}_{TES}$ is the power from the TES to the ORC; C_{TES} is the capacity of the TES; t_{sample} is the sample time used for calculations.

2.3.3 Organic Rankine Cycle (ORC)

Fig. 2.3 shows the schematic of the ORC system in this study. By applying FLT to the ORC system in this study, the following system of equations is derived:

$$P_{gen} = \eta_{gen} \cdot \dot{m}_{WF} \cdot (h_1 - h_2) \tag{2.5a}$$

$$P_{motor} = \frac{\dot{m}_{WF} \cdot (h_4 - h_3)}{\eta_{motor}} \tag{2.5b}$$

$$P_{ORC} = P_{gross} - P_{motor} \tag{2.5c}$$

$$\dot{Q}_{ORC} = \dot{m}_{WF} \cdot (h_2 - h_3) \tag{2.5d}$$

$$\dot{Q}_{TES} = \dot{m}_{tes} \cdot c_{p,htf} \cdot (T_{ev,in} - T_{ev,out}) \tag{2.5e}$$

where, P_{gen} is the gross electrical power generated by the generator coupled to the turbine; P_{motor} is the electrical power consumed by the motor coupled to the pump; P_{ORC} is the net electrical power delivered by the ORC; $\dot{Q}_{ORC}$ is the thermal power generated by the ORC; $\dot{Q}_{TES}$ is the thermal power from the HTF to the ORC evaporator; h_x is the specific enthalpy of the ORC working fluid (WF) at state x; $\dot{m}_{WF}$ is the WF mass flow rate; η_{gen} and η_{motor} are the efficiencies of the ORC turbine generator and motor, respectively; $\dot{m}_{tes}$ is the HTF mass flow rate from the TES; $c_{p,htf}$ is the specific heat at constant pressure of the HTF; $T_{ev,in}$ and $T_{ev,out}$ are the HTF inlet and outlet temperatures to the ORC evaporator, respectively. Further, it
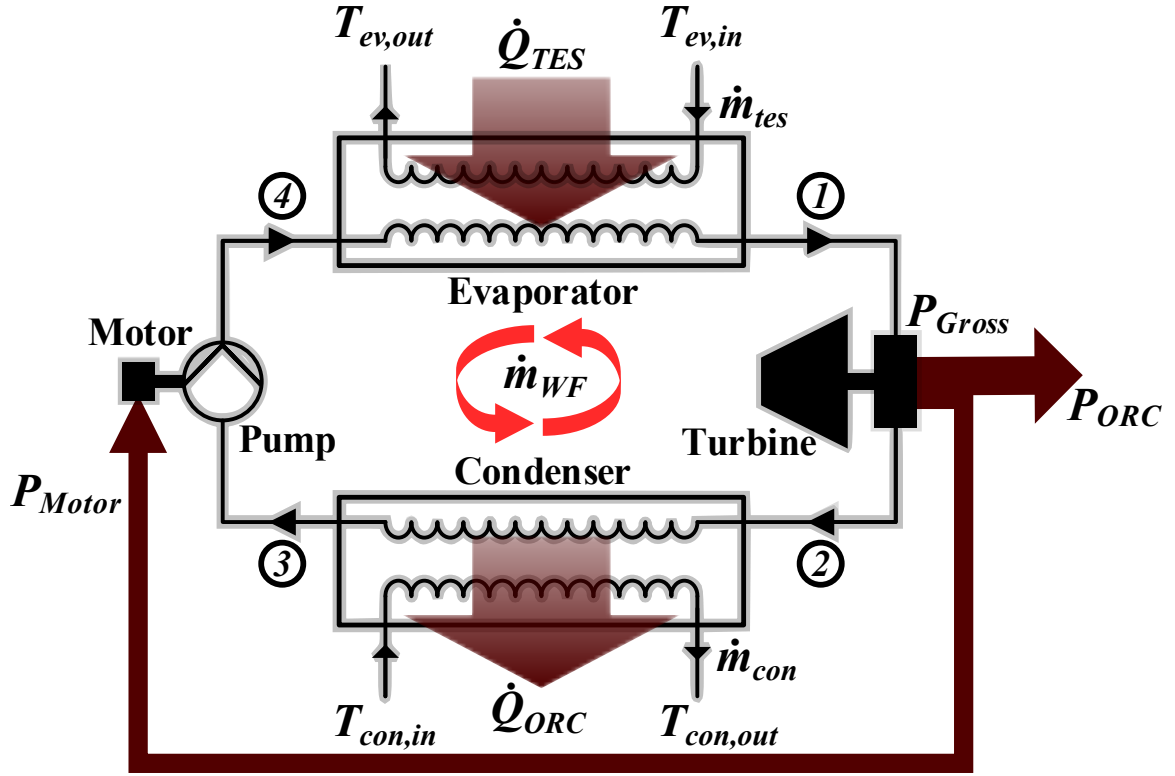
Figure 2.3: Organic Rankine Cycle (ORC) system in this study. The system has four states as shown by the circled numbers.

can be shown that:

$$P_{ORC} = f(\dot{m}_{tes}, r_p) \tag{2.6a}$$

$$\dot{Q}_{ORC} = g(\dot{m}_{tes}, r_p) \tag{2.6b}$$

where, $\dot{m}_{tes}$ is the mass flow rate of the HTF from the TES to the ORC, r_p is the pressure ratio.

The variation of P_{ORC} and $\dot{Q}_{ORC}$ with changes in $\dot{m}_{tes}$ and r_p are shown in Fig. 2.4.

(a) Thermal Power　　**(b) Electrical Power**
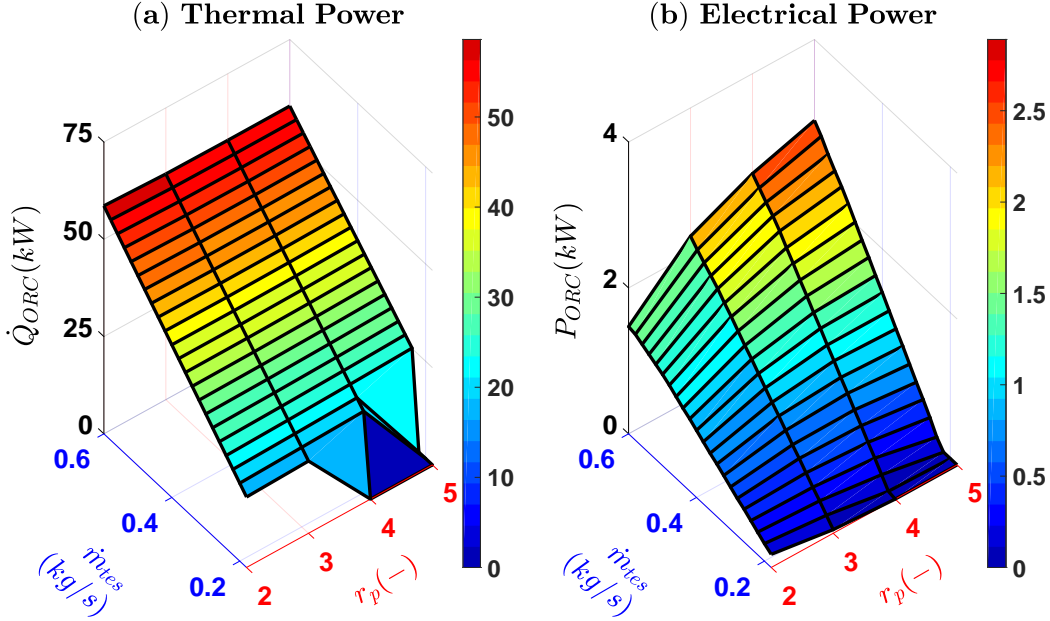
Figure 2.4: ORC co-generated heat rate ($\dot{Q}_{ORC}$) and electric power (P_{ORC}) as a function of pressure ratio (r_p) of the ORC and HTF mass flow rate ($\dot{m}_{tes}$) from the TES.

In Fig. 2.4, the x axis and y axis limits of $\dot{m}_{tes}$ and r_p are based on the physical limits given by the manufacturer [99]. Fig. 2.4(a) shows that the variation of $\dot{Q}_{ORC}$ with r_p is insignificant when compared to the variation in $\dot{Q}_{ORC}$ by changing $\dot{m}_{tes}$. Hence, $\dot{Q}_{ORC}$ can be further approximated as a function of only $\dot{m}_{tes}$.

$$\dot{Q}_{ORC} = g(\dot{m}_{tes}) \tag{2.7}$$

In addition, we can observe from Fig. 2.4(b) that P_{ORC} increases non-linearly with increase in both $\dot{m}_{tes}$ and r_p. Similar to Fig. 2.4(a), P_{ORC} is a strong function of $\dot{m}_{tes}$ in Fig. 2.4(b). The FLT based models of the ORC are validated against measurements

34

from manufacturer [99] for the nominal operation point of the ORC. The results are tabulated in Table 2.2. The errors between measurements and model outputs are found to be less than 3%.

By applying SLT to the ORC system in this study, the rate of exergy destruction of the ORC according to the state numbers in Fig. 2.3 is given by:

$$\dot{X}_{dest_{1-2}} = T_{amb} \cdot \dot{m}_{WF} \cdot (s_2 - s_1) \tag{2.8a}$$

$$\dot{X}_{dest_{2-3}} = T_{amb} \cdot \dot{m}_{WF} \cdot (s_3 - s_2 + \frac{q_{ORC}}{T_{con,m}}) \tag{2.8b}$$

$$\dot{X}_{dest_{3-4}} = T_{amb} \cdot \dot{m}_{WF} \cdot (s_4 - s_3) \tag{2.8c}$$

$$\dot{X}_{dest_{4-1}} = T_{amb} \cdot \dot{m}_{WF} \cdot (s_1 - s_4 - \frac{q_{TES}}{T_{ev,m}}) \tag{2.8d}$$

where, s_x is the specific entropy of the WF at state x (i.e., numbers 1 to 4 in Fig. 2.3); q_{TES} and q_{ORC} are the input and output heat per unit mass of the WF, respectively; $T_{ev,m}$ and $T_{con,m}$ are the arithmetic mean temperatures of the evaporator and condenser of the ORC, respectively.

The total rate of exergy destroyed by the ORC ($\dot{X}_{dest}^{ORC}$) is the sum of the rate of the exergy destroyed in the four processes (Fig. 2.3) and is calculated as:

$$\dot{X}_{dest}^{ORC} = T_{amb} \cdot (\frac{\dot{Q}_{ORC}}{T_{con,m}} - \frac{\dot{Q}_{TES}}{T_{ev,m}}) \tag{2.9}$$

For the ORC module in this study, we can show that the rate of exergy recovered $(\dot{X}_{rec}^{ORC})$ is mainly a function of electrical power from the ORC (P_{ORC}), thus

$$\dot{X}_{rec}^{ORC} = f(\dot{m}_{tes}, r_p) \qquad (2.10)$$

2.3.4   Building Thermal Network and HVAC System

The FLT based mathematical model for the office building in this study is based on previous works [100, 101, 102] from our research group and has been experimentally validated with the building temperature measurements. The model predicts room air temperature and calculates thermal load for each zone of the building. Details of the model are available in [100, 101, 102].

Table 2.2
ORC model validation against the manufacturer data [99] for the system nominal operating point. The inputs to the simulation model are $T_{ev,in}$, $T_{ev,out}$, P_1, T_1, P_3, T_3, and $\dot{m}_{tes}$ using the data provided by the manufacturer.

Variable	Unit	Measured	Simulated	Error (%)
$\dot{m}_{tes}$	kg/s	0.6	0.6	0.0
$\dot{Q}_{TES}$	kW	60	60.2	0.3
T_2	^oC	73.8	71.9	2.6
T_4	^oC	37	36.4	1.6
P_{gen}	kW	4	4	0.0
P_{motor}	kW	0.9	0.9	0.0
$\dot{Q}_{ORC}$	kW	55	56.1	2.0

The energy consumed by the building HVAC system is found using the following energy index ($I_{e,t}$):

$$I_{e,t} = \sum_{t=0}^{t} \sum_{i=1}^{N_{zones}} \left(P_{i,t}^F + P_{i,t}^H \right) \cdot \Delta t \tag{2.11}$$

where, i is the thermal zone number in the building, N_{zones} is the total number of thermal zones in the building, and t is time. The power consumption of the building HVAC system is the sum of the electrical power consumed by the HP in each thermal zone in the building ($P_{i,t}^H$) and the ventilation fan in each thermal zone in the building ($P_{i,t}^F$), which is calculated by:

$$P_{i,t}^F = \gamma_F \cdot (\dot{m}_{i,t}^r)^3 \tag{2.12a}$$

$$P_{i,t}^H = \frac{\dot{m}_{i,t}^r \cdot c_{p,air} \cdot (T_{i,t}^{Su} - T_{i,t}^{AHU})}{COP} \tag{2.12b}$$

where, $\dot{m}_i^r$ is the rate of mass flow of the supply air to the ith room and γ_F is power coefficient of the ventilation fan.

For the office building considered in this study, each thermal zone is considered as a control volume with constant air flow rate in and out of the control volume. In addition, the mass of air in the control volume (CV) is assumed to be constant. Furthermore, by applying SLT to the control volume, the rate of exergy destroyed for

the ith room of the office building ($\dot{X}^b_{dest_i}$) is given by:

$$\dot{X}^b_{dest_i} = (1 - \frac{T_{amb}}{T^r_i})\dot{Q}^{HT}_i - \dot{W}^r_i + (\sum_{in} \dot{m}^r_i \psi - \sum_{out} \dot{m}^r_i \psi) - \frac{dX^b_i}{dt} \qquad (2.13)$$

where, T_{amb} is the ambient air temperature; T^r_i is the air temperature of the ith room; $\dot{Q}^{HT}_i$ is the rate of heat transfer from the CV; $\dot{W}^r_i$ is the rate of work done by the flowing fluid in the CV; subscripts "in" and "out" refer to the inlet and outlet states in the flowing fluid of the CV, respectively; $\dot{m}^r_i$ is the air mass flow rate of flowing fluid in the CV; ψ is exergy related to the flowing CV; and X^b_i is the exergy of the CV.

But, the rate of exergy destroyed in the CV due to heat transfer in Equation (2.13) is given by:

$$(1 - \frac{T_{amb}}{T^r_i})\dot{Q}^{HT}_i = \sum_{j \in N^r_i}(1 - \frac{T_{amb}}{T^r_i})(\frac{T^r_j - T^r_i}{R^W_{i,j}}) \qquad (2.14)$$

where, T^r_j is the air temperature of the jth thermal node; and $R^W_{i,j}$ is the thermal resistance between i^{th} room and the jth thermal node.

In addition, the rate of work done by the flowing fluid in the CV in Equation (2.13) is 0.

$$\dot{W}^r_i = 0 \qquad (2.15)$$

Furthermore, the rate of exergy destroyed in the CV due to the flowing fluid in

Equation (2.13) is given by:

$$
\begin{aligned}
\left(\sum_{in} \dot{m}_i^r \psi - \sum_{out} \dot{m}_i^r \psi\right) = \ & \dot{m}_i^r \cdot [(h_{in} - h_{amb}) - T_{amb} \cdot (s_{in} - s_{amb}) \\
& + \frac{V_{in}^2}{2} + g \cdot z_{in} - (h_{out} - h_{amb}) \\
& + T_{amb} \cdot (s_{out} - s_{amb}) - \frac{V_{out}^2}{2} - g \cdot z_{out}]
\end{aligned}
\tag{2.16}
$$

where, h is the specific enthalpy of the flowing fluid in the CV; s is the specific entropy of the flowing fluid in the CV; subscript "amb" refers to the ambient condition; V is the velocity of the flowing fluid in the CV; g is the acceleration due to gravity; and z is the elevation of the flowing fluid in the CV.

Assuming the changes in kinetic energy and potential energy are negligible in the flowing fluid when compared to changes in the enthalpy and entropy of the flowing fluid in Equation (2.16), we get.

$$
\left(\sum_{in} \dot{m}_i^r \psi - \sum_{out} \dot{m}_i^r \psi\right) = \dot{m}_i^r \cdot [(h_{in} - h_{out}) - T_{amb} \cdot (s_{in} - s_{out})]
\tag{2.17}
$$

Next, the rate of exergy change in the CV in Equation (2.13) is given by:

$$\frac{dX_i^b}{dt} = \frac{d(m_i^{room} \cdot \Delta\phi)}{dt} = \frac{d(m_i^{room} \cdot (\phi_2 - \phi_1))}{dt}$$

$$= m_i^{room} \cdot \frac{d(\phi_2 - \phi_1)}{dt} + (\phi_2 - \phi_1) \cdot \frac{dm_i^{room}}{dt}$$

$$= m_i^{room} \cdot \frac{d(\phi_2 - \phi_1)}{dt} \; (Since, \; \frac{dm_i^{room}}{dt} = 0)$$

$$= m_i^{room} \cdot [(u_2 - u_{amb}) + P_{amb} \cdot (v_2 - v_{amb}) - T_{amb} \cdot (s_2 - s_{amb}) \qquad (2.18)$$

$$- (u_1 - u_{amb}) - P_{amb} \cdot (v_1 - v_{amb}) + T_{amb} \cdot (s_1 - s_{amb})]$$

$$= m_i^{room} \cdot [(u_2 - u_1) - T_{amb} \cdot (s_2 - s_{amb})]; \; Since, \; v_2 = v_1$$

$$\approx \frac{m_i^{room}}{\Delta t} \cdot [\Delta u - T_{amb} \cdot \Delta s]$$

where, m_i^{room} is the mass of the fluid in the room; ϕ is the exergy of the CV seen as a closed system; subscripts "1" and "2" refer to the fluid states at time t and $t + dt$; P is the pressure of the fluid in the CV; v is the specific volume of the CV and u is the specific internal energy of the flowing fluid in the CV.

Further, by assuming ideal gas approximations for the flowing fluid in the CV, we get [103]:

$$\Delta u = \int_a^b c_{v,air} \cdot dT \Rightarrow u_b - u_a = c_{v,air} \cdot (T_b - T_a) \qquad (2.19)$$

$$\Delta h = \int_a^b c_{p,air} \cdot dT \Rightarrow h_b - h_a = c_{p,air} \cdot (T_b - T_a) \qquad (2.20)$$

40

$$\text{Since } v_b = v_a, \text{ then}$$

$$\Delta s = \int_a^b \frac{c_{v,air}}{T} \cdot dT + R \cdot \ln \frac{v_b}{v_a} \Rightarrow s_b - s_a = c_{v,air} \cdot \ln \frac{T_b}{T_a} + R \cdot \ln \frac{v_b}{v_a} \qquad (2.21)$$

$$= c_{v,air} \cdot \ln \frac{T_b}{T_a}$$

where, subscripts "a" and "b" are the ideal gas states; T is the temperature of the ideal gas; $c_{v,air}$ is the specific heat at constant volume of the ideal gas; $c_{p,air}$ is the specific heat at constant pressure of the ideal gas; and R is the gas constant of the ideal gas.

Finally, Equation (2.22) is obtained by:

† substituting the Equations (2.19), (2.20) and (2.21) in Equations (2.17) and (2.18);

† substituting Equations (2.14) and (2.15) along with the resulting Equations (2.17) and (2.18) in Equation (2.13); and

† discretizing Equation (2.13) with $\Delta t = t_{sample}$.

$$\dot{X}^b_{dest_i}[k] = \sum_{j \in N^r_i} (1 - \frac{T_{amb}[k]}{T^r_i[k]})(\frac{T^r_j[k] - T^r_i[k]}{R^w_{i,j}})$$

$$+ \dot{m}^r_i[k] \cdot [c_{p,air} \cdot (T^{Su}_i[k] - T^r_i[k]) - T_{amb}[k] \cdot c_{v,air} \cdot \ln(\frac{T^{Su}_i[k]}{T^r_i[k]})] \qquad (2.22)$$

$$- \frac{m^{room}_i \cdot c_{v,air}}{t_{sample}} \cdot [(T^r_i[k] - T^r_i[k-1]) - T_{amb}[k] \cdot \ln \frac{T^r_i[k]}{T^r_i[k-1]}]$$

Where, [.] indicates the time index i.e., [k] represents the value at the current time step and [k-1] represents the value at the previous time step; T_i^{Su} is the supply air temperature to the ith room of the office building.

2.3.5 Air Handling Unit (AHU)

The AHU inputs pre-heated air from the ERV to the HP in each HVAC zone in the building. The inlet air temperature to the HP is calculated for both occupied and unoccupied times as shown below:

$$
T_{i,t}^{AHU} =
\begin{cases}
\text{a) Occupied time,} \\[2ex]
\dfrac{\dot{m}_{i,t}^r - \dot{m}_{i,t}^v}{\dot{m}_{i,t}^r} T_{i,t}^r + \dfrac{\dot{m}_{i,t}^v}{\dot{m}_{i,t}^r} T_t^{ERV} + \dfrac{\dot{Q}_{ORC,t}}{N_{zones}\dot{m}_{i,t}^r c_{p,air}} \\[3ex]
\text{b) Unoccupied time,} \\[2ex]
T_{i,t}^r + \dfrac{\dot{Q}_{ORC,t}}{N_{zones}\dot{m}_{i,t}^r c_{p,air}}
\end{cases}
\tag{2.23}
$$

During the unoccupied time in the room, the returning air from all the thermal zones in the building is recirculated through the ORC condenser and then goes to the HPs. During the occupied time in the room, the ventilation requirement based on the required indoor air quality is considered. In this study, the default occupant density of the office space is taken to be 5 persons/100 m^2 and the default combined outdoor

air rate (i.e., required fresh air) is 8.5 L/(s.person), using the ASHRAE standard 62.1-2007 [104]. Furthermore, the returning air from all the thermal zones is recirculated and mixed with the required flow rate $(\dot{m}_i^v)$ of fresh air from the ERV. Then, the resulting air goes through the ORC condenser and is heated to supply the HPs or the HVAC zones in the building directly. The ERV outlet air temperature (T_t^{ERV}) is determined by:

$$T_t^{ERV} = T_{amb,t} + ERE \cdot (T_{i,t}^r - T_{amb,t})$$ (2.24)

where, ERE is the Energy Recovery Effectiveness that is calculated according to AHRI/ASHRAE standard 1060 [105].

2.4 Energy Based Model Predictive Control (EMPC) and Cost Based Model Predictive Control (CMPC) - Framework Design, Results and Analysis

2.4.1 Structure of the Designed Energy Based Model Predictive Control (EMPC)

Fig. 2.5 shows the structure of the MPC framework designed to minimize the electrical energy consumption of the building HVAC system equipped with the MicroCSP. At each time step Δt, the optimization problem is solved over the prediction horizon N. Equation (2.25) defines the objective function while Equation (2.26) lists the constraints. The optimized variables are the supply air temperature (T^{Su}), the HTF mass flow rate from the TES ($\dot{m}_{tes}$), and the slack variables ($\bar{\epsilon}, \underline{\epsilon}$) used to guarantee the existence of a feasible solution. The inputs to the MPC optimizer are solar irradiation and weather forecasts. The comfort temperature bounds are set based on

ANSI/ASHRAE Standard 55-2013.

$$\min_{\dot{m}_{tes},T^{Su},\bar{\epsilon},\underline{\epsilon}}\{(I_{e,t} - \overbrace{\sum_{t=0}^{t_f} P_{ORC,t}.\Delta t}^{P_{Grid,t}.\Delta t}) + \rho(|\bar{\epsilon}|_1 + |\underline{\epsilon}|_1)\} \tag{2.25}$$

Subject to the following constraints:

$$T_{t+k+1|t} = AT_{t+k|t} + BT^{Su}_{t+k|t} + Ed_{t+k|t} \tag{2.26a}$$

$$T^z_{t+k|t} = CT_{t+k|t} \tag{2.26b}$$

$$P_{ORC,t+k|t} = f(\dot{m}_{tes_{t+k|t}}, r_{p_{t+k|t}}) \tag{2.26c}$$

$$\dot{Q}_{COG,t+k|t} = g(\dot{m}_{tes_{t+k|t}}) \tag{2.26d}$$

$$SOC_{t+k+1|t} = SOC_{t+k|t} + \frac{(\dot{Q}_{SOL_{t+k|t}} - \dot{Q}_{TES_{t+k|t}}).\Delta t}{C_{TES}} \tag{2.26e}$$

$$\underline{SOC} \leq SOC_{t+k+1|t} \leq \overline{SOC} \tag{2.26f}$$

$$0 \leq \dot{m}_{tes_{t+k|t}} \leq \dot{m}_{max} \tag{2.26g}$$

$$T^{AHU}_{t+k|t} \leq T^{Su}_{t+k|t} \leq \bar{\mathcal{T}}_{t+k|t} \tag{2.26h}$$

$$\underline{T}^r_{t+k|t} - \underline{\epsilon}_{t+k|t} \leq T^r_{t+k|t} \leq \bar{T}^r_{t+k|t} + \bar{\epsilon}_{t+k|t} \tag{2.26i}$$

$$\underline{\epsilon}_{t+k|t}, \bar{\epsilon}_{t+k|t} \geq 0 \tag{2.26j}$$

The state-space Equations (2.26a) and (2.26b) capture the thermodynamics of the building; Equations (2.26c) and (2.26d) include the ORC model; the SOC of the TES

is estimated in Equation (2.26e); Equation (2.26f) defines the upper and lower bounds of the TES SOC set to 95% and 5%, respectively; Equation (2.26g) is the maximum HTF mass flow rate ($\dot{m}_{max}$) dictated by the ORC manufacturer [94]; Equation (2.26h) shows the constraints on the supply air temperature that represents the constraint on the control input; Equation (2.26i) defines the comfort temperature bounds of the thermal zone temperature and includes the slack variables; finally, Equation (2.26j) presents the slack variables constraints.
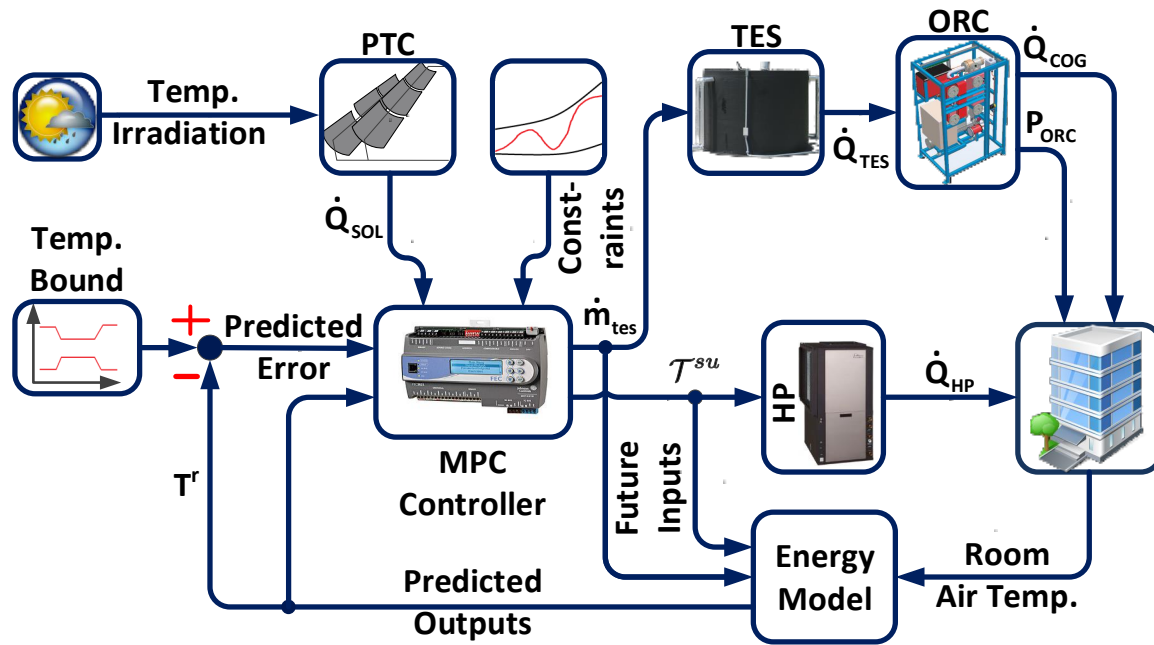
Figure 2.5: Structure of the designed EMPC to minimize the electrical energy consumption of the combined MicroCSP system and HVAC system in the building.

2.4.2 Structure of the Designed Energy Cost Based Model Predictive Control (CMPC)

The objective function in Equation (2.27) is used for energy cost minimization of the building HVAC system with MicroCSP. The building power consumption in the objective function is multiplied by locational marginal pricing (LMP) of electricity. The LMP data is provided by the Midcontinent Independent System Operator (MISO) at most 24 hours in advance [106]. The optimization problem is solved for the following objective function subject to the same constraints listed in Equation (2.26).

$$\min_{\dot{m}_{tes}, \mathcal{T}^{su}, \bar{\epsilon}, \underline{\epsilon}} \left\{ \left(I_{e,t} - \overbrace{\sum_{t=0}^{t_f} P_{ORC,t}.\Delta t}^{P_{Grid,t}.\Delta t} \right) .\Omega^T + \rho(|\bar{\epsilon}|_1 + |\underline{\epsilon}|_1) \right\} \tag{2.27}$$

Where, Ω^T is the LMP.

2.4.3 Control Results

MATLAB® software was used to implement the building, PTC, TES, and ORC models. YALMIP Toolbox [107] was used in MATLAB® for the optimization problem formulation and providing an interface with the solver. IPOPT [108] and Gurobi [109] were used as solvers, and the optimization problem was run in a computer with Intel®

47
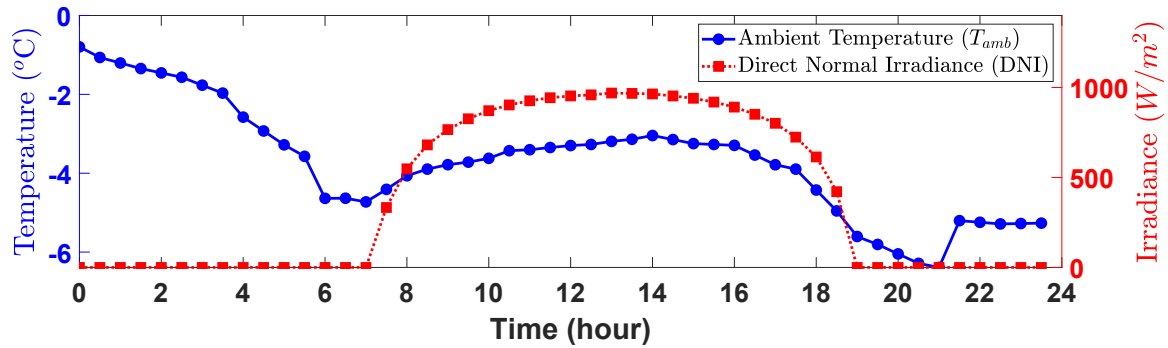
Figure 2.6: Ambient air temperature (T_{amb}) and Direct Normal Irradiance (DNI) measurements from March 18, 2016, in Houghton, MI.

Core™ i7-7500 CPU @ 2.90GHz and 16.0 GB RAM.

The prediction horizon is $N = 48$, and the time step is $\Delta t = 30$ minutes. It is worth mentioning that the one-day ahead prediction constraint is dictated by the availability of the forecast data which is only available for the next 24 hours. 72 thermal zones are considered for the building simulation. The simulations are performed using weather data from March 18, 2016, in Houghton, MI, USA, as shown in Fig. 2.6.

2.4.3.1 Rule Based Control (RBC)

The most commonly used controllers for building HVAC systems are the rule-based controllers (RBC) due to their simplicity and easy implementation. To guarantee thermal comfort, the RBC checks the thermal zone temperature at each time step. When the thermal zone temperature is outside the comfort temperature bounds, the RBC switches on the heating or cooling elements for the time step period Δt until it

48

is again within the comfort temperature bounds. Here, the RBC results are explained since they provide a baseline to compare with MPC results for the MicroCSP system to assess the impact of the predictive model-based control strategy on saving HVAC energy or cost.

Fig. 2.7 depicts the RBC results for MicroCSP integration into the building. As it can be seen in Fig. 2.7(a), when the thermal zone temperature violates the comfort temperature bounds at 7 AM and 9 PM, the RBC turns on the HP to increase the thermal zone temperature and brings it within the comfort temperature bounds. Starting from 8 AM, the MicroCSP uses the maximum amount of thermal energy cumulated in the TES from the PTC solar array (Fig. 2.7(b)). From Fig. 2.7(c), it can be seen that the HP operates only when the comfort temperature bounds are violated while the ORC heat production supplies heat to the thermal zone as long as it is available, keeping its temperature within the comfort temperature bounds. Fig. 2.7(d) depicts the power supplied to the HP by the grid and the LMP. Since the solar energy production is directly injected into the ORC without any dispatch, the SOC does not vary much, as it is shown in Fig. 2.7(e).

2.4.3.2 Energy Based Model Predictive Control (EMPC)

Fig. 2.8(a) shows the temperature profiles of the supply air and a sample thermal zone within the comfort temperature bounds. From midnight to 6 AM, when the
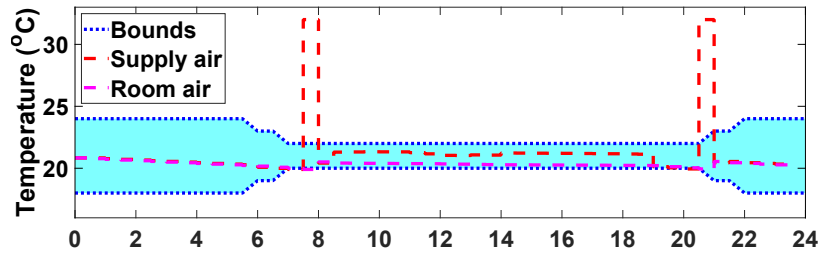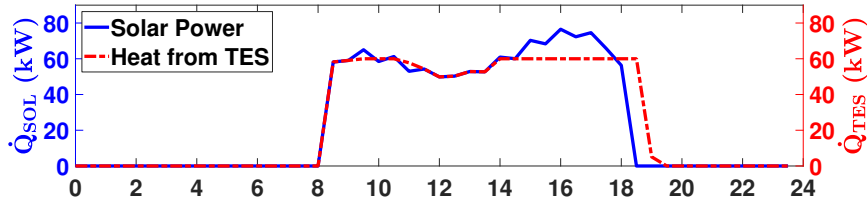
49

(a) Supply air and resulting thermal zone temperatures

(b) PTC solar array generation and TES dispatched heat
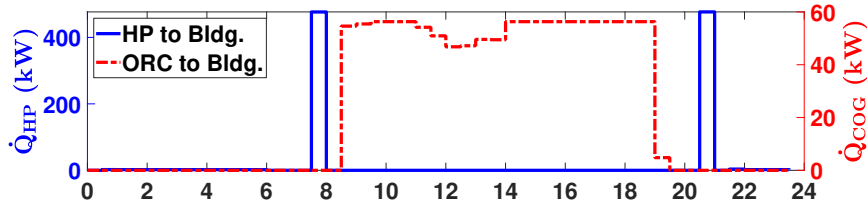
(c) HP and cogeneration heat supplied to the building
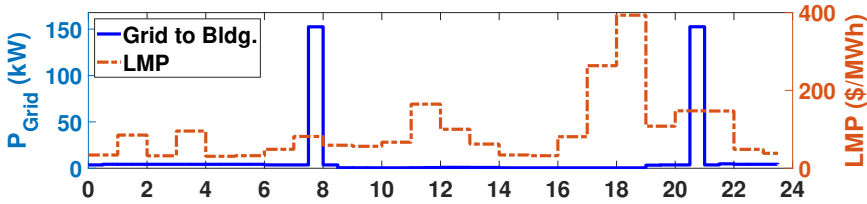
(d) Power supplied by the power grid to the building and LMP
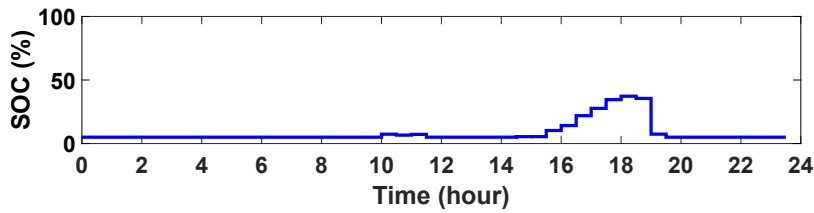
(e) State of charge of the TES

Figure 2.7: __RBC results__ of the combined MicroCSP system and the building HVAC system.

building is not occupied, the thermal zone temperature is allowed to fall down without violating the comfort bounds. Then, during the building occupancy, the HP supplies the minimum amount of heat to ensure that the thermal zone temperature stays at the lower comfort bound. Fig. 2.8(b) shows the heat produced in the PTC solar array, and the heat dispatched from the TES to the ORC. At the beginning and the end of the building occupancy, there is not enough heat production from the PTC solar array, hence the MPC uses the HP to supply the required heat to the thermal zone. When the TES is filled with enough quantity of heated HTF from the PTC solar array, the MPC runs the ORC to provide cogeneration heat to the building (Fig. 2.8(c)). Fig. 2.8(d) shows the power supplied from the power grid and from the ORC to the building. The MPC controls the PTC solar array production through the TES, regulating the input heat of the ORC to operate at its maximum efficiency and provide cogeneration heat to keep the thermal zone at the lower comfort bound. This causes the SOC of the TES to vary, as shown in Fig. 2.8(e).

2.4.3.3 Energy Cost Based Model Predictive Control (CMPC)

The MPC results for minimizing HVAC operational cost are shown in Fig. 2.9. Fig. 2.9(a) shows the temperature profiles of the supply air and a sample thermal zone within the comfort temperature bounds. It can be seen that from midnight to 4 AM when the building is not occupied, the HP are turned off as the thermal zone
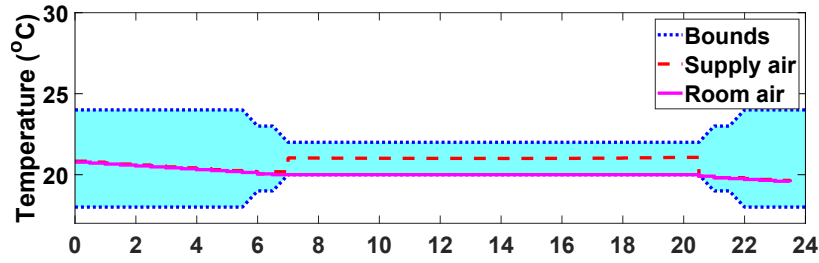
(a) Supply air and resulting thermal zone temperatures
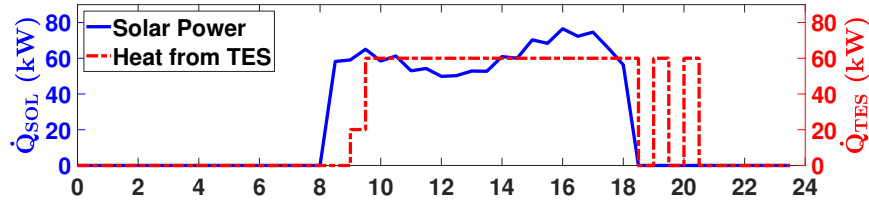
(b) PTC solar array generation and TES dispatched heat
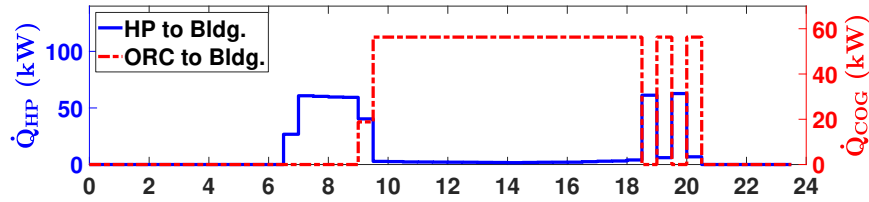
(c) HP and cogeneration heat supplied to the building
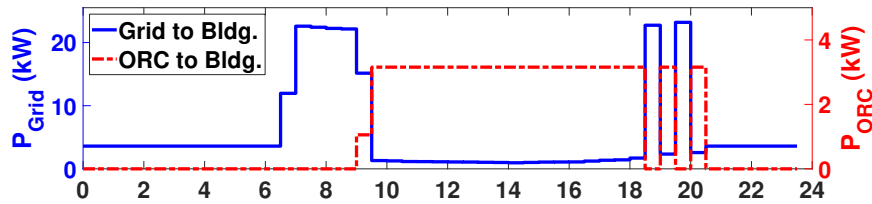
(d) Power grid and ORC power supplied to the building
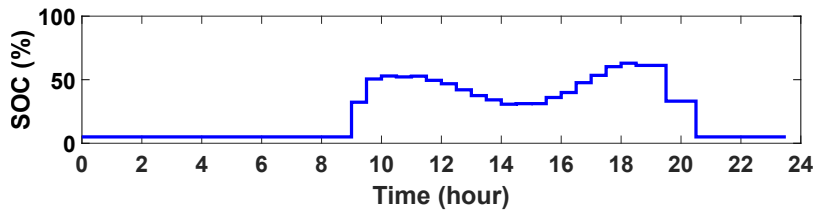
(e) State of charge of the TES

Figure 2.8: __EMPC results__ of the combined MicroCSP and the building HVAC system.

temperature is within the comfort temperature bounds. Then, at 4:30 AM when the LMP is low, the MPC is preheating the room to guarantee that the thermal zone temperature does not fall below the lower comfort bound. During the building occupancy, the MPC tries to maintain the thermal zone temperature close to the lower comfort bound to avoid spending unnecessary energy. Fig. 2.9(b) shows the thermal power generated by the PTC solar array and the TES thermal power supplied to the ORC. As shown in Fig. 2.9(c), the MPC turns on the HP around 4:30 PM to preheat the thermal zone when the LMP is low. Then, when the PTC solar array starts producing enough heat, the HP supplies heat to the thermal zone using cogeneration heat from the ORC and switch to the HP only when the LMP is low again (3 PM). Fig. 2.9(d) depicts the grid power consumed by the HP as a response to the LMP variations. The TES stores the extra heat generated by the PTC solar array that is not used by the ORC so that it can be utilized later, at the end of the day when the solar irradiation is not enough to produce heat in the PTC solar array. The variation of the SOC of the TES is shown in Fig. 2.9(e) and confirms that all the solar energy is used; thus, the initial and final SOCs are the same.

The building occupancy coincides with the sunlight period; hence, the thermal zones are heated using cogeneration heat from the MicroCSP keeping their temperature inside the comfort bounds. However, when the MicroCSP is off, the thermal zone temperature falls down until it violates the comfort temperature bounds only then the RBC turns on the HP to bring back the thermal zone temperature inside the
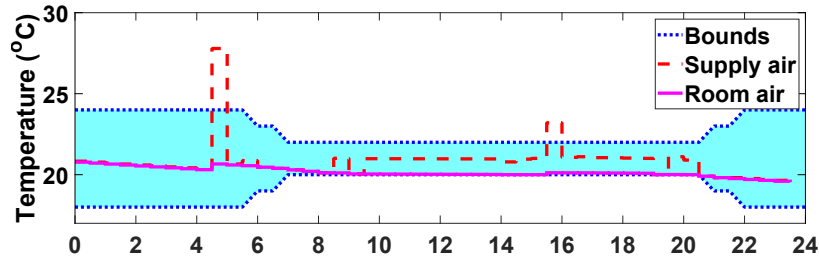
(a) Supply air and resulting thermal zone temperatures
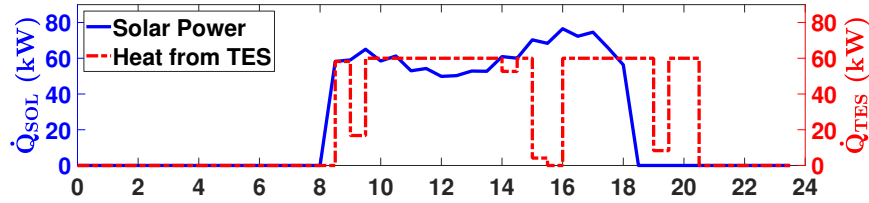
(b) PTC solar array generation and TES dispatched heat
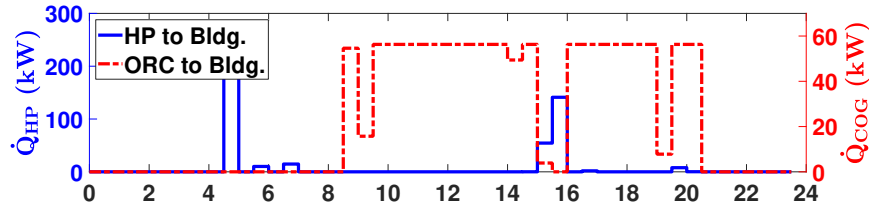
(c) HP and cogeneration heat supplied to the building
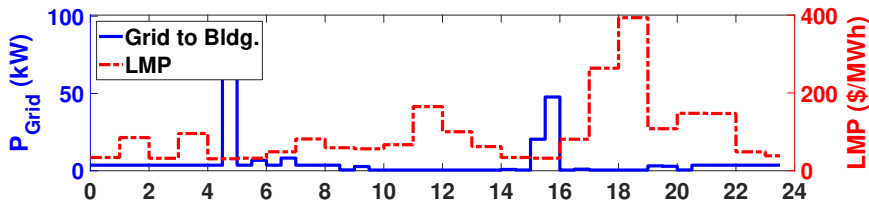
(d) Power supplied by the power grid to the building and LMP
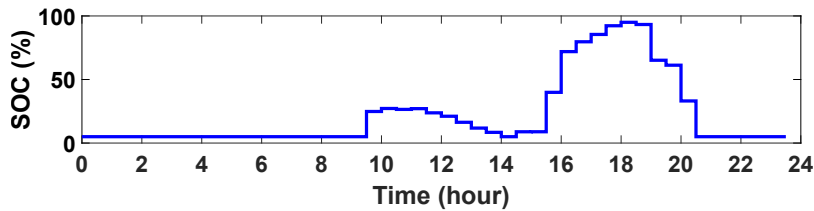
(e) State of charge of the TES

Figure 2.9: <u>**CMPC results**</u> of the combined MicroCSP and the building HVAC system.

comfort temperature bounds which leads to high energy consumption. Since this violation occurs in periods when LMP is high (Fig. 2.7) it leads to higher costs as well. The predictive capability of the MPC anticipates these temperature violations and turns on the HP to preheat the thermal zone when the MicroCSP is off (Fig. 2.8) or when the LMP is low (Fig. 2.9).

Table 2.3 presents the energy consumption and energy cost saving by utilizing the designed EMPC and CMPC for the combined building HVAC and the MicroCSP system compared to utilizing the RBC.

Table 2.3 shows that the designed EMPC and CMPC framework for the control of the MicroCSP integrated into the building HVAC system, the energy and cost savings are 38% and 70%, respectively. This shows the importance of the MPC framework to exploit the full potential of the MicroCSP thermal and electrical production when integrated into the building HVAC system.

Table 2.3
Electrical energy consumption and cost comparison for showing the
significance of using MPC control.

Control Type	Energy Consumption [kWh/day]	Energy Saving* [%]	Control Type	Electricity Cost [$/day]	Cost Saving* [%]
RBC	208.7	-	RBC	21.5	-
EMPC	130.3	37.6%	CMPC	6.4	70.2%

*Calculated by reference to RBC of the HVAC system with MicroCSP integration.

2.4.3.4 Storage Capacity Effects

This section investigates into the effect of the size of TES on the results of MicroCSP integration into the building HVAC system in terms of energy consumption and cost.

Fig. 2.10 shows that TES size has more effect on the cost saving than the energy saving. The energy saving reaches its maximum value with a 38 kWh capacity TES and using a bigger TES does not lead to more energy saving. Indeed, for the actual penetration rate and without price incentives, the MicroCSP energy production does not need to be substantially dispatched as it can be consumed almost instantly by the building during the occupancy period. Still, minimum storage is required to guarantee that the ORC of the MicroCSP system is supplied with the nominal thermal power to operate at its maximum efficiency. On the other hand, increasing the TES capacity lowers the energy cost since it improves the system flexibility in terms of dispachability, so that MicroCSP production can supply the building at periods of high LMP as it is shown in Fig. 2.9. The energy cost saving reaches its maximum value starting from 114 kWh capacity.
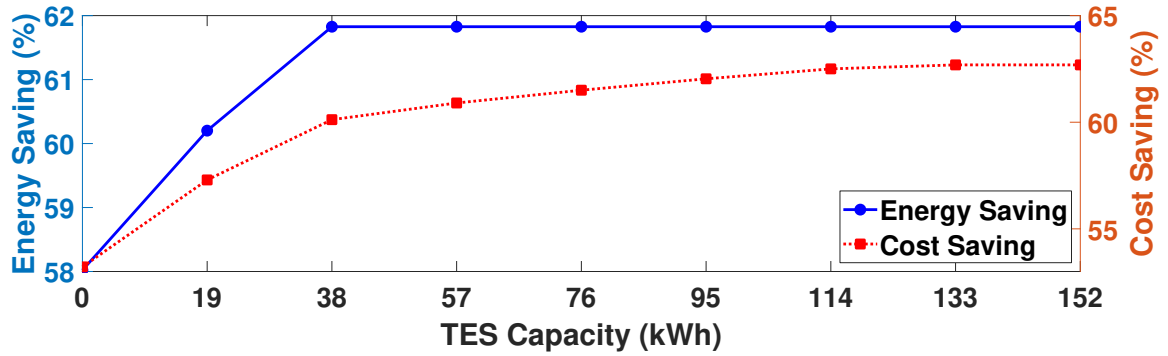
Figure 2.10: Effects of storage capacity for the building HVAC daily energy consumption and daily electricity cost.

2.4.3.5 Monte Carlo Simulations

The MPC results can be subject to interpretation since they do not consider prediction uncertainty in LMP, solar irradiation, and variations in weather conditions. Hence, to demonstrate the performance of the designed MPC framework in the presence of variations and prediction uncertainties, a probabilistic Monte-Carlo analysis is carried out.

Reference [110] defines the accuracy of the temperature prediction as the percentage of forecasts within three degrees of Fahrenheit. According to reference [110] the accuracy of the temperature prediction is around 70% for the location of the testbed. Several parameters affect the forecast of solar irradiation which can be categorized into deterministic parameters (i.e., geographic coordinate, season, time of the day, etc.) and probabilistic parameters (i.e., weather, cloudiness, etc.). Authors in [111] have reported several techniques to forecast LMP with a mean absolute percent error

(MAPE) ranging from 0.9% to 1.5%. Reference [112] presents a technique for forecasting solar irradiation with a MAPE of 9.1% for sunny days and 26.7% for cloudy days.

In this thesis, the Monte-Carlo analysis is performed by introducing additive uncertainty with a normal distribution to simulate random variations of the weather conditions, the solar irradiation, and the LMP using the results from [110, 111, 112]. The Monte-Carlo simulation results, depicted in Fig. 2.11, show the validity of the proposed methods with the presence of variations and prediction uncertainties.

Fig. 2.11 (a) and Fig. 2.11 (b) depict the probability distribution of the energy and cost savings of the building HVAC integrating MicroCSP by applying MPC, compared to using RBC. It can be seen that the probability of achieving at least 37% energy saving is around 60%, while the probability of at least 70% cost saving is 50%. Furthermore, it is shown that the energy saving will always be above 33% and the cost saving will always be above 68% in the worst case. This shows the significance of using MPC versus RBC for optimal operation of integrated HVAC and MicroCSP system.

2.4.4 Summary and Conclusion

Section 2.4 presented a real-time model predictive control framework to minimize the energy consumption and operational cost of the building HVAC system with
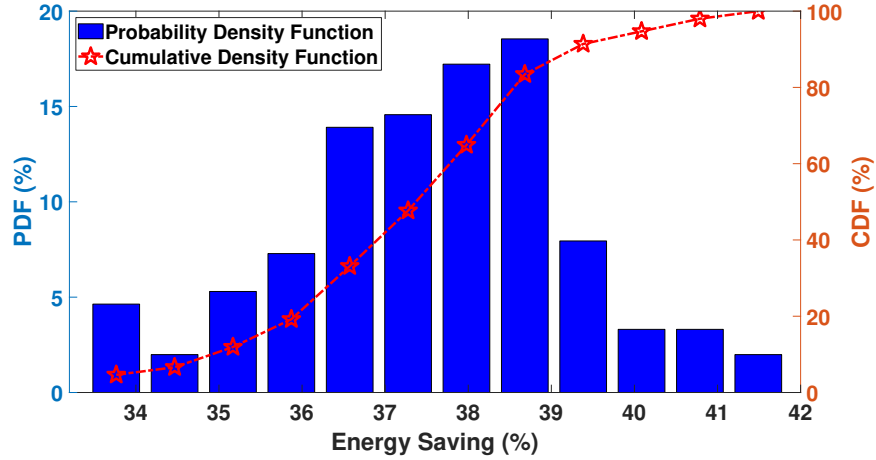
(a) Energy saving probability
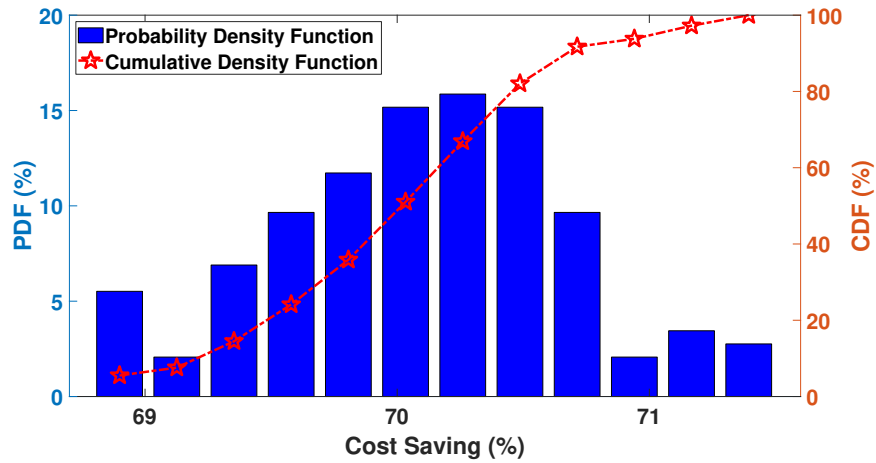
(a) Cost saving probability

Figure 2.11: __Monte-Carlo MPC simulation results__ showing the probability of the building HVAC energy and energy cost savings by applying EMPC and CMPC, respectively; __compared to using RBC.__

integrated MicroCSP. In addition, a new control-oriented mathematical model of a MicroCSP system is derived. All MicroCSP and HVAC submodels were experimentally validated [23, 98, 99, 100, 101, 102]. The key findings of this work are listed below:

Controller design effect: MPC vs. RBC

† The control results show that the design of an EMPC framework for the MicroCSP integrated into the building HVAC system leads to a 37% energy saving compared to the conventional RBC. In other words, by understanding MicroCSP and HVAC dynamics, one can significantly reduce the energy consumption of the HVAC system. Furthermore, the designed CMPC framework provides 70% reduction of the energy cost compared to the RBC. This shows that the MPC framework has more benefits when dealing with dynamic electricity prices due to its capability to optimize HVAC and MicroCSP energy flows by knowing the upcoming electricity price changes and acting accordingly.

Energy storage sizing effect

† Proper energy storage sizing is essential to optimize the electrical cost and the energy consumption of the building HVAC system. Indeed, adding a TES system to the MicroCSP increases the energy saving by almost 4% and the cost saving by almost 10%. These numbers are only applicable to the conditions studied in this thesis and can change when LMP profile or outdoor weather conditions change. Overall, the capacity of TES needs to be chosen carefully to

avoid unnecessary oversizing since after reaching the optimal capacity, the cost and energy savings do not change any more even if the capacity is increased.

Prediction uncertainty and seasonal variation effects

† Monte Carlo analysis results show that, by utilizing MicroCSP and applying EMPC, the HVAC energy saving ranges from 34% to 42% while applying CMPC saves the HVAC cost between 68% and 72% even in the presence of variations and prediction uncertainty, compared to using RBC.

2.5 Exergy Based Model Predictive Control (XMPC) Framework Design, Results and Analysis

2.5.1 Structure of the Designed Exergy Based Model Predictive Control (XMPC)

According to SLT, the second law efficiency (η_{II}) is defined as:

$$\eta_{II} = \frac{\dot{X}_{rec}}{\dot{X}_{sup}} = 1 - \frac{\dot{X}_{dest}}{\dot{X}_{sup}} \qquad (2.28)$$

where, $\dot{X}_{rec}$, $\dot{X}_{sup}$ and $\dot{X}_{dest}$ are the rate of exergy recovered, supplied and destroyed, respectively.

From Equation (2.28), it is clear that reducing the exergy destruction or increasing the exergy recovered when the exergy supplied is constant will increase the second law efficiency of the system. Therefore, in this study, the optimizer decreases the exergy destruction in the building while increasing the exergy recovered in the ORC, along with meeting comfort and system constraints.

Fig. 2.12 shows the structure of the XMPC framework designed for optimal exergy-based control of the combined building HVAC and MicroCSP systems. To minimize the building HVAC system's exergy destruction and to maximize the MicroCSP system's recovered exergy, the objective function is formulated as shown in Equation (2.29) subject to the constraints listed in Equations (2.30a) through (2.30j). The optimization problem is solved at each time step, to find the current; and future values of the temperature of the supply air (T^{Su}), the mass flow rate of HTF from the TES ($\dot{m}_{tes}$), and the pressure ratio of ORC (r_p). Here, soft constraints are used by adding slack variables (ϵ) and multiplying the slack variables by a weight factor (α) to ensure the room air temperature converges to a optimal solution (i.e., to be within the comfort temperature bound) all the time. The inputs for the XMPC optimization model are the forecast of ambient temperature and solar irradiation. ANSI/ASHRAE Standards are used to set the room air temperature comfort bounds and the ventilation requirements.

$$\min_{T^{Su}, r_p, \dot{m}_{tes}} \{\dot{X}_{dest}^b - \dot{X}_{rec}^{ORC} + \alpha(|\bar{\epsilon}|_1 + |\underline{\epsilon}|_1)\} \tag{2.29}$$

Subject to the following constraints:

$$T_{t+k+1|t} = AT_{t+k|t} + BT_{t+k|t}^{Su} + Ed_{t+k|t} \tag{2.30a}$$

$$T_{t+k|t}^r = CT_{t+k|t} \tag{2.30b}$$

$$P_{ORC,t+k|t} = f(\dot{m}_{tes_{t+k|t}}, r_{p_{t+k|t}}) \tag{2.30c}$$

$$\dot{Q}_{ORC,t+k|t} = g(\dot{m}_{tes_{t+k|t}}) \tag{2.30d}$$

$$SOC_{t+k+1|t} = SOC_{t+k|t} + \frac{(\dot{Q}_{PTC_{t+k|t}} - \dot{Q}_{TES_{t+k|t}}).\Delta t}{C_{TES}} \tag{2.30e}$$

$$\underline{SOC} \leq SOC_{t+k|t} \leq \overline{SOC} \tag{2.30f}$$

$$0 \leq \dot{m}_{tes_{t+k|t}} \leq \dot{m}_{max} \tag{2.30g}$$

$$T_{t+k|t}^{AHU} \leq T_{t+k|t}^{Su} \leq \bar{T}_{t+k|t} \tag{2.30h}$$

$$\underline{T}_{t+k|t}^r - \underline{\epsilon}_{t+k|t} \leq T_{t+k|t}^r \leq \bar{T}_{t+k|t}^r + \bar{\epsilon}_{t+k|t} \tag{2.30i}$$

$$\underline{\epsilon}_{t+k|t}, \bar{\epsilon}_{t+k|t} \geq 0 \tag{2.30j}$$

Where, the time index $t + k|t$ represents the predicted value of the variable at the time $t + k$ evaluated at the current time t. Equations (2.30a) and (2.30b) constitute the building's state-space dynamic model; (2.30c) and (2.30d) represent the ORC model; (2.30e) shows the SOC calculation of TES; (2.30f) binds the SOC of TES to the lower and upper values; (2.30g) is used to limit the ORC evaporator mass flow ($\dot{m}_{max}$) as per the manufacturer [94]; (2.30h) is the temperature constraint of the supply air of the HP; (2.30i) is the constraint to keep air temperature of the room within the comfort bound; finally, (2.30j) includes the constraint which ensures that

64
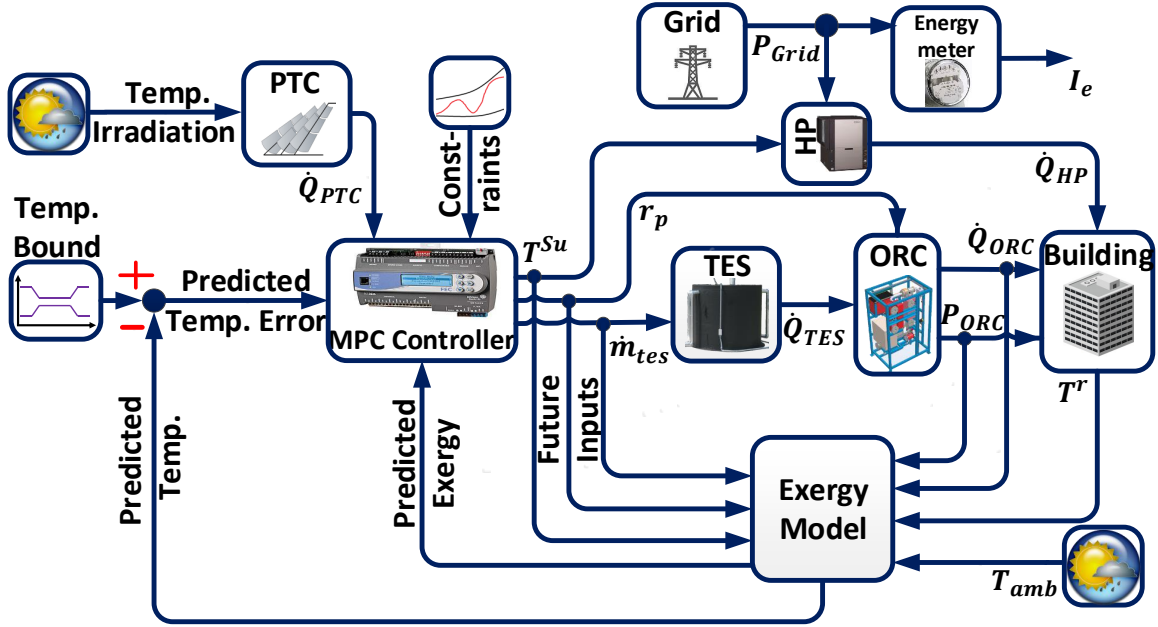
Figure 2.12: Structure of the designed XMPC to minimize both the exergy destruction, and the grid electrical energy consumption of the combined MicroCSP system and HVAC system in the building.

the slack variables are either zero or positive. It should be noted that k varies from 0 to the prediction horizon. When $k = 0$, the optimiser assigns the current value of the variables to the HP, TES and ORC (see Fig. 2.12). When $k \neq 0$, the optimiser assigns the future predicted values of the variables to the exergy model (see Fig. 2.12). The optimizer assigns the current and future values of the variables in real-time at the current time t such that the exergy destruction of the system (see Equation 2.29) is minimised.

2.5.2   Exergy Based Model Predictive Control (XMPC) Results

MATLAB® was used to implement the mathematical and optimization models from Sections 2.3 and 2.5.1. The measured ambient temperature, and the solar DNI for a sample cold and sunny winter day in Houghton, MI, USA were considered for simulations, as shown in Fig. 2.13. The update rate is selected as 30 minutes for both RBC and XMPC due to slow thermal dynamics of rooms.

YALMIP Toolbox [107] was used for XMPC formulation and implementation in MATLAB®. The prediction horizon of 24 hours (i.e., 1 day) was applied, and the default solver of YALMIP Toolbox [107], FMINCON was utilized. The optimization problem was run in a computer with Intel® Core™ i7-8700K CPU @ 3.7GHz with 32GB of RAM and the computation time was 184 seconds. The weight factor (α) for the slack variables in Equation (2.29) were tuned to get optimal room air temperature. The impact of α on the optimizer can be summarized as:

† If α tends towards 0, then the exergy destruction (and hence the grid electrical energy consumption) of the system will be minimum but room air temperature will violate the comfort temperature bounds. This is because the optimizer will not find a feasible solution satisfying all the constraints.

† If α tends towards infinity, then the optimizer will satisfy the constraints but the solution found will not be optimal. This is because the optimizer will minimize the room air temperature violations against the comfort temperature bounds with a higher priority than minimizing the exergy destruction (and hence the grid electrical energy consumption) of the system.

† Tuning α in between the above two cases will enable the optimizer to minimize the exergy destruction (and hence the grid electrical energy consumption) of the system and also satisfy the constraints.

The total energy consumption ($I_{e,t}$) of all thermal zones for the sample day is given by Equation (2.11). The total exergy destruction ($X_{dest,t}$) of the building HVAC and the ORC systems for the sample day is given by:

$$X_{dest,t} = \sum_{t=0}^{t} \dot{X}_{dest_t}^{ORC} \cdot \Delta t + \sum_{t=0}^{t} \sum_{i=1}^{N_{zones}} \dot{X}_{dest_{i,t}}^{b} \cdot \Delta t \qquad (2.31)$$

2.5.2.1 Rule-Based Control (RBC)

This section presents the results of RBC for the combined building HVAC and MicroCSP systems. RBC provides the baseline for comparison with the designed exergy-based controller. The rules of the designed RBC are:
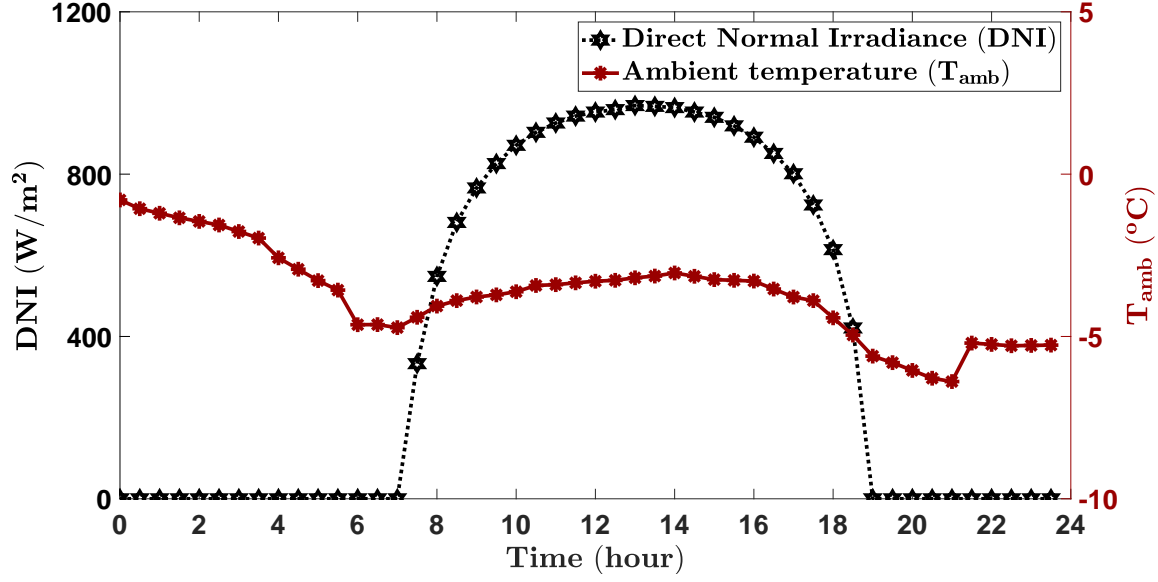
Figure 2.13: Solar irradiation in the form of direct normal irradiance (DNI) and outdoor ambient temperature (T_{amb}) measured every half hour for a sample cold and sunny winter day (18th March 2016) in Houghton, MI, USA.

$$
T_{i,t}^{Su} = \begin{cases}
T_{i,t}^{AHU} & \text{if } T_{i,t}^{r} > \bar{T}_{i,t}^{r} \\[2ex]
\bar{T}_{i,t} & \text{if } \underline{T}_{i,t}^{r} \leq T_{i,t}^{r} \leq \bar{T}_{i,t}^{r} \text{ AND } T_{i,t-1}^{Su} = \bar{T}_{i,t-1} \\[2ex]
T_{i,t}^{AHU} & \text{if } \underline{T}_{i,t}^{r} \leq T_{i,t}^{r} \leq \bar{T}_{i,t}^{r} \text{ AND } T_{i,t-1}^{Su} < \bar{T}_{i,t-1} \\[2ex]
\bar{T}_{i,t} & \text{if } T_{i,t}^{r} < \underline{T}_{i,t}^{r}
\end{cases}
\tag{2.32}
$$

Fig. 2.14(a) shows the temperature of the air supplied from the HP and the temperature of the room air of a sample room for the operating conditions in Fig. 2.13. As seen from Fig. 2.14, the air temperature of the room starts at 21°C and ramps down till it reaches below the lower temperature bound. The air temperature of the room

then violates the lower comfort temperature bound from hour 7:00 to 7:30. This is because, even though the room air temperature violation occurs at 7:00, the control action occurs at the next time step 30 minutes later. From hours 8:30 to 19:30, the thermal power from PTC (Fig. 2.14(b)) maintains the air temperature of the room within the comfort temperature bounds, while the HP is switched off. RBC does not have control on the TES, i.e. if the power output of the PTC is less than the maximum capacity of the ORC input, then the power output of the PTC is the same as the power input to the ORC. The ORC operates at its maximum capacity when the power output of the PTC is greater than the maximum capacity of the ORC input and the difference between the PTC output and the maximum capacity of the ORC input is stored in the TES and used at a later time. The electrical and thermal powers from the ORC are shown in Fig. 2.14(c). After hour 19:30, the room air temperature ramps down till it reaches the lower temperature bound at about 20:00. Once the room temperature reaches the lower bound, the HP switches on again after the next time step 30 minutes later and ramps up the room air temperature to above the lower comfort bound. Then, the room temperature ramps down but is within the comfort bounds. Fig. 2.14(d) shows the power consumed by the HP from the grid and the SOC of the TES. The power consumed from the grid reflects the periods when room is heated by the HP (i.e., from hours 7:30 to 8:00 and hours 20:30 to 21:00). SOC of the TES increases from hours 15:00 to 18:00 when the thermal input from the PTC is greater than the ORC capacity ($60\ kW$) and the thermal power accumulated in the

TES is used from the hours 18:30 to 19:30 when there is no thermal power produced by the PTC. Fig. 2.14(e) shows the exergy destruction rate of the combined building HVAC system and ORC system. The exergy destruction rate increases when heat is applied to the room and hence we see that the profile of the exergy destruction rate of the building HVAC system and the ORC system is similar to the supply air temperature to the room. As will be explained later, the portion of the exergy destruction by the ORC is significantly less than that by the HVAC system.

2.5.2.2 Exergy-Based Model Predictive Control (XMPC)

The air temperature of the supply air from the HP and the temperature of the room air for the same conditions of Fig. 2.13 are shown in Fig. 2.15(a). During the unoccupied time (i.e., from 0:00 to 7:00), it can be seen that the HP is switched off, while the air temperature of the room is within the comfort temperature bounds. Then, during the early morning, at the start of the occupied time, (i.e., from 7:00 to 8:30), the optimizer turns on the HP and heats the room gradually to ensure that the room air temperature is maintained at the lower comfort temperature bound. It should be noted that, the XMPC, unlike RBC (see difference in Figs. 2.14(a) and 2.15(a)), does not overheat the room as (1) XMPC will consider the future solar-thermal energy available, and (2) will consider the room thermal dynamics and aim to minimize the exergy destruction of the room. Further during the occupancy mode (i.e., from 8:30
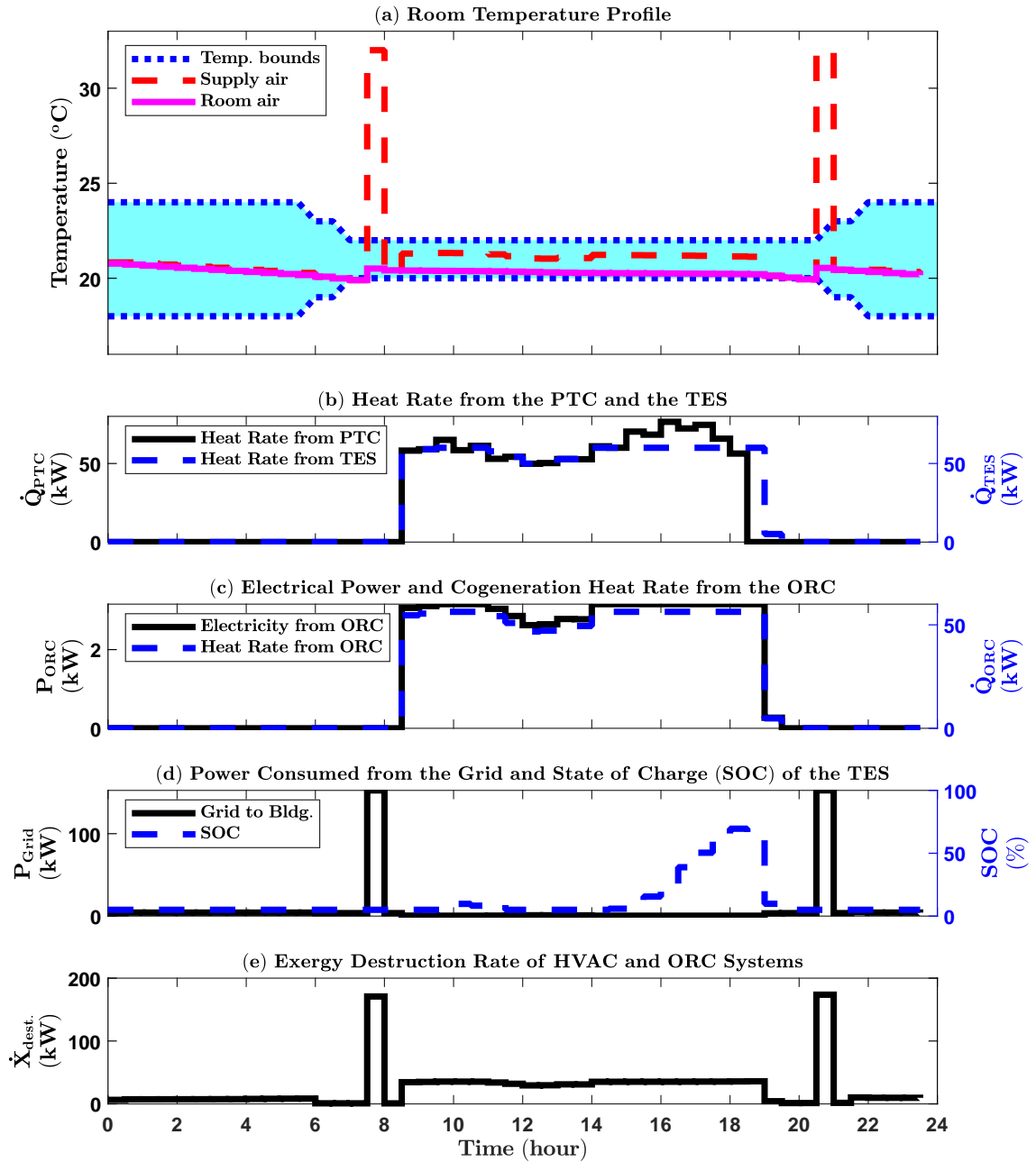
Figure 2.14: <u>RBC results</u> for the sample day shown in Fig. 2.13.

to 20:30), the optimizer tries to keep the air temperature of the room at the lower

comfort temperature bound by utilizing the solar-thermal energy and supplying the

minimum heat needed from the HP. After hour 20:30, the air temperature of the

room ramps down within the comfort temperature bounds. Fig. 2.15(b) depicts the heat rate produced by the PTC, and the heat rate from the TES to the ORC. The power consumed by the HPs from the grid and the SOC of the TES are shown in Fig. 2.15(d). Power consumed by the HP from the grid occurs when there is no thermal power from the TES and the optimizer has to turn on the HP. The power consumed from the grid is always greater than zero whenever ORC is not operating at its maximum capacity ($\dot{Q}_{TES} = 60 \ kW$) due to HVAC ventilation fan power demand. When ORC is operating at its maximum capacity, the electrical power from ORC (P_{ORC}) satisfies the HVAC ventilation fan power demand and hence power demand from the grid becomes zero. The optimizer stores a portion of the thermal power from the PTC from hours 15:00 to 18:00 leading to the increase in SOC of the TES. This is to meet the constraint which does not allow the thermal input from the PTC to be greater than the ORC capacity (60 kW). This thermal power accumulated in the TES is used from the hours 18:30 to 19:30 when there is no thermal power produced by the PTC. The total exergy destruction rate of the building HVAC system and the ORC system is shown in Fig. 2.15(e). The exergy destruction rate of the building is always positive even when there is no supply air from the ORC or HP (i.e., from hours 0:00 to 7:00 and from hours 20:30 to 23:30) due to the heat transfer from the room to the outdoors. The exergy destruction rate increases from hours 7:00 to 8:30 and hours 19:00 to 20:30 due to supply air from HP to the building. The exergy destruction rate further increases from hours 8:30 to 19:00 due to (1) the supply air from the

72

Table 2.4

Comparison for the effects of control framework on grid electrical energy
consumption, exergy destruction, and discomfort index[1] for the sample day
in Fig. 2.13.

Control Type	Elec. Cons. [kWh]	Elec. Cons. Reduction* [%]	Exergy Dest. [kWh]	Exergy Dest. Reduction* [%]	Discomfort Index [$°Ch$]	Discomfort Index Reduction* [%]
RBC	208.7	-	606.8	-	0.15	-
XMPC	114.1	45.4	503.6	17	0.00	100.00

* Percentages are calculated by comparing with the baseline RBC.

[1] The discomfort index (I_d) is defined as a metric to account for the room air temperature
violations against the comfort temperature bounds and is given by [113]:

$$I_d = \sum_{t=0}^{t_f} min(|T_t^r - \underline{T}_t^r|, |T_t^r - \bar{T}_t^r|) \cdot 1_{\mathcal{B}^c(t)}(T_t^r)$$

where, $\mathcal{B}(t) = [\underline{T}_t^r, \bar{T}_t^r]$ is the comfort temperature bounds at time t; $1_{\mathcal{B}^c(t)}$ is the indicator
function of its complement $\mathcal{B}^c(t)$.

ORC increases the exergy destruction rate of the building; and (2) irreversibilities

associated with the ORC operation.

The total energy consumption, exergy destruction, and discomfort index of all thermal

zones for the sample day are listed in Table 2.4 and compared for the designed XMPC

framework against the baseline RBC for the combined HVAC and MicroCSP systems.

Table 2.4 shows that the designed XMPC framework leads to 45.4%, 17%, and 100%

reductions in energy consumption, exergy destruction, and discomfort index compared

to the baseline RBC.

Table 2.5 further differentiates the total exergy destruction content of the overall

system between the exergy destruction of the building HVAC system and the exergy

destruction of the ORC system. Comparing Tables 2.4 and 2.5 shows that (i) when

RBC is applied, the exergy destruction of the building HVAC system contributes a higher percentage of the total exergy destruction of the overall system, and (ii) moving from RBC to the designed XMPC, the reduction in exergy destruction of the building HVAC system is more sensitive to the total reduction in the exergy destruction of the overall system. The reduction in exergy destruction of the overall system translates to a reduction in overall energy demand of the building HVAC system and at the same time increases the available energy of the ORC. These lead to the reduction in grid electrical energy consumption.

Furthermore, the reduction in grid electrical energy consumption from RBC to XMPC can be understood from the exergy balance sankey diagram in Fig. 2.16. The electrical energy from the grid is treated as pure exergy (i.e., electrical energy content is the same as electrical exergy content). In Fig. 2.16, the notion of 100% refers to the total exergy supplied when RBC is applied to the combined building HVAC system and the MicroCSP system. In Fig. 2.16, exergy destruction of the fan is calculated

Table 2.5
Exergy destruction contribution by the building and ORC for the sample
day in Fig. 2.13.

Control Type	Exergy Dest. of Building [kWh]	Exergy Dest. Reduction* [%]	Exergy Dest. of ORC [kWh]	Exergy Dest. Reduction* [%]
RBC	450	-	156.7	-
XMPC	362.6	19.4	141.0	10.1

* Exergy destruction reduction percentages are calculated by comparing with the baseline RBC.
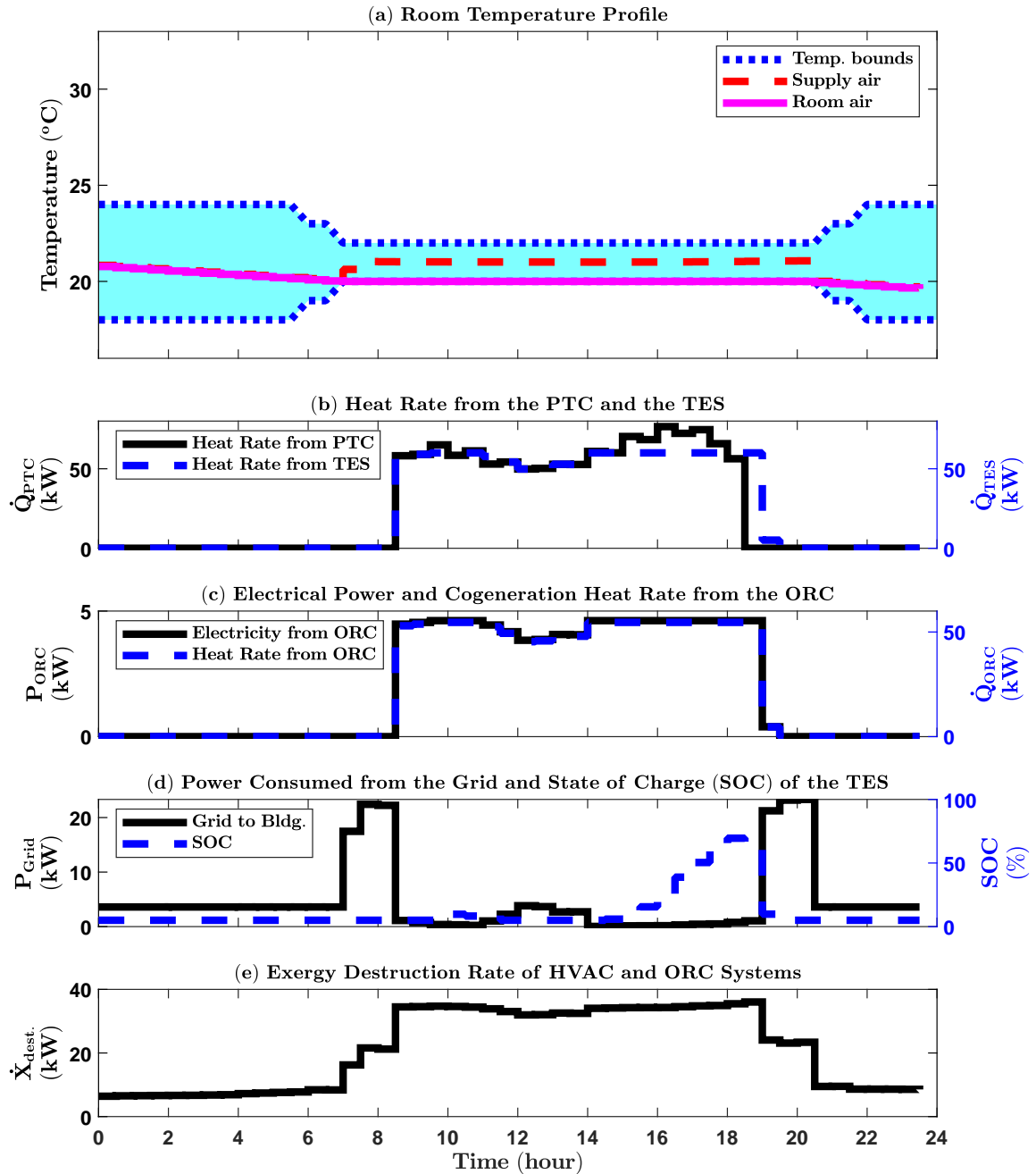
Figure 2.15: <u>XMPC results</u> for the sample day shown in Fig. 2.13.

using Equation (2.12a). Exergy destruction of the ORC is calculated using Equation (2.9). Exergy destruction due to heat loss from the building is calculated using the first term on the right hand side of Equation (2.22). Exergy destruction due to mass
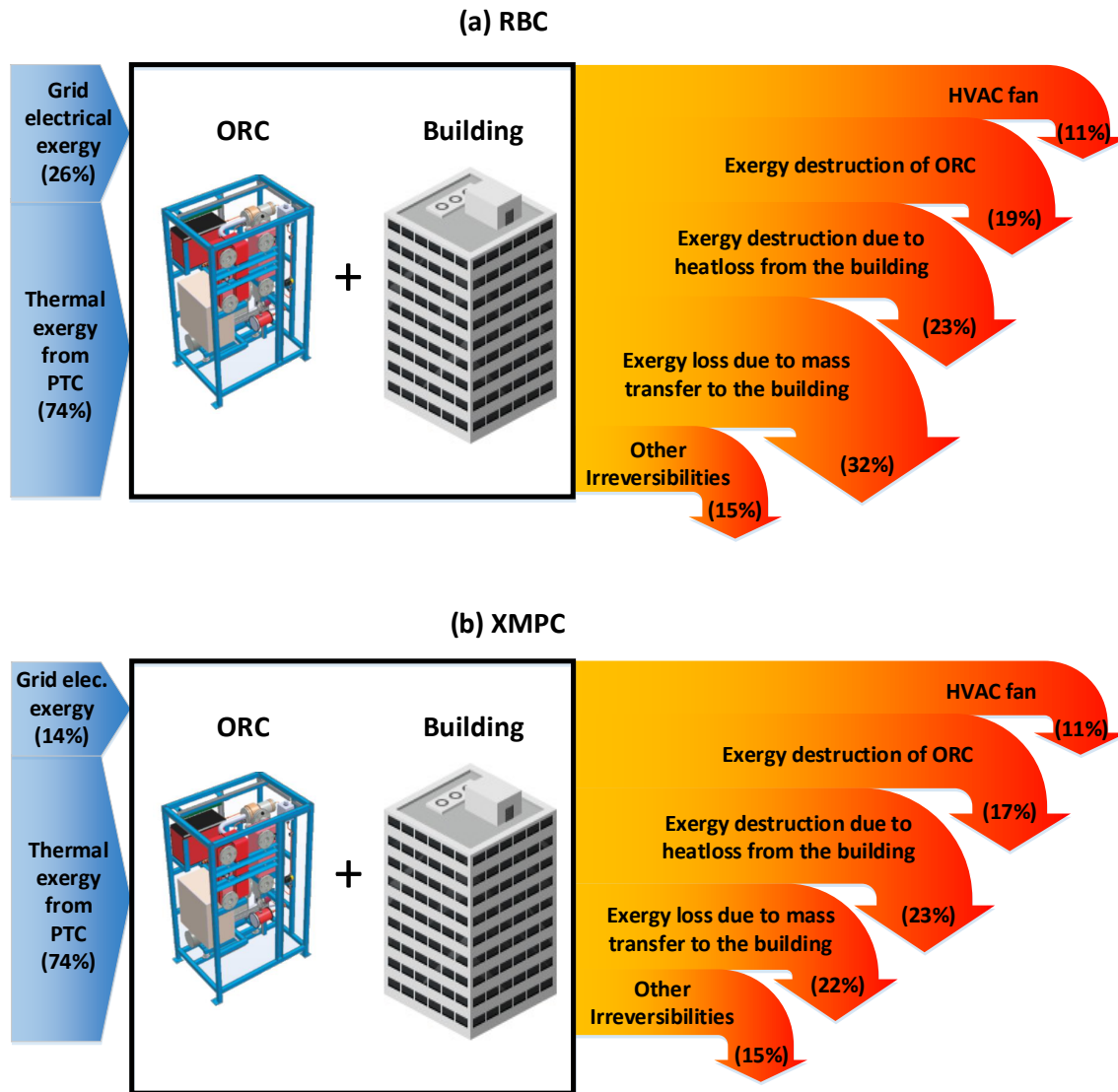
Figure 2.16: Exergy balance of the building and the ORC system for the sample day shown in Fig. 2.13 using two different control frameworks. All percentages in the figure are calculated with reference to the total exergy input to the system in the case of RBC.

transfer to the building is calculated using the second and third term on the right hand side of Equation (2.22). Other irreversibilities are calculated as the difference between the total exergy supplied and total exergy destroyed (See Equation (2.31)). In both the RBC and XMPC cases, the thermal exergy input to the ORC is the same

because the same sample day (Fig. 2.13) was applied to both cases. However, the electrical exergy (or energy) reduces by 12% when we move from RBC to XMPC. This is attributed to:

† 10% less exergy destruction in the building due to reduction in mass transfer of unnecessary hot air input to the building; and

† 2% less exergy destruction in the ORC due to a more efficient operation of the ORC by selecting optimum pressure ratio (r_p).

In essence, the 12% reduction in the exergy destruction in the building and the ORC system leads to a minimal use of the HP through optimum coordination of energy demand and supply by knowing upcoming available thermal and electrical energies from the Solar source and the HVAC required heat by knowing building thermal dynamics. This optimum coordination results in 45% lesser electrical energy requirement from the grid by using XMPC versus the baseline RBC (Table 2.4).

2.5.2.3 Effects of Number of HVAC Zones in the Building and Thermal Energy Storage (TES) Capacity

The results presented in Sections 2.5.2.1 and 2.5.2.2 are for the building with 72 HVAC zones and TES capacity of 48 kW.h. In this section, grid electrical energy

and the second law efficiency for the designed XMPC are calculated by varying the number of HVAC zones in the building and also by varying the TES capacity.

Fig. 2.17(a) shows that if the number of HVAC zones of the building is increased without changing the TES capacity of the MicroCSP, the optimal configuration includes seventy two HVAC zones. At seventy two HVAC zones in the building, the ORC operates optimally to utilize the highest possible energy from PTC (i.e., the ORC shows minimum exergy destruction) for the given sample day, and room temperature conditions. As the number of HVAC zones is increased in the building, the grid electrical energy consumption increases to compensate for the increase in HVAC demand. This increase in grid electrical energy consumption amplifies the amount of exergy supplied, but the exergy destroyed by the building also increases. This increase in exergy destroyed is greater than the rise in exergy supplied. This is because exergy supplied is a function of the grid electrical energy increase but exergy destroyed in the building is a function of the co-generated thermal energy from the ORC, and the thermal energy from the HP (grid electrical energy multiplied by COP of the HP). Hence the second law efficiency reduces (see Eq. (2.28)). As the number of HVAC zones is reduced, the grid electrical energy decreases but so does the second law efficiency. This is because, the ORC does not operate optimally and hence the grid electrical energy also does not decrease to its full potential to compensate for this reduction in ORC electrical energy. This causes the exergy destruction to drop at a smaller rate than the exergy supplied and hence the second law efficiency reduces.

Fig. 2.17(b) shows the importance of including a TES and the importance of TES sizing to get the optimal second law efficiency and the maximum energy savings. Fig. 2.17(b) shows that if we increase the TES capacity without adding the number of HVAC zones in the building, the grid electrical energy consumption decreases, and the second law efficiency increases. However, the drop in grid electrical energy consumption and the increase in second law efficiency saturates after the TES capacity is "large enough" for the ORC to operate optimally. For the ORC to operate optimally, the TES capacity should be large enough to store the thermal energy from the PTC and dispatch it to the ORC when demanded. Without TES, the ORC does not operate optimally and grid electrical energy consumption also rises to compensate for this reduction in ORC electrical energy. This increases the exergy destroyed while the exergy supplied will remain almost constant and hence the second law efficiency reduces (see Eq. (2.28)). This phenomenon is slightly improved by having a small TES (i.e., 24 kW.h), but the full potential is only realized when TES capacity is 48 kW.h. Any increase in TES capacity beyond this, will not show any major impact on grid electrical energy consumption or second law efficiency.

These results show the importance of proper sizing of the TES and the number of HVAC zones in the building for given PTC and ORC systems.
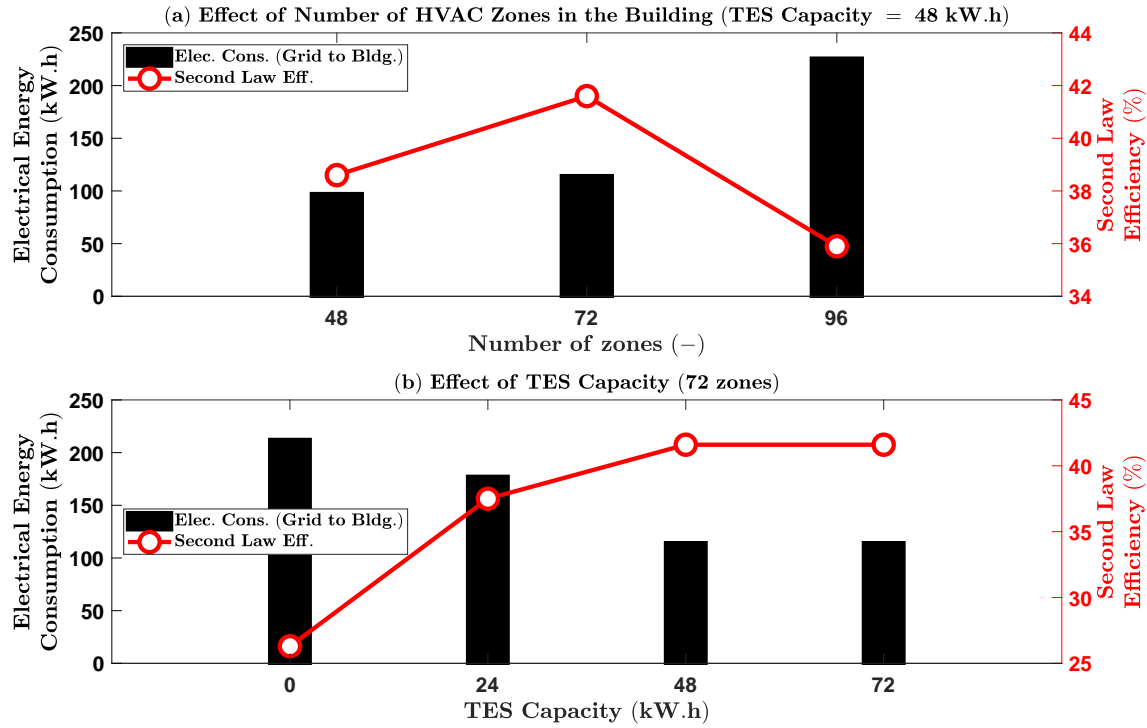
Figure 2.17: Effects of total HVAC zone number in the building and TES capacity on grid electricity consumption and second law efficiency of the system.

2.5.2.4 Uncertainty Quantification by Monte-Carlo Simulations (MCS)

The results presented in sub-sections 2.5.2.1 and 2.5.2.2 are for a cold and sunny winter sample day (Fig. 2.13). However, uncertainties in the future predictions of the solar irradiation, and the ambient temperature for the sample day which the controller requires (Fig. 2.12) were not considered. Furthermore, to quantify the controller performance for the whole of the winter season, seasonal variations of the solar irradiation, and the ambient temperature needs to be accounted for. Hence, in this
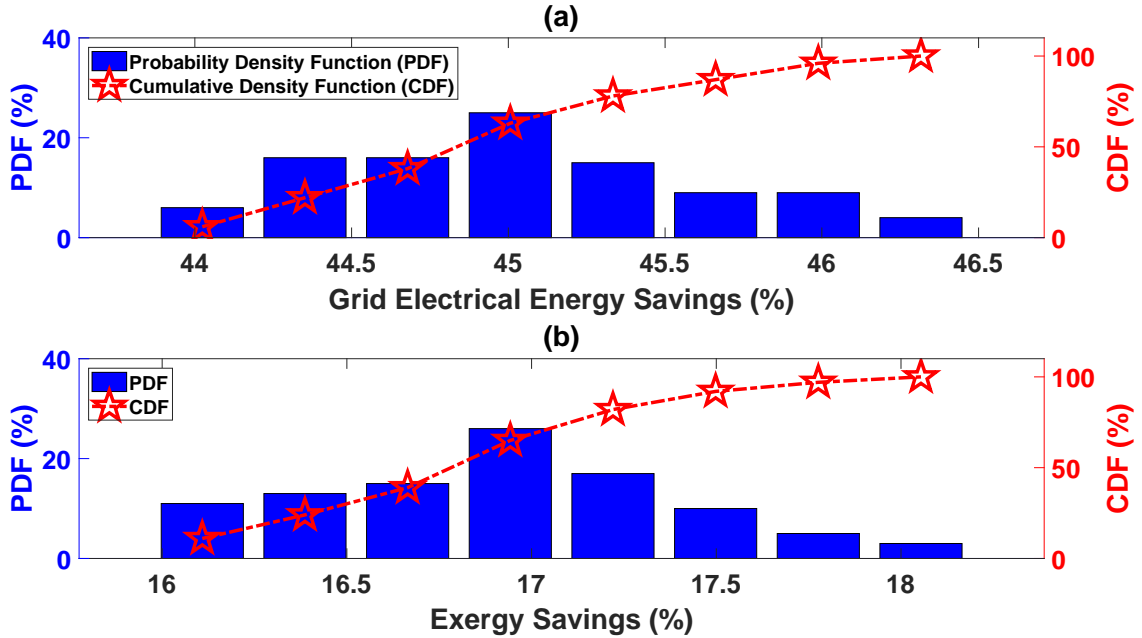
Figure 2.18: Monte-Carlo simulations showing the probability of grid electrical energy and exergy savings by moving from **RBC to XMPC** after **accounting for prediction uncertainties** of the controller inputs.

section, a probability analysis using MCS was carried out to account for the uncertainties and the variations discussed. These simulations show possible outcomes for the reduction in energy consumption and exergy destruction, along with the likelihood of each outcome.

Fig. 2.18 and Fig. 2.19 show the probability distribution of savings in energy consumption and exergy destruction of the building HVAC and MicroCSP systems when the designed XMPC is used compared to when the RBC is used. The inputs for the MCS used to generate Fig. 2.18 account for uncertainties in prediction of the solar irradiation, and outdoor ambient temperature for the sample sunny and cold winter

day. The prediction uncertainties are generated by adding a white noise of signal-to-noise ratio of 5 dB to the inputs shown in Fig. 2.13 and random inputs are generated, based on a prior study [23]. Hundred random inputs were generated and MCS was carried out for each case. The results show that the savings in energy consumption and exergy destruction do not go below 44% and 16%, respectively. Furthermore, Fig. 2.18 shows that, there is 50% likelihood of reducing energy consumption and exergy destruction by over 45% and 17%, respectively.

The inputs for the MCS used to generate Fig. 2.19 account for seasonal variations of the solar irradiation, and ambient temperature for the sample winter day. To account for the seasonal variation, the solar irradiation data and outdoor ambient temperature data were taken for Houghton, MI, USA from September to April of the 2015-16 winter from the US National Renewable Energy Lab website [114]. Hundred random inputs were generated and MCS was carried out for each case. The results show that the savings in energy consumption and exergy destruction do not go below 35% and 14%, respectively. Furthermore, Fig. 2.19 shows that, there is 50% likelihood of reducing energy consumption and exergy destruction by over 43% and 18%, respectively.
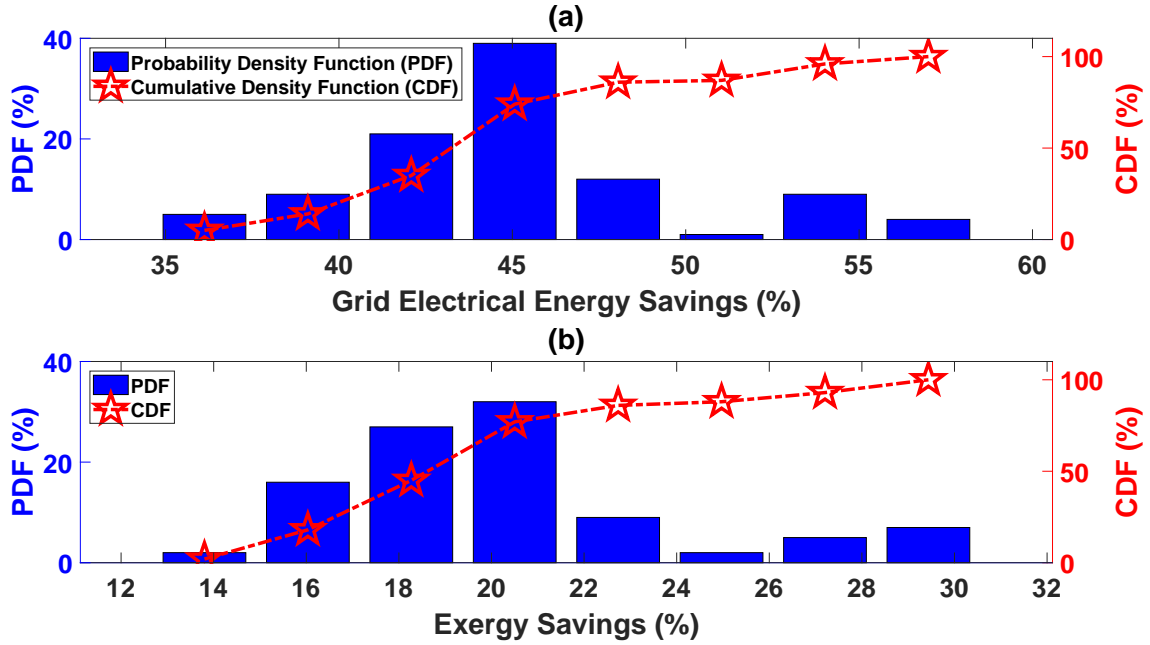
Figure 2.19: Monte-Carlo simulations showing the probability of grid electrical energy and exergy savings by moving from **RBC to XMPC** after **accounting for seasonal variations** of the controller inputs.

2.5.3 Summary and Conclusions

The Section 2.5.2 shows the study undertaken to design an XMPC framework to minimize the grid electricity consumption of the HVAC system in the building when integrated with a MicroCSP system. Control-oriented models, based on FLT and SLT, were developed for a MicroCSP system and then integrated into the FLT and SLT based models of the HVAC system in the building. The resulting integrated model was incorporated into a predictive control framework to optimally co-ordinate the thermal and electrical energy flows in accordance to HVAC system needs in the building. The main findings from this study for the case studies in this work are

summarized as:

† The designed XMPC framework can provide 17% reduction in the exergy destruction of the MicroCSP + HVAC system, which leads to a 45% reduction in the grid electrical energy for the HVAC system, compared to the applied rule-based controller (RBC) for the MicroCSP system and HVAC system in the building.

† The designed XMPC framework can reduce the exergy destruction in building by 10% due to mass transfer and in ORC by 2% due to operation irreversibilities, when compared to the overall exergy supplied to the MicroCSP system and HVAC system in the building when RBC is applied to the MicroCSP system and HVAC system in the building.

† It is critical to properly size the TES capacity and the HVAC zones in the building for a given MicroCSP system. The results show that the optimal second law efficiency of the system is obtained at 72 HVAC zones, and 48 kW.h of TES capacity for the given PTC and ORC systems.

† The exergy savings of the system vary from 16% to 18% by considering the uncertainties in the future prediction of the solar irradiation, and the ambient temperature for the sample day, which results in a grid electrical energy reduction from 44% to 47%. Furthermore, when we consider the seasonal variations of the solar irradiation, and the ambient temperature, the exergy savings of the

system vary from 13% to 30%. This leads to a grid electrical energy reduction from 35% to 58%.

Chapter 3

Model Predictive Control for Internal Combustion Engines and Waste Heat Recovery System[1]

3.1 Introduction

According to the recent United States Energy Information Administration (EIA) report [15], 31% of the total CO_2 emissions in the US in 2019 was caused by the transportation sector. However, 75% of the transportation sector is primarily driven

---

[1]This results from this chapter are based on Reddy et al. publications on Energy Based MPC for (1) Transportation Sector in [7] and (2) Building Sector in [8].

by internal combustion engines (ICEs). This includes ICEs used in over 90% of on-road vehicles in 2019 in the US. The report further predicts that in 2050, 65% of the transportation sector would be primarily driven by ICEs. The report further showed another significant application of the ICEs in the building sector. Additionally, the building sector accounted for two-thirds of the electricity consumed in 2019 in the US. ICEs used for customer-owned electricity generation accounted for 6% of the total electricity used by buildings. The report predicts that the customer-owned electricity generation in buildings is only going to increase from now till 2050. In addition, authors in reference [16] argue in favor of customer-owned electricity generation when considering the economic feasibility of off-grid electricity usage in rural areas where the grid is not yet extended. Furthermore, ICE based power generators are used as the main back-up electricity source in grid connected buildings [17]. Increasing environmental calamities causing disruption to the power grid makes the 12 billion USD global generator industry stronger [18, 19]. All these reasons show the significant application of the ICE, demand for minimizing the energy usage in ICE systems and make them more energy efficient.

One way to make ICE more energy efficient is by using a waste heat recovery (WHR) system. In an ICE, around a quarter of the input fuel energy is wasted as thermal energy by the exhaust gases leaving the ICE [56]. A WHR system converts this wasted thermal energy to a usable form of energy [57]. In a WHR system, a heat exchanger (HE) transfers the thermal energy from exhaust gas to a heat engine [58]

or a thermo-electric generator (TEG) [59]. In a TEG, thermal energy is directly converted to electricity using semi-conductors. The heat engine generally used in WHRs is an organic Rankine cycle (ORC) device which converts thermal energy to mechanical energy. The choice of the prime mover in a WHR system is mainly dictated by the size and the operating temperatures of the ICE [60]. Chapter 3 focuses on an ORC driven WHR system owing to the size of the ICE used in this thesis.

Fig. 3.1 shows an overview of the literature on the combined ICE and WHR systems. Fig. 3.1 shows that, a lot of studies have been carried out on the (i) design [115, 116, 117], (ii) energy based analysis [59, 118, 119], (iii) exergy based analysis [120, 121, 122, 123], (iv) model based optimization [124, 125, 126] and (v) experimental optimization [127, 128, 129] of combined ICE and WHR systems. But, very few studies explore the optimal control of the combined ICE and WHR systems. For example, the authors in references [130, 131, 132, 133, 134] propose the design of rule based control (RBC) frameworks for the combined ICE and WHR systems. But, an optimal control framework needs to be designed to realise the full potential of a combined ICE and WHR system [135]. The optimal control framework should consider (i) operating limits of the ICE, (ii) available exhaust gas energy from the ICE to WHR, (iii) operating limits of the WHR, and (iv) thermal requirements of the exhaust aftertreatment system. But the design of the rules or populating calibrated tables require significant calibration effort on the ICE and/or WHR test bench.
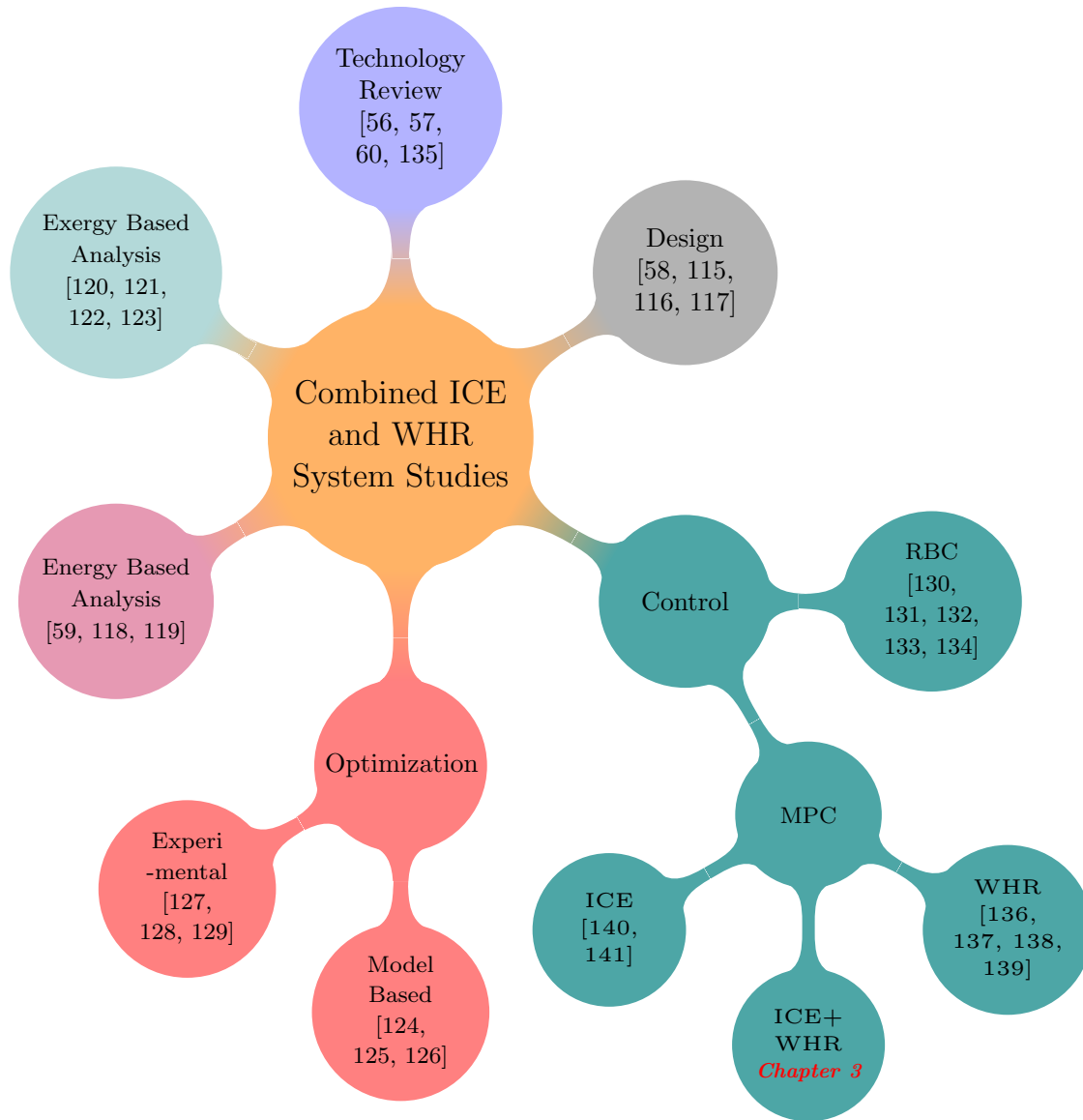
Figure 3.1: Overview of the ICE and WHR system studies.

Model predictive controllers (MPCs) have been successfully used for the optimal control of ICE systems [140, 141] and WHR systems [136, 137, 138, 139]. MPC, when applied to a combined ICE and WHR system, can:

† provide real-time optimal solution based on the current value and future predictions of the desired power;

† handle constraints on the operating limits of the air system, fuel system, ORC, and meet tailpipe emission requirements; and

† reduce the calibration effort required in the ICE and WHR test bench.

The literature review also shows that energy based analysis of the ICE + WHR can determine the energy flow through the ICE and WHR system. In other words, energy based analysis of the combined ICE and WHR system can minimize the fuel consumed by the ICE. However, exergy based analysis can determine the irreversibilities and the sources of entropy generation in the combined ICE and WHR system. This will allow the exergy based analysis to further minimize the fuel consumed by the ICE by minimizing the exergy destruction (unavailable energy) of the combined ICE and WHR systems. Exergy based analysis is more critical when trying to optimize different types of energies like the mechanical power from the ICE and the exhaust thermal energy from the ICE [142].

Hence in Chapter 3, we design energy based MPC (EMPC) and exergy based MPC (XMPC) frameworks for ICE + WHR to be used for transportation applications and building electricity generation. The EMPC and XMPC frameworks are designed to (i) reduce the fuel consumption of the ICE, and (ii) meet exhaust gas temperature

requirements for fast exhaust aftertreatment system light off. The results for the ICE are based on extensive experimentation on an actual 6.7 liter compression ignition engine at Michigan Technological University.

This Chapter is organized as follows. The experimental testbed is detailed in Section 3.2. Then, the mathematical models based on of the ICE, turbocharger (TC), HE, and ORC are explained in Section 3.3. The problem formulation, design, and control results of the EMPC for the combined ICE and WHR system for transportation and building electricity generations applications are explained in Sections 3.4 and 3.5, respectively. In addition, the problem formulation, design, and control results of the XMPC for the combined ICE and WHR system are discussed in Section 3.6. In Sections 3.4, 3.5 and 3.6, the designed EMPC, and XMPC are compared to a RBC applied to the ICE system without WHR and applied to the combined ICE and WHR system. In addition, the ability of the designed EMPC and XMPC are assessed to adapt to the exhaust gas temperature requirement.

3.2 Testbed

The ICE in this work is a turbocharged dual fuel natural gas-diesel engine in Advanced Power Systems Research Center of Michigan Technological University. Table 3.1 shows the technical specifications of the ICE. Fig. 3.2 shows the ICE experimental

setup. In the ICE, fresh air from the atmosphere is compressed, regulated, and cooled by the TC, throttle, and intercooler, respectively. The compressed air is mixed with natural gas, and part of exhaust gases via a mixer and by adjusting exhaust gas recirculation (EGR) valve. This mixture goes into the engine cylinders, where diesel fuel is directly injected. Combustion of air-fuels mixture causes the engine to produce power in a 4-stroke operation.

(a) Schematic of the engine test setup
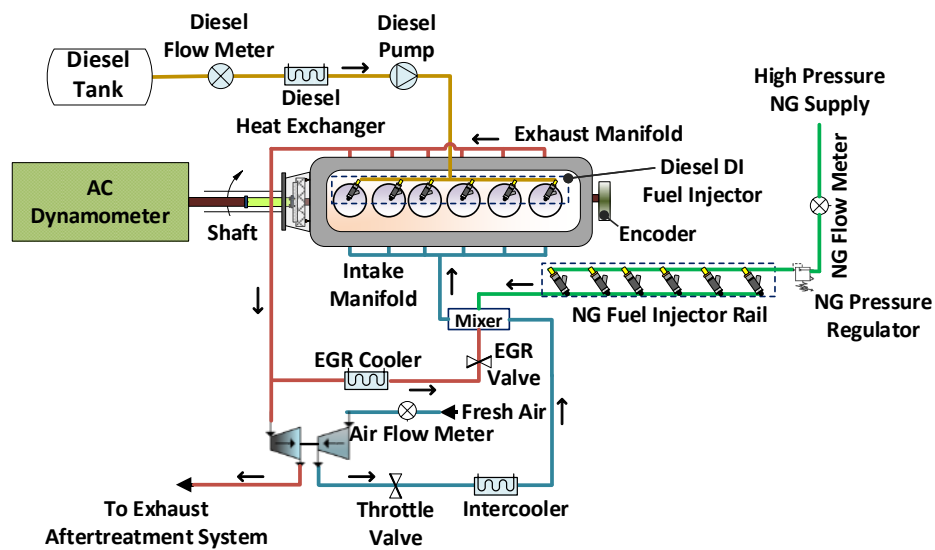
(b) Engine test cell
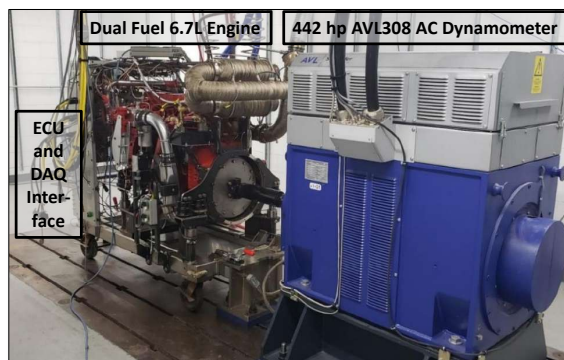
Figure 3.2: Experimental setup of the engine.

The ICE test unit is instrumented with six in-cylinder pressure transducers, three

AVL GH12D and three AVL GH15D, for combustion metrics analysis. The fuel flow measurement is done by two Micro Motion Coriolis Meter ELITE CMFS010P, one for the liquid diesel and the other for the compressed natural gas. All temperature measurements (i.e., intake manifold, exhaust gas, engine coolant) are made with type K thermocouples. Intake and exhaust pressures are measured by Omega Absolute Pressure Transducer MMA050V5P4D1T3A5CE. Other pressure measurements (i.e., oil pressure, fuel inlet) are done with Omega Gage Pressure Transducer GP50. The crank angle position is measured by a BEI encoder series H25D with 360 pulses per revolution; the load and speed are controlled by an AVL A/C Dynoroad 308/4 SX. Measurement errors include sensor accuracy and systematic error due to factors, such as electrical noise, signal conditioning, signal transmission, hysteresis. In order to mitigate these factors, several control points are taken during conducted engine testings, alongside with test repetitions. It has been observed an average measurement error for independent and dependent variables is below 3%.

In the ICE, exhaust gases from the cylinders enter the TC and then exit to the aftertreatment system. In this work, the WHR system is located between the TC and the aftertreatment system (Fig. 3.3). The WHR system is based on an experimental study done in references [143, 144]. Table 3.2 shows the technical specification of the WHR system. The WHR system consists of two sub-systems:

† Heat Exchanger - Transfers the thermal power from the exhaust gases to the

94

working fluid (WF) of the ORC.

† ORC System - Converts the thermal power from the WF of the ORC to usable mechanical power (P^{ORC}) for propulsion.

The total power output from the system will include $P^{ORC} + P^{ICE}$ (Fig. 3.3). This thesis focuses on optimizing ICE, TC, and WHR operations to minimize total fuel consumption, while meeting the requirements for the exhaust aftertreatment system.

Table 3.1
Engine technical specifications.

Model	Cummins ISB6.7 CM2250
Number of cylinders	6
Bore x Stroke	107 x 124 mm
Connecting rod length	192 mm
Displacement volume	6.7 L
Compression Ratio	15.0 : 1
Aspiration system	Turbocharged (Wastegate) + Charge Air Cooler + High Pressure EGR + Throttle Valve
Diesel Fueling System	Direct Injection 8 holes (168 mm diameter)
Natural Gas Fueling System	Single Point Injection Upstream of Intake Manifold 6 CNG injectors (Westport AEC 8 g/s)
Rated Power	231 kW (310 HP) @ 1800 RPM
Rated Torque	1230 Nm @ 1620 RPM
Peak BMEP	24 bar
Boost pressure at Peak BMEP	247 kPa
Minimum Throttling Pressure	70 kPa
Exhaust Temperature Range	350 to 870 °C
Peak Cylinder Pressure	<150 bar
Firing Order	1-5-3-6-2-4

Table 3.2

WHR system technical specifications.

Heat exchanger	203 mm diameter stainless steel shell and a 1275 mm long tube bundle with 101 stainless steel tubes.
ORC working fluid	Ethanol
Condenser fluid	50% water and 50% ethylene glycol mixture by weight
Pump	Vickers VMQ double-action 10-cc/rev vane pump
Turbo expander	Garret GT25 turbo expander (Modified for application)
Rated power	17 kW
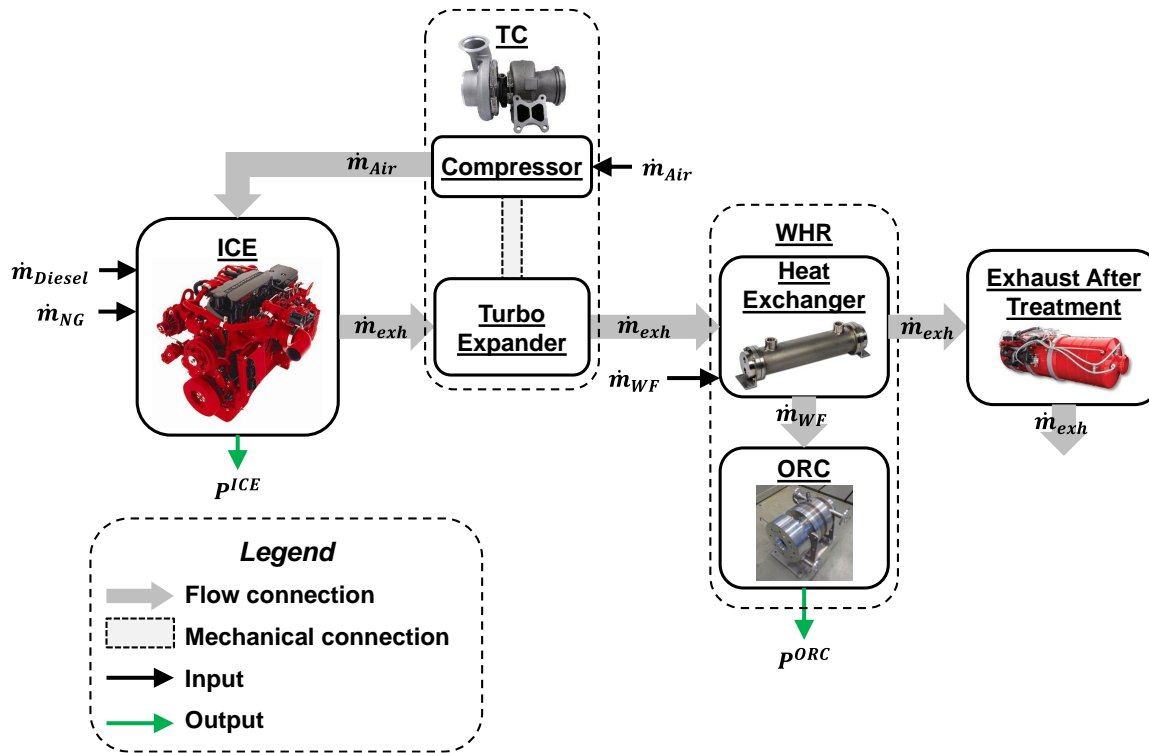
Figure 3.3: Power and mass flows in the ICE + WHR setup in this study.

3.3   Modeling

This Section describes the control oriented models of the ICE and WHR systems developed based on First Law of Thermodynamics (FLT) and Second Law of Thermodynamics (SLT); used for the studies in Sections 3.4, 3.5 and 3.6. Control oriented models are mathematical models of the system suitable for control studies. For example, control studies may favor a less (but reasonably) accurate model of the system requiring fewer parameters against a highly accurate but detailed model of a system requiring lots of geometrical parameters. In Chapter 3, the accuracy of the models developed are greater than 95% in the operating zone of the system.

3.3.1   IC Engine (ICE)

The ICE in Chapter 3 is modeled using measured data from the engine test cell (Fig. 3.2). The ICE torque (Tq^{ICE}) and exhaust gas temperature ($T_{exh}^{ICE,out}$) are modeled as functions of four engine variable inputs, including: diesel start of injection (SOI), manifold absolute pressure (MAP), diesel injection pressure ($DIPr$), and

diesel substitution ratio (DSR).

$$Tq^{ICE} = \Upsilon_1(MAP, SOI, DSR, DIPr) \qquad (3.1a)$$

$$T_{exh}^{ICE,out} = \Omega_1(MAP, SOI, DSR, DIPr) \qquad (3.1b)$$

However, the ICE power (P^{ICE}) is proportional to Tq^{ICE} and the angular speed of the ICE (ω^{ICE}). Hence, when ω^{ICE} is constant, P^{ICE} is calculated as:

$$P^{ICE} = \Upsilon_2(MAP, SOI, DSR, DIPr) \qquad (3.2)$$

It is worth noting that the functions Υ_1, Ω_1 and Υ_2 are quadratic and nonlinear. Υ_1, Ω_1 and Υ_2 are obtained by varying MAP, SOI, DSR, $DIPr$; tabulating the resulting Tq^{ICE}, $T_{exh}^{ICE,out}$, P^{ICE}; and developing a database model with 4 inputs and 1 output.

DSR represents the amount by which natural gas fuel has substituted diesel fuel. DSR is calculated by using natural gas ($\dot{m}_{NG}$) and diesel ($\dot{m}_{Diesel}$) mass flow rates:

$$DSR = \frac{\dot{m}_{NG}}{\dot{m}_{NG} + \dot{m}_{Diesel}} \cdot 100 \qquad (3.3)$$

Fig. 3.4 shows the steady state validation of ICE power and exhaust gas temperature

by varying SOI, MAP, $DIPr$ and DSR. In Chapter 3, the maximum steady state errors in the entire operating range of the ICE are less than: (i) 5% in predicting power, and (ii) 3% in predicting exhaust gas temperature. Fig. 3.4 also shows that P^{ICE} increases as MAP, $DIPr$ and DSR increases. In addition, increasing SOI shows that P^{ICE} peaks at an optimal value of SOI; but, P^{ICE} reduces as SOI is increased or decreased from this optimal value.
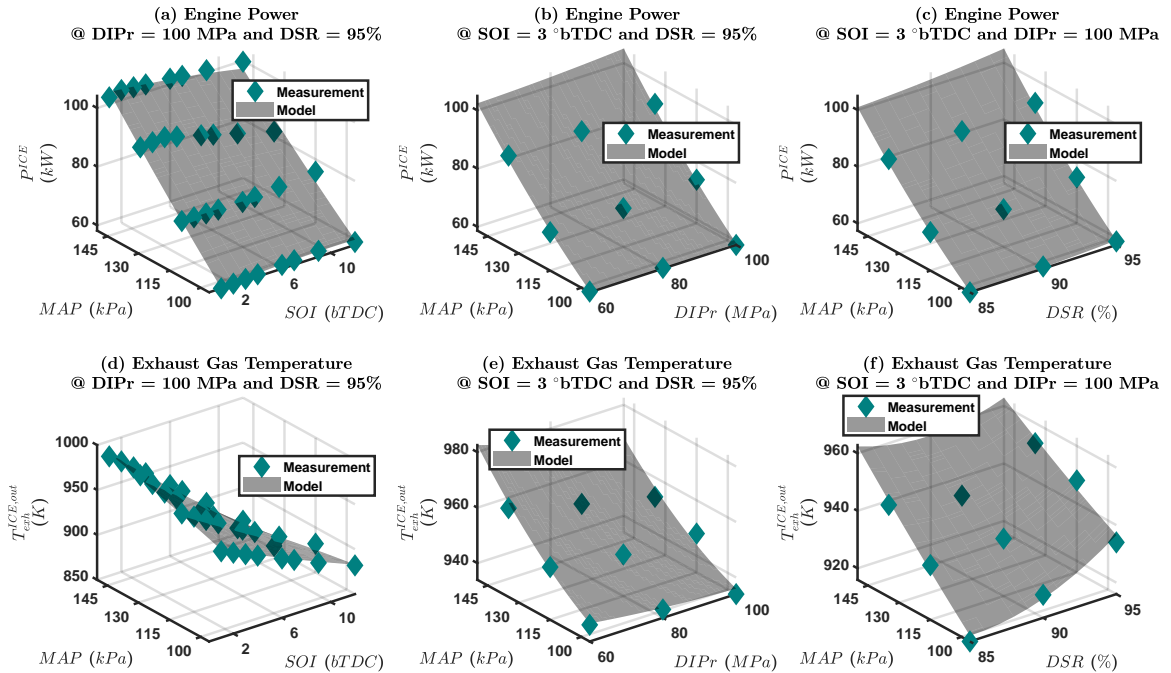
Figure 3.4: Comparison between the ICE steady state measurements and model output as a function of the manifold absolute pressure (MAP), diesel start of injection (SOI), diesel injection pressure ($DIPr$) and diesel substitution ratio (DSR). ICE speed: 1200 rpm, EGR: 0%.

Furthermore, the air path dynamics is captured in the ICE model by using 2nd order system dynamics. Fig. 3.5 shows the transient validation of MAP as a function of time. Fig. 3.5 was generated by increasing the throttle opening percentage and measuring MAP in the ICE test-cell (Fig. 3.2) and in the ICE model. The maximum

transient error of the model in predicting MAP is less than 3%.

Applying SLT to the dual fuel ICE, the rate of exergy destruction of the ICE ($\dot{X}_{Dest}^{ICE}$) is calculated as follows:

$$\dot{X}_{Dest}^{ICE} = (1 - \frac{T_{amb}}{T_{wall}^{ICE}})\dot{Q}_{HL}^{ICE} - P^{ICE} + (\sum_{in} \dot{m}_{in}\psi - \sum_{out} \dot{m}_{out}\psi) \qquad (3.4)$$

where, T_{amb} is the ambient air temperature; T_{wall}^{ICE} is the cylinder wall temperature of the ICE; $\dot{Q}_{HL}^{ICE}$ is the rate of heat lost from the ICE to the ambient air; and $\sum_{in} \dot{m}_{in}\psi$ and $\sum_{out} \dot{m}_{out}\psi$ are the rate of exergies due to the fluids flowing into and out of the ICE, respectively. For the ICE studied in Chapter 3, $\dot{Q}_{HL}^{ICE}$ is a function of T_{amb}, T_{wall}^{ICE} and MAP.
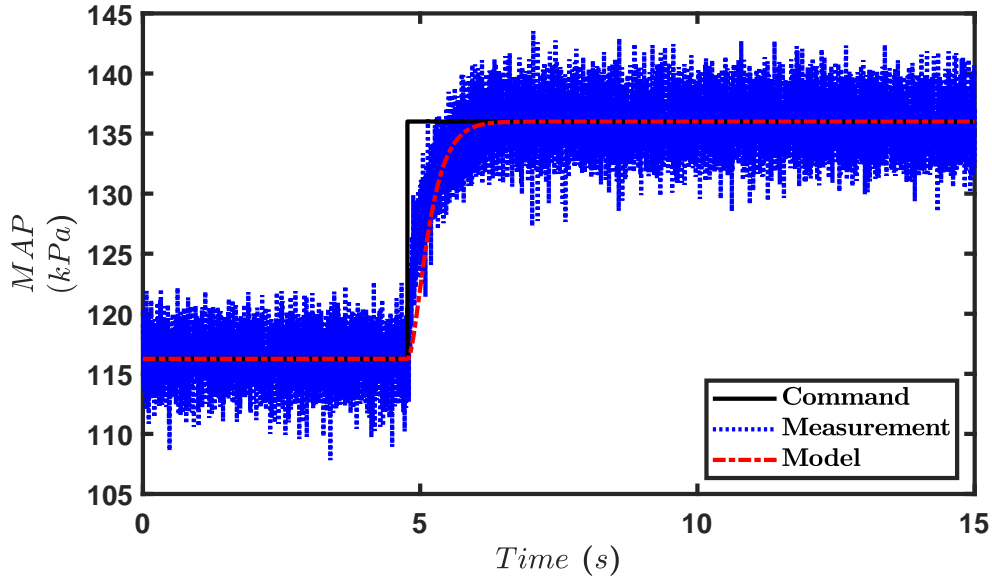
Figure 3.5: Transient comparison of manifold absolute pressure (MAP) between the ICE measurements and model output; ICE speed: 1200 rpm, SOI: 3 °bTDC, $DIPr$: 100 MPa, DSR: 95%, EGR: 0%.

Furthermore, the fluids input into the ICE include the diesel fuel, natural gas fuel, and ambient air (Figure 3.3). However the rate of exergy values of the diesel fuel and natural gas fuel is dominant when compared to rate of exergy value of ambient air. Hence, the rate exergy due to the fluids flowing into the ICE ($\sum_{in} \dot{m}_{in} \psi$) is approximated as:

$$\sum_{in} \dot{m}_{in} \psi = \dot{m}_{Diesel} \cdot HV_{Diesel} \cdot K_{Diesel} + \dot{m}_{NG} \cdot HV_{NG} \cdot K_{NG} \qquad (3.5)$$

where, HV_{Diesel} and HV_{NG} are the heating values of the diesel and natural gas fuel, respectively; and K_{Diesel} and K_{NG} are the chemical exergy factors of diesel and natural gas fuel, respectively.

The chemical exergy factor (K) of hydrocarbon fuels is calculated by [145]:

$$K = 1.0401 + 0.1728 \cdot \frac{h}{c} + 0.0432 \cdot \frac{o}{c} + 0.2169 \cdot \frac{s}{c} \cdot (1 - 2.0628 \cdot \frac{h}{c}) \qquad (3.6)$$

where, h, c, o and s are the mass fraction of hydrogen, carbon, oxygen and sulphur in the fuel, respectively.

Finally, the exit rate exergy due to exhaust gases flowing out the ICE ($\sum_{out} \dot{m}_{out} \psi$) is:

$$\sum_{out} \dot{m}_{out} \psi = \dot{m}_{exh} \cdot [(h_{exh}^{ICE,out} - h_{amb}) + T_{amb} \cdot (s_{exh}^{ICE,out} - s_{amb})] \qquad (3.7)$$

101

where, $\dot{m}_{exh}$ is the mass flow rate of the engine exhaust gas; $h_{exh}^{ICE,out}$ and $s_{exh}^{ICE,out}$ are the specific enthalpy and specific entropy of the exhaust gases leaving the ICE, respectively; and h_{amb} and s_{amb} are the specific enthalpy and specific entropy of the ambient air, respectively.

3.3.2 Turbocharger (TC)

The turbocharger is modeled separately as a (i) turbo-expander, and (ii) compressor. The temperature of the intake air at the outlet of the compressor ($T_{int}^{c,out}$) is calculated by:

$$T_{int}^{c,out} = ((\frac{p_{amb}}{MAP})^{1-\gamma^c} \cdot T_{amb}^{\gamma^c})^{\frac{1}{\gamma^c}} \tag{3.8}$$

where, p_{amb} and T_{amb} are the ambient air pressure and temperature, respectively; and γ^c is the compression ratio of the compressor. γ^c is estimated using the measurements from the engine test cell (Fig. 3.2).

Then, the pressure of the exhaust gas at the outlet of the turbo-expander ($p_{exh}^{tb,out}$) is determined by:

$$p_{exh}^{tb,out} = ((\frac{T_{exh}^{tb,out}}{T_{exh}^{tb,in}})^{\gamma^{tb}} \cdot (p_{exh}^{tb,in})^{1-\gamma^{tb}})^{\frac{1}{1-\gamma^{tb}}} \tag{3.9}$$

where, $T_{exh}^{tb,out}$ is the temperature of the engine exhaust fluid leaving the turbo-expander; $p_{exh}^{tb,in}$ and $T_{exh}^{tb,in}$ are the pressure and temperature of the engine exhaust

fluid entering the turbo-expander, respectively; and γ^{tb} is the expansion ratio of the turbo-expander. $T_{exh}^{tb,out}$, $p_{exh}^{tb,in}$, $T_{exh}^{tb,in}$, and γ^{tb} are estimated using the measurements from the engine test cell (Fig. 3.2).

Then by applying FLT, power of the compressor (P^c) and power of the turbo-expander (P^{tb}) are calculated as:

$$P^c = \dot{m}_{int} \cdot (h_{int}^{c,out} - h_{int}^{c,in}) \tag{3.10a}$$

$$P^{tb} = \dot{m}_{exh} \cdot (h_{exh}^{tb,in} - h_{exh}^{tb,out}) \tag{3.10b}$$

where, $\dot{m}_{int}$ is the rate of mass flow of the engine intake fluid; $h_{int}^{c,in}$ and $h_{int}^{c,out}$ are the specific enthalpies of the engine intake fluid entering and leaving the compressor, respectively; $\dot{m}_{exh}$ is the mass flow rate of the engine exhaust gas; and $h_{exh}^{tb,in}$ and $h_{exh}^{tb,out}$ are the specific enthalpies of the engine exhaust fluid entering and leaving the turbo-expander, respectively.

Applying SLT, the rate of exergy destruction in the compressor ($\dot{X}_{Dest}^c$) and the rate of exergy destruction in the turbo-expander ($\dot{X}_{Dest}^{tb}$) are calculated as:

$$\dot{X}_{Dest}^c = T_{amb} \cdot \dot{m}_{int} \cdot (s_{int}^{c,out} - s_{int}^{c,in}) \tag{3.11a}$$

$$\dot{X}_{Dest}^{tb} = T_{amb} \cdot \dot{m}_{exh} \cdot (s_{exh}^{tb,out} - s_{exh}^{tb,in}) \tag{3.11b}$$

where, $s_{int}^{c,in}$ and $s_{int}^{c,out}$ are the specific entropies of the engine intake fluid entering and

103

leaving the compressor, respectively; and $s_{exh}^{tb,in}$ and $s_{exh}^{tb,out}$ are the specific entropies of the engine exhaust fluid entering and leaving the turbo-expander, respectively.

It should be noted that knowing the pressure and temperature of the fluid, the specific enthalpies and specific entropies of the fluid are obtained from EES, a commercially available software [146].

3.3.3 Heat Exchanger (HE)

As shown in Fig. 3.3, an HE is used in this study to transfer thermal energy from the ICE exhaust gas to the ORC. Equation (3.12) is used to calculate the temperature of the engine exhaust gas leaving the WHR system ($T_{exh}^{WHR,out}$).

$$T_{exh}^{WHR,out} = T_{exh}^{WHR,in} - \frac{\dot{Q}_{ORC}}{U_{HE} \cdot A_{s_{HE}}} \tag{3.12}$$

Where, $T_{exh}^{WHR,in}$ is the temperature of the engine exhaust gas entering the WHR; $\dot{Q}_{ORC}$ is the rate of heat transferred from the HE to the ORC; U_{HE} (=45 W/m².K) is the overall heat transfer co-efficient of the HE; and $A_{s_{HE}}$ is the surface area of the HE.

For the HE in this study, U_{HE} and $A_{s_{HE}}$ are constant and the temperature drop of

104

the exhaust gas across the WHR (i.e., $\Delta T_{exh}^{WHR} = T_{exh}^{WHR,out} - T_{exh}^{WHR,in}$) is a function

of the heat flow rate to the ORC.

$$\Delta T_{exh}^{WHR} = \Psi(\dot{Q}_{ORC}) \tag{3.13}$$

Applying SLT, the rate of exergy destruction in the HE ($\dot{X}_{Dest}^{HE}$) is:

$$\dot{X}_{Dest}^{HE} = T_{amb} \cdot \dot{m}_{exh} \cdot (s_{exh}^{WHR,out} - s_{exh}^{WHR,in}) \tag{3.14}$$

where, $s_{exh}^{WHR,in}$ and $s_{exh}^{WHR,out}$ are the specific entropies of the exhaust gas entering

and leaving the HE, respectively.

3.3.4 Organic Rankine Cycle (ORC)

Applying the FLT for the ORC yields:

$$P^{ORC} = P^e - P^{pu} \tag{3.15a}$$

$$P^e = \eta_{isen}^e \cdot \eta_{mech}^e \cdot \dot{m}_{WF} \cdot (h_{WF}^{e,in} - h_{WF}^{e,out}) \tag{3.15b}$$

$$P^{pu} = \frac{\dot{m}_{WF} \cdot (h_{WF}^{pu,out} - h_{WF}^{pu,in})}{\eta_{isen}^{pu} \cdot \eta_{mech}^{pu}} \tag{3.15c}$$

$$\dot{Q}_{ORC} = \dot{m}_{WF} \cdot (h_{WF}^{e,in} - h_{WF}^{pu,out}) \tag{3.15d}$$

where, P^{ORC} is the net mechanical power delivered by the ORC; P^e is the mechanical power of the expander in the ORC; P^{pu} is the mechanical power input to the pump in the ORC; η_{isen}^e and η_{mech}^e are the isentropic and mechanical efficiencies of the expander in the ORC, respectively; $\dot{m}_{WF}$ is the mass flow rate of the WF in the ORC; $h_{WF}^{e,in}$ and $h_{WF}^{e,out}$ are the specific enthalpies of the WF entering and leaving the expander in the ORC, respectively; η_{isen}^{pu} and η_{mech}^{pu} are the isentropic and mechanical efficiencies of the pump in the ORC, respectively; and $h_{WF}^{pu,in}$ and $h_{WF}^{pu,out}$ are the specific enthalpies of the WF entering and leaving the pump in the ORC, respectively. Further, it can be shown that:

$$Tq^{ORC} = \Pi_1(\dot{m}_{WF}, r_p) \tag{3.16a}$$

$$P^{ORC} = \Pi_2(\dot{m}_{WF}, r_p) \tag{3.16b}$$

where, Tq^{ORC} is the net mechanical produced by the ORC; and r_p is the pressure ratio of the ORC.

By applying SLT to the ORC system in this study, the rate of exergy destruction of the ORC ($\dot{X}_{Dest}^{ORC}$) is given by:

$$\dot{X}_{Dest}^{ORC} = T_{amb} \cdot \left(\frac{\dot{Q}_{Lost}}{T_{con,m}} - \frac{\dot{Q}_{ORC}}{T_{ev,m}} \right) \tag{3.17}$$

where, $\dot{Q}_{Lost}$ is the rate of heat transferred from the condersor of the ORC to the

ambient; $T_{ev,m}$ and $T_{con,m}$ are the arithmetic mean temperatures of the evaporator and condenser of the ORC, respectively.

For the ORC module in this study, we can show that the rate of exergy recovered $(\dot{X}_{Rec}^{ORC})$ is

$$\dot{X}_{Rec}^{ORC} = \lambda_2(\dot{m}_{WF}, r_p) \tag{3.18}$$

Finally, the ORC model is validated against the measurements in references [143, 144] and the maximum steady state errors are less than 3%.

3.4 Energy Based Model Predictive Control (EMPC) for Automotive Applications - Framework Design, Results and Analysis

3.4.1 Structure of the designed Energy Based Model Predictive Controller (EMPC)

The brake thermal efficiency of the combined ICE and WHR system is calculated as:

$$\eta_{th,b}^{System} = \frac{Tq^{System} \cdot \omega}{\dot{m}_{Diesel} \cdot HV_{Diesel} + \dot{m}_{NG} \cdot HV_{NG}} \tag{3.19}$$

where, Tq^{System} is the total torque of the system; ω is the angular speed of the system; and HV_{Diesel} and HV_{NG} are the heating values of diesel fuel and natural gas fuel, respectively. Additionally, the total system torque (Tq^{System}) is the sum of both the ICE torque (Tq^{Engine}) and the ORC torque (Tq^{ORC}).

Fig. 3.6 shows the structure of the EMPC framework designed to (a) minimize the ICE fuel consumption; and (b) meet the exhaust gas temperature constraint of the ICE when integrated with a WHR system. The objective function in Equation (3.20)
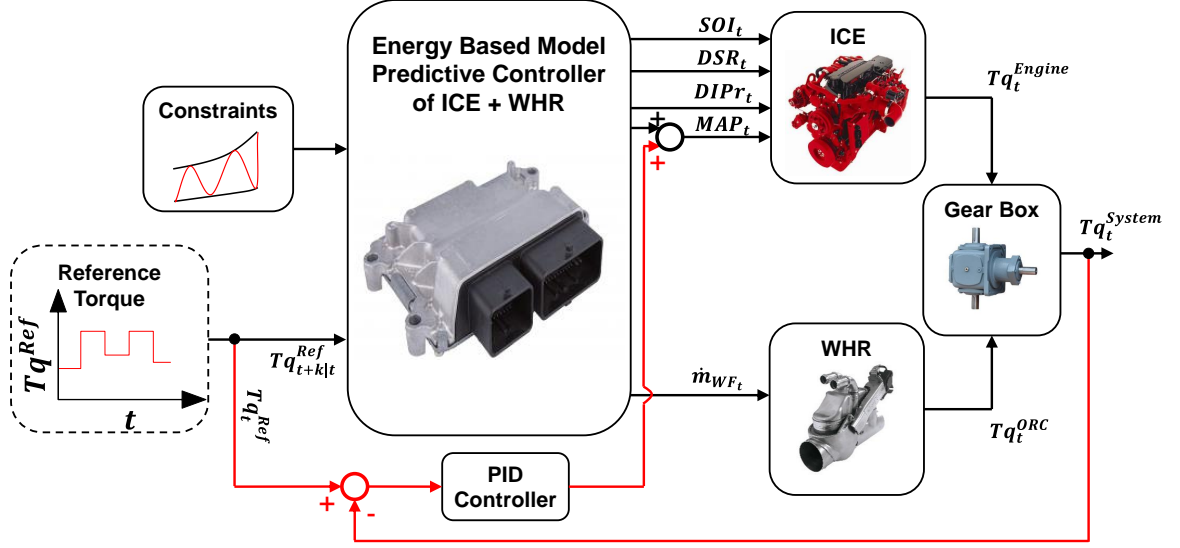
Figure 3.6: Structure of the designed EMPC for the combined ICE and WHR system. © 2021 IEEE

is formulated to maximize the efficiency of the system. The system is subject to the constraints listed in Equations (3.21a) through (3.21q). The optimization problem is solved at each time step, to find the current and future values of diesel injection pressure ($DIPr$), diesel substitution ratio (DSR), diesel start of injection (SOI), manifold absolute pressure (MAP), and mass flow rate of the WF ($\dot{m}_{WF}$) in the ORC. The input for the EMPC optimization model is the required torque (Tq^{Ref}).

$$\max_{MAP,SOI,DIPr,DSR,\dot{m}_{WF}} \left\{ \eta_{th,b}^{System} \right\} \tag{3.20}$$

Subject to the following constraints:

$$\eta_{th,b_{t+k|t}}^{System} = \Lambda(MAP_{t+k|t}, SOI_{t+k|t}, DIPr_{t+k|t}, DSR_{t+k|t}, \dot{m}_{WF_{t+k|t}}) \tag{3.21a}$$

$$Tq_{t+k|t}^{Engine} = \Upsilon(MAP_{t+k|t}, SOI_{t+k|t}, DIPr_{t+k|t}, DSR_{t+k|t}) \tag{3.21b}$$

$$Tq_{t+k|t}^{ORC} = \Pi(\dot{m}_{WF_{t+k|t}}) \tag{3.21c}$$

$$Tq_{t+k|t}^{Ref} = Tq_{t+k|t}^{Engine} + Tq_{t+k|t}^{ORC} \tag{3.21d}$$

$$\underline{x_i} \leq x_{i_{t+k|t}} \leq \overline{x_i} \tag{3.21e}$$

$$-\widehat{x_i} \leq \frac{d(x_{i_{t+k|t}})}{dt} \leq +\widehat{x_i} \tag{3.21f}$$

$$\underline{T_{exh_{t+k|t}}} \leq \Omega(MAP_{t+k|t}, SOI_{t+k|t},$$
$$DIPr_{t+k|t}, DSR_{t+k|t}, \dot{m}_{WF_{t+k|t}}) \leq \overline{T_{exh_{t+k|t}}} \tag{3.21g}$$

$$\underline{\omega} \leq \omega_{t+k|t} \leq \overline{\omega} \tag{3.21h}$$

$$\underline{Tq^{Engine}} \leq Tq_{t+k|t}^{Engine} \leq \overline{Tq^{Engine}} \tag{3.21i}$$

$$\underline{Tq^{ORC}} \leq Tq_{t+k|t}^{ORC} \leq \overline{Tq^{ORC}} \tag{3.21j}$$

Equation (3.21a) constitutes the brake thermal efficiency of the system; (3.21b) and (3.21c) constitute the torque of the ICE and ORC, respectively; (3.21d) is the constraint to keep the system output torque equal to the reference (required) torque; (3.21e) limits the control variables (represented by x_i) between their minimum and maximum values; (3.21f) represents the ramp limits of all the control variables; (3.21g) limits the temperature of the exhaust gas after the WHR system within the lower

and higher exhaust gas temperature bounds to satisfy the thermal requirements of the exhaust aftertreatment system; (3.21h) limits the angular speed of the system; (3.21i) and (3.21j) limit the ICE and ORC torques, respectively. In addition, Fig. 3.6 shows that a PID controller is designed in parallel to the designed EMPC. EMPC provides the optimum trajectory for the engine control inputs (SOI, DSR, $DIPr$, MAP) and WHR control input ($\dot{m}_{WF}$). The EMPC mainly acts as a feedforward optimal controller. Then, the PID controller is added as a feedback controller for Tq^{Ref} tracking. The PID controller adjusts MAP because it is the dominant variable affecting the total system torque (Tq^{System}).

3.4.2   Control Results

The plant models and desired controllers are implemented in MATLAB®. The system synchronous speed was fixed at 1200 rpm and simulations were done for 80 seconds. For EMPC formulation, YALMIP Toolbox [107] is used for a symbolic interface with MATLAB® solvers. The control horizon of 100 ms (1 engine cycle) is applied, prediction horizon of 1 second (10 Engine cycles) is applied, and the FMINCON solver is utilized. The simulation time to real time ratio is 2.1 when solving the optimization problem was run in a computer with Intel® Core™ i7-8700K CPU @ 3.7 GHz with 32 GB of RAM. Further reduction in the computation cost is needed for the designed EMPC to run on the engine control module (ECM).

3.4.2.1 Rule Based Control (RBC)

An RBC framework is designed to provide a baseline for comparison against the designed EMPC framework. The RBC derives its rules from a "fully calibrated" engine operation done by the engine test cell calibration engineer, taking about one year to calibrate.

3.4.2.2 Fuel Saving

In this section, the fuel saving potential of the designed control framework is discussed. Here, the controller performance is evaluated by demanding the same reference torque (Tq^{Ref}) and comparing the outputs from three controllers including (i) the designed EMPC framework when applied to the combined ICE and WHR system, (ii) the RBC when applied to the ICE system without WHR, and (iii) the RBC when applied to the combined ICE and WHR system. Fig. 3.7 shows the tracking performance of all the three controllers. This figure shows that the tracking of Tq^{Ref} is similar in all controllers; thus, their performance for saving fuel and meeting constraints can be compared.

Fig. 3.8 shows a comparison of all the control outputs among the three designed control systems. In RBC, the values for $\dot{m}_{WF}$, $DIPr$, DSR, and SOI are based on
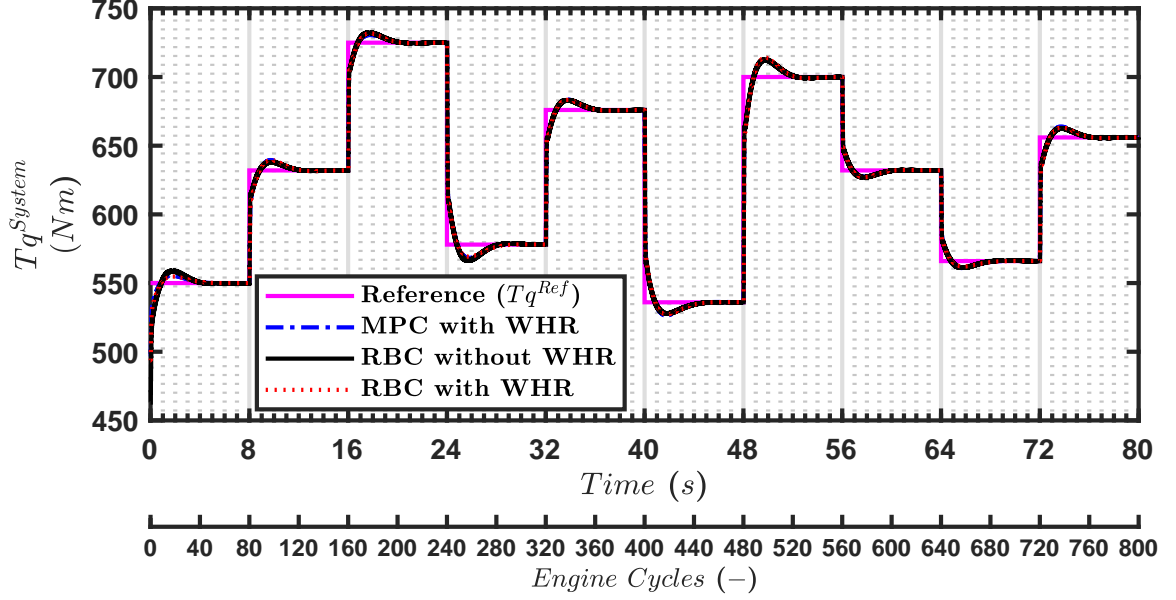
Figure 3.7: Tracking performance of the three designed controllers. The torque tracking error of all controllers is similar and the maximum tracking error is less than 2%. ICE speed $= 1200\ rpm$, and EGR $= 0\%$. © 2021 IEEE

test cell calibration for the required steady-state torque; while the value of MAP is interpolated in accordance to the required ICE torque (Tq^{Engine}). The designed EMPC optimally chooses the values of the engine and WHR control variables to (a) minimize the fuel consumption; and (b) meet exhaust gas temperature constraint as shown in Fig. 3.9.

Fig. 3.9(a) shows a reduction in fuel consumption of the ICE as a result of two factors: (i) adding WHR, (ii) changing RBC to EMPC. The fuel consumed by the ICE over the simulation time for the three control systems is shown in Table 3.3. This is calculated by integrating the fuel consumption rate of the ICE (Fig. 3.9(a)) over the simulation time. Fig. 3.9(b) shows that the designed EMPC is also able to
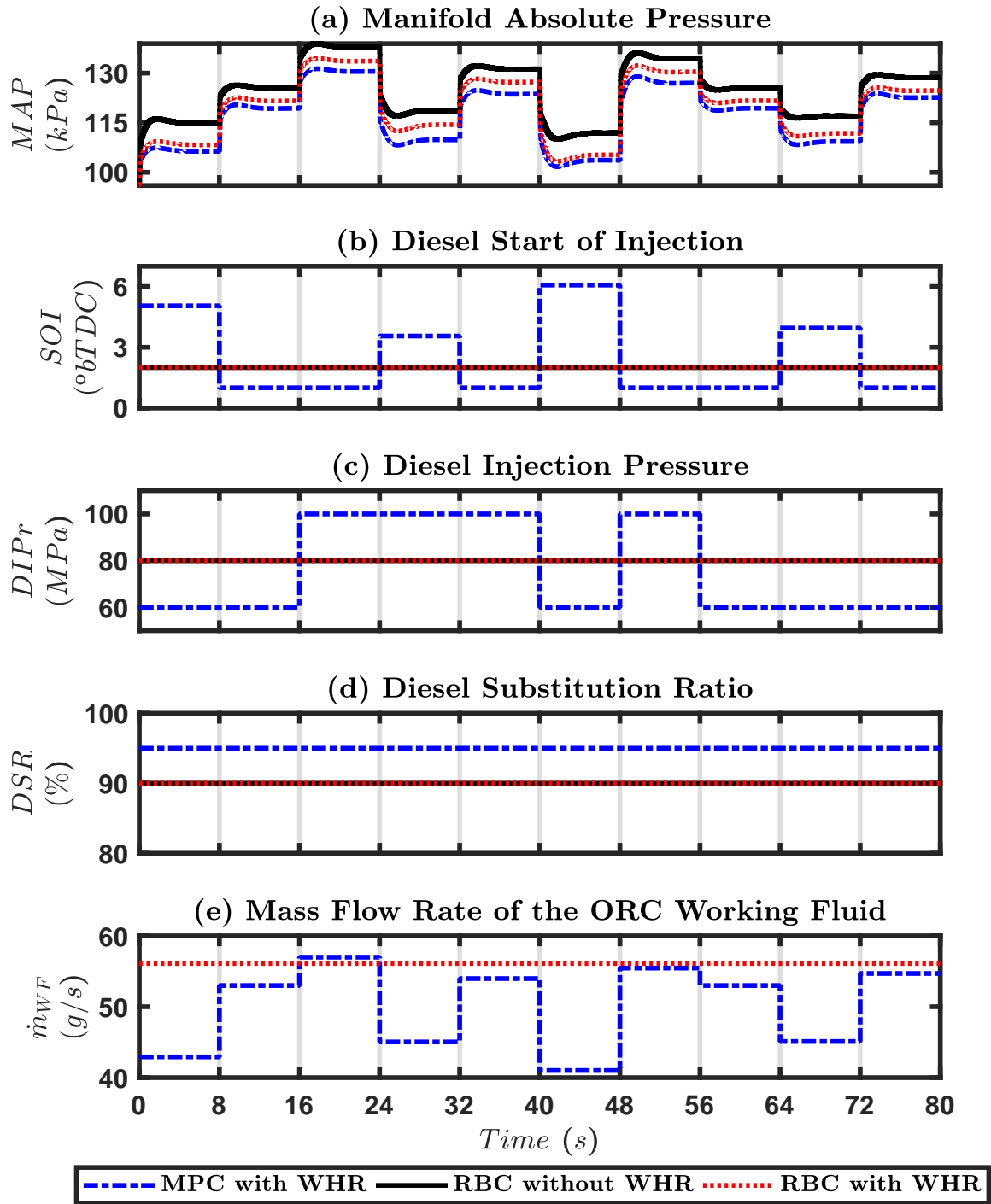
Figure 3.8: Controller outputs when the designed EMPC is applied to the combined ICE and WHR system. The controller outputs are compared with the two RBCs for the same conditions as those in Fig. 3.7. © 2021 IEEE

meet the exhaust gas temperature constraint and controls $T_{exh}^{WHR,out}$ such that it is always above the minimum required limit. The exhaust gas temperature constraint is determined by adding 25 K to the catalyst light off temperature (i.e., 500 K) for a typical diesel ICE [147]. The failure of the exhaust gas temperature to meet the exhaust temperature constraint when RBC is applied to the combined ICE and WHR system is quantified in Table 3.3. Fig. 3.9(b) shows that $T_{exh}^{WHR,out}$ violates the minimum allowed temperature at least 40% of the times.
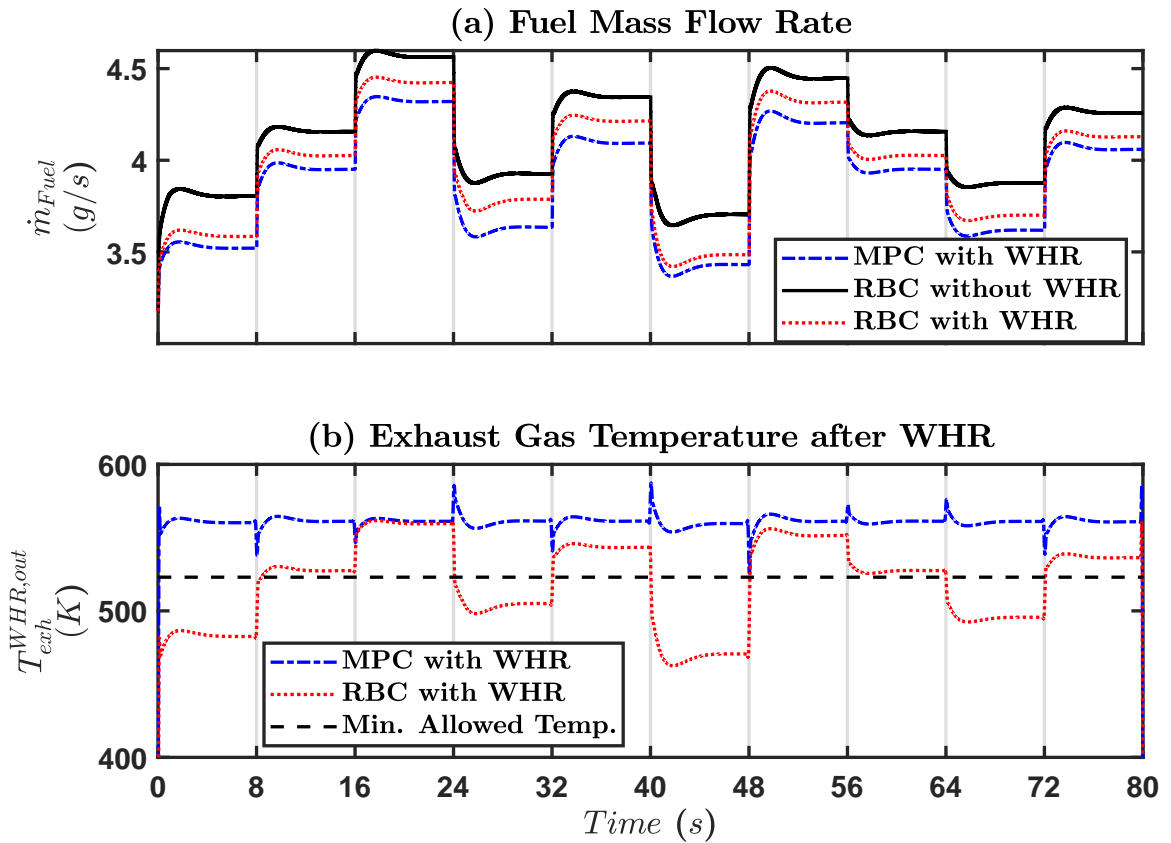
Figure 3.9: Comparison of the system outputs for the same conditions as those in Fig. 3.7. © 2021 IEEE

3.4.2.3 Variable Exhaust Gas Temperature Constraint

The controller will encounter situations dictated by exhaust aftertreatment system conditions. The controller should be capable of (i) maintaining the exhaust gas temperature at the inlet of the exhaust aftertreatment system to be greater than the required catalyst light off temperature, and (ii) raising the exhaust gas temperature at the inlet of the aftertreatment system high enough for efficient diesel particulate filter (DPF) regeneration whenever needed. In tune with that, variable exhaust gas temperature constraint is considered in the designed EMPC. To illustrate the controller performance for a case study, Fig. 3.9(b) is changed to a variable exhaust gas temperature constraint by considering the DPF regeneration temperature for a typical diesel ICE [148] from time 36 to 44 seconds. In addition, the same reference torque (Tq^{Ref}) as shown in Fig. 3.7 is used. Fig. 3.10 shows the results of the designed

Table 3.3

Fuel consumption and the average violation of exhaust gas temperature from the minimum allowed exhaust gas temperature are compared among the three system and control configurations studied. © 2021 IEEE

System	Control	Fuel Consumed (g)	Fuel Savings* (%)	Average Exh. Temp. Violation (K)**
ICE	RBC	329.9	-	-
ICE + WHR	RBC	317.5	3.8	14
ICE + WHR	EMPC	310.3	5.9	0

* Percentages are calculated by comparing with the baseline RBC without WHR.
** The average exhaust gas temperature violation is defined as a metric to account for the violation of engine exhaust gas temperature after the WHR system ($T_{exh}^{WHR,out}$) against the required exhaust temperature bound ($\underline{T_{exh}}$) and is given by $\dfrac{\sum\limits_{i=1}^{i=n} (\underline{T_{exh}} - T_{exh}^{WHR,out}(i))}{n}$, when $T_{exh}^{WHR,out}(i) < \underline{T_{exh}}$
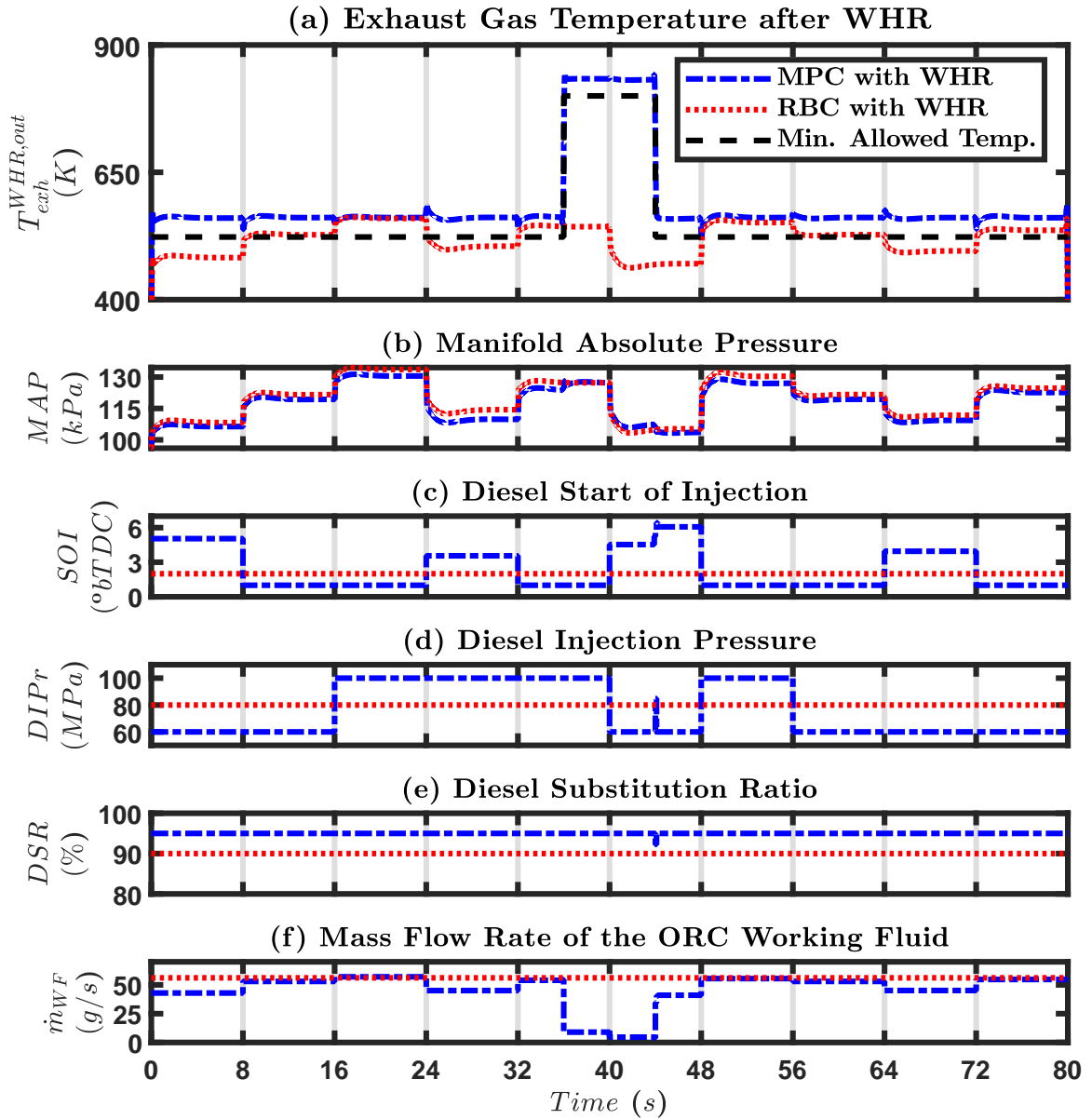
Figure 3.10: System and controller outputs when the designed EMPC and RBC are applied to the combined ICE and WHR system. Subplots (b) through (f) show the controller outputs. © 2021 IEEE

controllers in meeting $T_{exh}^{WHR,out}$ constraint. The designed EMPC optimally adjusts

the control outputs such that the constraints are never violated; but, the RBC is

not capable of meeting the exhaust temperature constraint during DPF regeneration

(Fig. 3.10).

3.4.3   Summary and Conclusions

Section 3.4 presented the study undertaken to design an energy based model predictive controller (EMPC) to (i) minimize the fuel consumption, and (ii) meet time-varying exhaust gas temperature constraint for a combined ICE and WHR system in vehicles. The exhaust gas temperature constraint represents light-off temperature requirements of the exhaust aftertreatment systems and also the required temperature for efficient DPF regeneration. In this study, control-oriented models for ICE system and WHR system were developed and then incorporated into an EMPC framework to optimally control the ICE and WHR systems in accordance with the reference torque demand. The main findings from this study show that the designed EMPC framework:

† can provide upto 5.9% fuel saving, compared to the baseline experimentally calibrated controller (RBC) for the ICE system without WHR;

† improves the fuel saving by 2.1%, compared to the RBC for the combined ICE and WHR system; and

† meets both constant and time-varying exhaust gas temperature (T_{exh}) constraints without any violations, while the RBC failed to meet T_{exh} constraints in over 40% of the tested conditions.

3.5 Energy Based Model Predictive Control (EMPC) for Electric Power in Buildings - Framework Design, Results and Analysis

3.5.1 Structure of the Designed Energy Based Model Predictive Control (EMPC)

The system efficiency of the combined ICE and WHR system (η^{System}) is calculated as:

$$\eta^{System} = \frac{P^{System}}{\dot{m}_{Diesel} \cdot HV_{Diesel} + \dot{m}_{NG} \cdot HV_{NG}} \tag{3.22}$$

where, P^{System} is the total electrical power delivered by the combined ICE and WHR system; HV_{Diesel} and HV_{NG} are the heating values of diesel and natural gas, respectively. P^{System} is calculated as the sum of P^{ICE} and P^{ORC}; multiplied by the gear box efficiency (η_{GB}) and the generator efficiency (η_{Gen}) as shown:

$$P^{System} = \eta_{GB} \cdot \eta_{Gen} \cdot (P^{ICE} + P^{ORC}) \tag{3.23}$$

Fig. 3.11 shows the structure of the EMPC framework designed to (a) minimize the

ICE fuel consumption; and (b) enforce the exhaust gas temperature constraint of the ICE when integrated with a WHR system. The objective function in Equation (3.24) is formulated to maximize efficiency of the system. The system is subject to the constraints listed in Equations (3.25a) through (3.25q). The optimization problem is solved at each time step, to find the current and future values of diesel injection pressure ($DIPr$), diesel substitution ratio (DSR), diesel start of injection (SOI), manifold absolute pressure (MAP), and mass flow rate of the WF ($\dot{m}_{WF}$) in the ORC. The input for the EMPC optimization model is the required power (P^{Ref}).
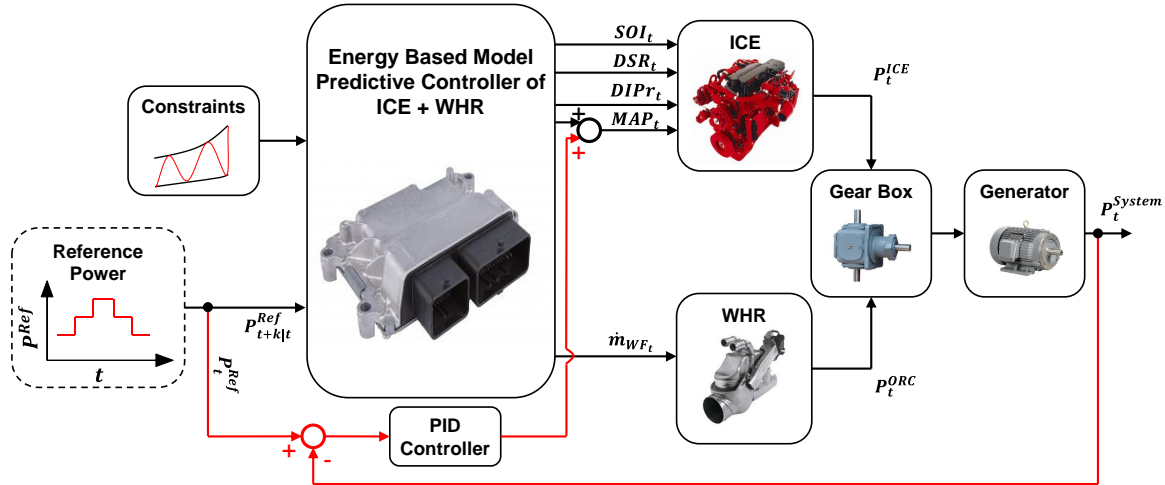
Figure 3.11: Structure of the designed EMPC for the combined ICE and WHR system.

The objective function is:

$$\max_{MAP,SOI,DIPr,DSR,\dot{m}_{WF}} \left\{ \eta^{System} \right\} \tag{3.24}$$

120

Subject to the following constraints:

$$\eta_{t+k|t}^{System} = \Lambda(MAP_{t+k|t}, SOI_{t+k|t}, DIPr_{t+k|t}, DSR_{t+k|t}, \dot{m}_{WF_{t+k|t}}) \quad \text{(3.25a)}$$

$$P_{t+k|t}^{ICE} = \Upsilon(MAP_{t+k|t}, SOI_{t+k|t}, DIPr_{t+k|t}, DSR_{t+k|t}) \quad \text{(3.25b)}$$

$$P_{t+k|t}^{ORC} = \Pi(\dot{m}_{WF_{t+k|t}}) \quad \text{(3.25c)}$$

$$P_{t+k|t}^{Ref} = (P_{t+k|t}^{ICE} + P_{t+k|t}^{ORC}) \quad \text{(3.25d)}$$

$$\underline{MAP} \leq MAP_{t+k|t} \leq \overline{MAP} \quad \text{(3.25e)}$$

$$\alpha(MAP_{t+k|t}) \leq SOI_{t+k|t} \leq \beta(MAP_{t+k|t}) \quad \text{(3.25f)}$$

$$\underline{DIPr} \leq DIPr_{t+k|t} \leq \overline{DIPr} \quad \text{(3.25g)}$$

$$\underline{DSR} \leq DSR_{t+k|t} \leq \overline{DSR} \quad \text{(3.25h)}$$

$$\underline{\dot{m}_{WF}} \leq \dot{m}_{WF_{t+k|t}} \leq \overline{\dot{m}_{WF}} \quad \text{(3.25i)}$$

$$-\widehat{MAP} \leq \frac{d(MAP_{t+k|t})}{dt} \leq +\widehat{MAP} \quad \text{(3.25j)}$$

$$-\widehat{SOI} \leq \frac{d(SOI_{t+k|t})}{dt} \leq +\widehat{SOI} \quad \text{(3.25k)}$$

$$-\widehat{DIPr} \leq \frac{d(DIPr_{t+k|t})}{dt} \leq +\widehat{DIPr} \quad \text{(3.25l)}$$

$$-\widehat{DSR} \leq \frac{d(DSR_{t+k|t})}{dt} \leq +\widehat{DSR} \quad \text{(3.25m)}$$

$$-\widehat{\dot{m}_{WF}} \leq \frac{d(\dot{m}_{WF_{t+k|t}})}{dt} \leq +\widehat{\dot{m}_{WF}} \quad \text{(3.25n)}$$

$$\underline{T_{exh_{t+k|t}}} \leq \Omega(MAP_{t+k|t}, SOI_{t+k|t}, DIPr_{t+k|t},$$

$$DSR_{t+k|t}, \dot{m}_{WF_{t+k|t}}) \leq \overline{T_{exh_{t+k|t}}} \quad \text{(3.25o)}$$

$$\underline{P^{Engine}} \leq P_{t+k|t}^{Engine} \leq \overline{P^{Engine}} \quad \text{(3.25p)}$$

$$\underline{P^{ORC}} \leq P_{t+k|t}^{ORC} \leq \overline{P^{ORC}} \quad \text{(3.25q)}$$

$$\text{(3.25r)}$$

Equation (3.25a) constitutes the system efficiency; (3.25b) and (3.25c) constitute the torque of the ICE and ORC, respectively; (3.25d) is the constraint to keep the system output torque equal to the reference (required) torque; (3.25e) through (3.25i) limit all the control variables within the minimum and maximum allowable values; (3.25j) through (3.25n) represent the ramp limits of all the control variables; (3.25o) limits the temperature of the exhaust gas after the WHR system within the lower and higher exhaust gas temperature bounds; (3.25p) and (3.25q) limit the ICE and ORC torques, respectively. In addition, Fig. 3.11 shows that a PID controller is designed in parallel to the designed EMPC. EMPC provides the optimum trajectory for the engine control inputs (SOI, DSR, $DIPr$, MAP) and WHR control input ($\dot{m}_{WF}$). The EMPC mainly acts as a feedforward optimal controller. Then, the PID controller is added as a feedback controller for P^{Ref} tracking. The PID controller adjusts MAP because it is the dominant variable affecting total system power (P^{System}).

3.5.2 Control Results

The plant models and desired controllers are implemented in MATLAB®. The system synchronous speed was fixed at 1200 rpm and simulations were done for 3-hour power demand. For EMPC formulation, YALMIP Toolbox [107] is used for a symbolic interface with MATLAB® solvers. The prediction horizon of 100 seconds is

applied, and the FMINCON solver is utilized. The optimization problem was run in a computer with Intel® Core™ i7-8700K CPU @ 3.7GHz with 32GB of RAM and the computation time was 210 seconds to simulate 3-hour operation.

3.5.2.1 Rule Based Control (RBC)

An RBC framework is designed to provide a baseline for comparison against the designed EMPC framework. The control flow of the designed RBC is shown in Fig. 3.12. The RBC represents a fully calibrated engine operation done by the engine test cell calibration engineer. Fig. 3.12 shows that the power from the ICE (P^{ICE}) is calculated as the difference of the power from ORC (P^{ORC}) and the total requested reference power (P^{Ref}). But, P^{ORC} is proportional to the mass flow rate of the WF to the ORC ($\dot{m}_{WF}$). In addition, $\dot{m}_{WF}$ is set to 0 if the system does not have a WHR system or if the system is integrated with a WHR system but if DPF regeneration event is requested by the electronic control unit (ECU). If and only if the system is integrated with WHR system and the ECU does not request a DPF regeneration event, then $\dot{m}_{WF}$ is set to a nominal value to maximise the efficiency of the ORC. For a given ICE speed and P^{ICE}; SOI, $DIPr$, and DSR are set to nominal values from the calibration tables populated from the ICE test bench data. Finally, for a given P^{ICE}, SOI, $DIPr$, and DSR; MAP is obtained using a 1-D table. It should be noted that, measurements from at least 3000 operating points were recorded to

123

populate the ICE calibration tables.
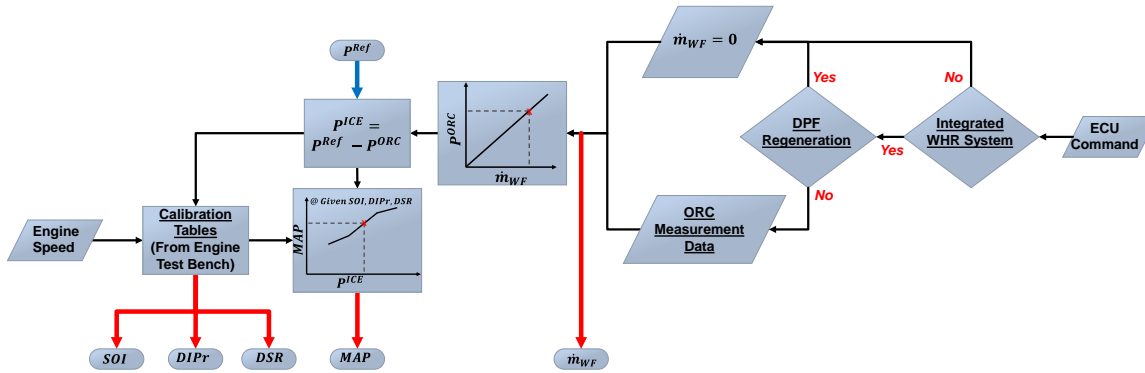
Figure 3.12: Control flow of the baseline rule based controller. The calibration tables are populated with measurements from a fully calibrated engine.
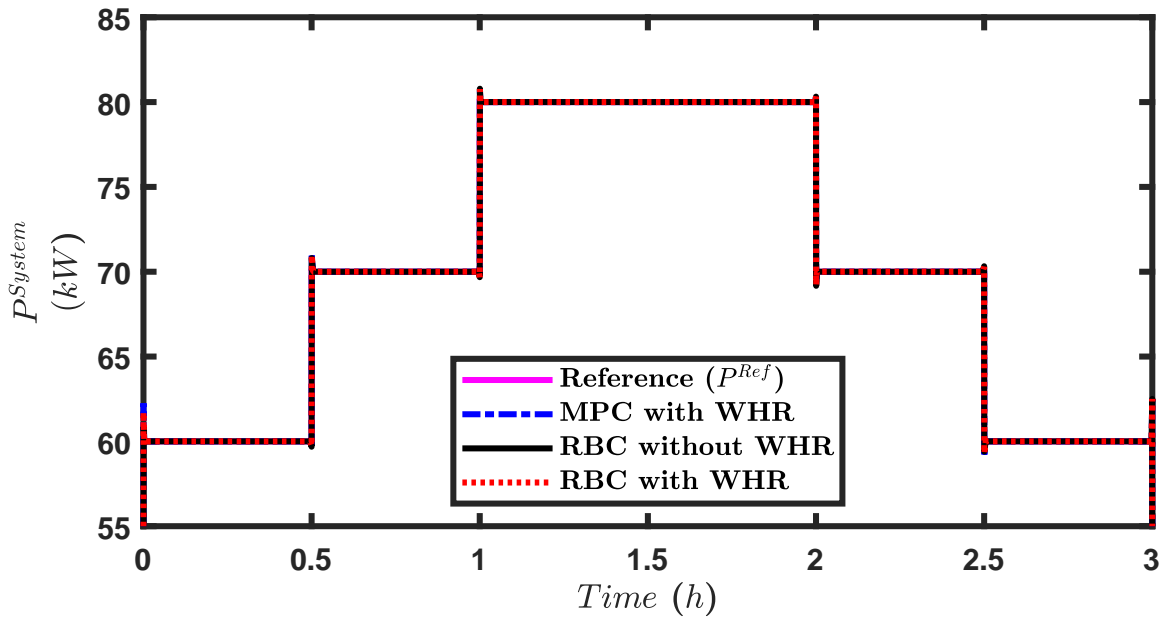
Figure 3.13: Tracking performance of the three designed controllers. The power tracking error of all controllers is similar and the maximum tracking error is less than 3%. ICE speed = 1200 rpm, and EGR = 0%.

124

3.5.2.2 Fuel Saving

In this section, the fuel saving potential of the designed control framework is discussed. Here, the controller performance is evaluated by demanding the same reference power (P^{Ref}) and comparing the outputs from three controllers including (i) the designed EMPC framework when applied to the combined ICE and WHR system, (ii) the RBC when applied to the ICE system without WHR, and (iii) the RBC when applied to the combined ICE and WHR system. Fig. 3.13 shows the tracking performance of all the three controllers to meet requested power. P^{Ref} shows a typical generator profile in the building under study [16]. This figure shows that the tracking of P^{Ref} is similar in all controllers; thus, their performance for saving fuel and meeting constraints can be compared.

Fig. 3.14 shows a comparison of all the control outputs among the three designed control systems. In RBC, the values for $\dot{m}_{WF}$, $DIPr$, DSR, and SOI are based on test cell calibration for the required steady-state power (Fig. 3.12); while the value

Table 3.4

Fuel consumption comparison among the three system and control configurations studied for the case of (i) <u>constant</u> exhaust temperature constraint, and (ii) RBC defined to maximize energy efficiency.

System	Control	Fuel Consumed (kg)	Fuel Saving* (%)
ICE	RBC	44.8	-
ICE + WHR	RBC	42.9	4.2
ICE + WHR	EMPC	41.8	6.7

* Percentages are calculated by comparing with the baseline RBC without WHR.

(a) Manifold Absolute Pressure

(b) Diesel Start of Injection

(c) Diesel Injection Pressure

(d) Diesel Substitution Ratio

(e) Mass Flow Rate of the ORC Working Fluid

MPC with WHR ——— RBC without WHR ·········· RBC with WHR
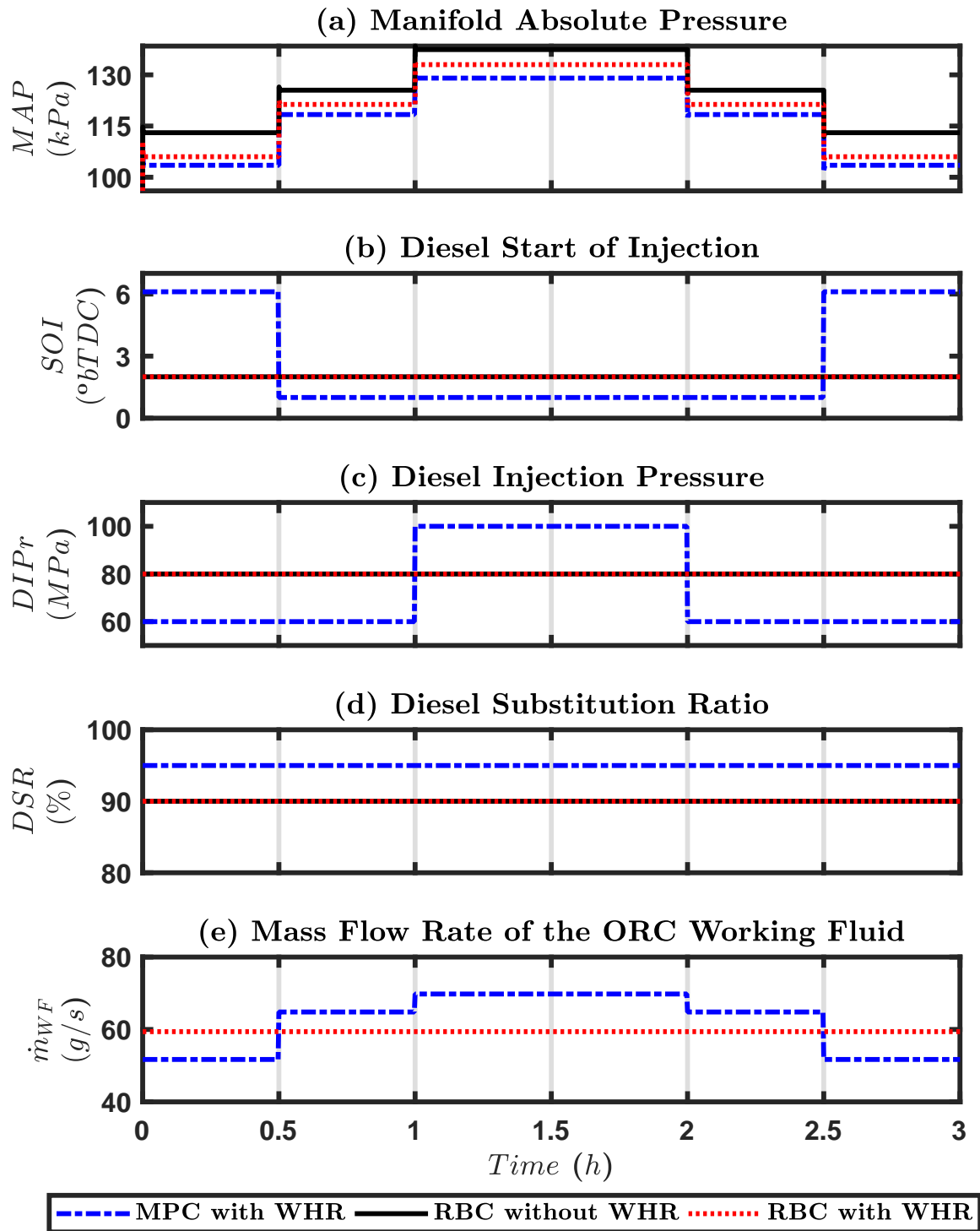
Figure 3.14: Controller outputs when the designed EMPC is applied to the combined ICE and WHR system. The controller outputs are compared with the two RBCs for the same conditions as those in Fig. 3.13.

126

of MAP is interpolated (Fig. 3.12) in accordance to the required ICE power (P^{ICE}). The designed EMPC optimally chooses the values of the engine and WHR control variables to (a) minimize the fuel consumption; and (b) meet exhaust gas temperature constraint as shown in Fig. 3.15.

Fig. 3.15(a) shows a reduction in fuel consumption of the ICE as a result of two factors: (i) adding WHR, (ii) changing RBC to EMPC. The fuel consumed by the ICE over the simulation time for the three control systems is shown in Table 3.4. This is calculated by integrating the fuel consumption rate of the ICE (Fig. 3.15(a)) over the simulation time. Fig. 3.15(b) shows that the designed EMPC is also able to meet the exhaust gas temperature constraint and controls $T_{exh}^{WHR,out}$ such that it is always above the minimum required limit. The exhaust gas temperature constraint is determined by adding 10 K to the minimum temperature for exothermic reactions to take place in the catalyst (i.e., 473 K) for a typical diesel ICE [147]. In addition, it should be noted that, the required $\dot{m}_{WF}$ in RBC was calibrated to maximize the fuel efficiency of the ICE. In tune with that, Fig. 3.15(b) shows that $T_{exh}^{WHR,out}$ violates the minimum allowed temperature at least 33% of the times.
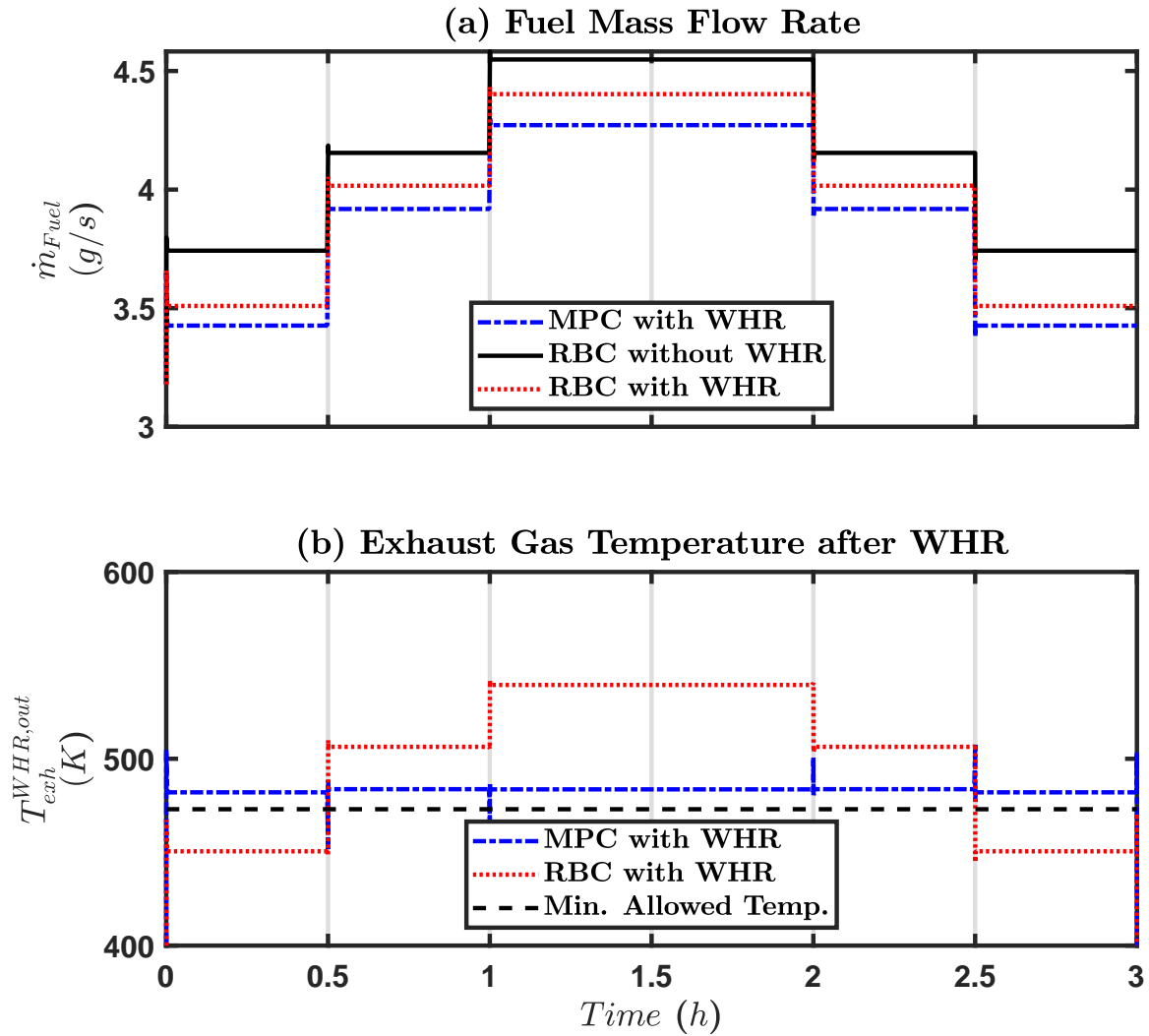
Figure 3.15: Comparison of the system outputs for the same conditions as those in Fig. 3.13.

3.5.2.3 Variable Temperature Tracking

The controller will encounter situations dictated by exhaust aftertreatment system conditions. The controller should be capable of (i) maintaining the exhaust gas temperature at the inlet of the aftertreatment system to be greater than the minimum

temperature required for exothermic reactions to take place in the catalyst, and (ii) raising the exhaust gas temperature at the inlet of the aftertreatment system high enough for efficient DPF regeneration whenever needed. In tune with that, variable exhaust gas temperature constraint is considered in the designed EMPC. To illustrate the controller performance for a case study, Fig. 3.15(b) is changed to a variable exhaust gas temperature constraint by considering the DPF regeneration temperature for a typical diesel ICE [149] from time 1:15 to 1:35 hours. In addition, the same reference power (P^{Ref}) as shown in Fig. 3.13 is used. Fig. 3.16 shows the results of the designed controllers in meeting $T_{exh}^{WHR,out}$ constraint. The designed EMPC optimally adjusts the control outputs such that the constraints are never violated.

The fuel consumed by the ICE over the simulation time for the three control systems is shown in Table 3.5. By comparing Table 3.4 and Table 3.5, we can observe:

† the fuel consumed reduced when RBC was applied to the combined ICE and WHR system because (i) the required $\dot{m}_{WF}$ in RBC was calibrated to minimize

Table 3.5
Fuel consumption comparison among the three system and control configurations studied for the case of (i) <u>variable</u> exhaust temperature constraint, and (ii) RBC defined not to violate exhaust temperature constraint.

| System	Control	Fuel Consumed (kg)	Fuel Saving* (%)
ICE	RBC	44.8	-
ICE + WHR	RBC	43.2	3.6
ICE + WHR	EMPC	42	6.3

* Percentages are calculated by comparing with the baseline RBC without WHR.
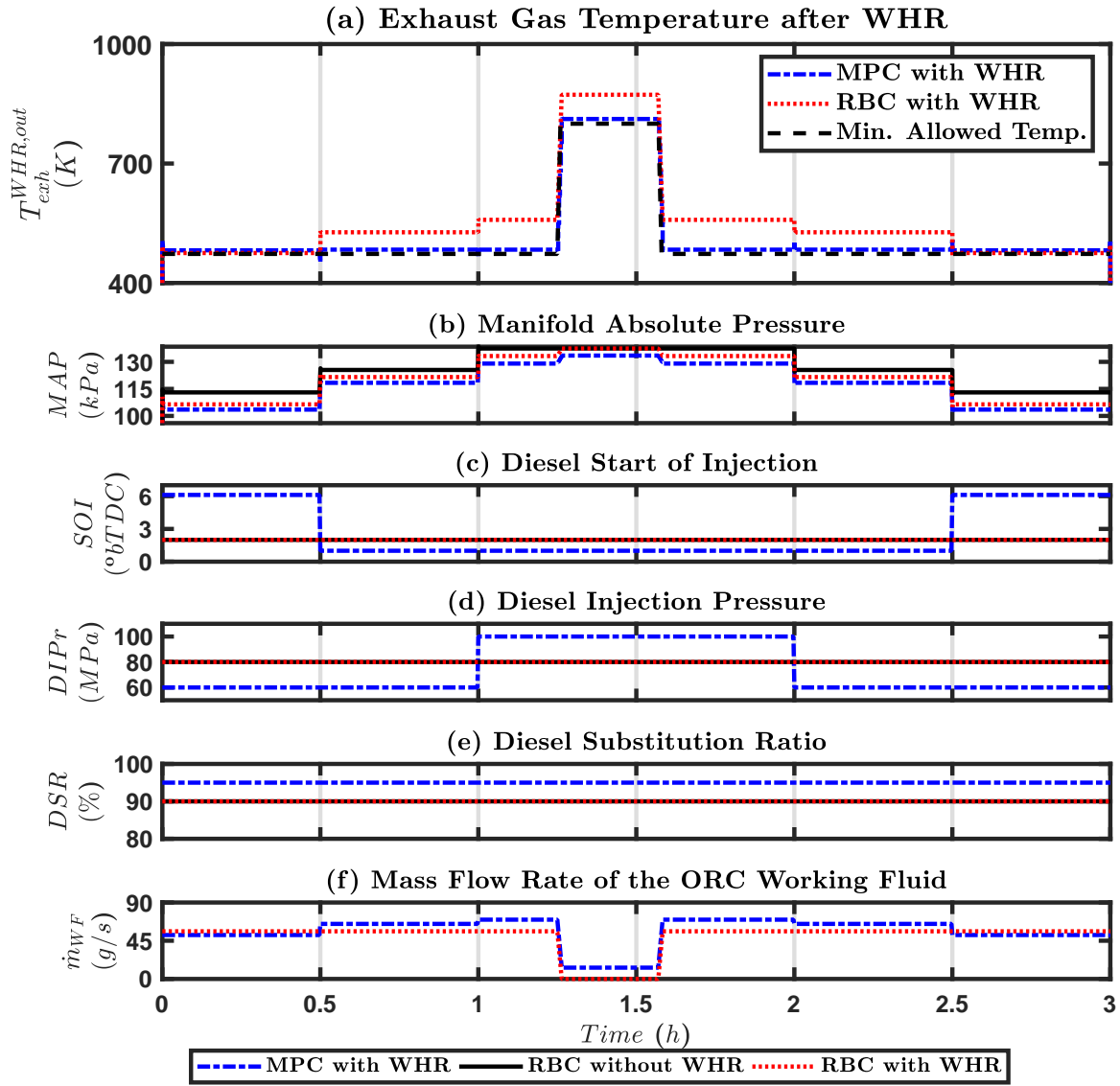
Figure 3.16: Controller outputs when the designed EMPC is applied to the combined ICE and WHR system. The controller outputs are compared with the two RBCs for the same conditions as those in Fig. 3.13.

exhaust temperature constraint violation, (ii) the controller switches off WHR during DPF regeneration requirement for 20 minutes; and

† the fuel consumed increased when the designed EMPC was applied to the combined ICE and WHR system because of the DPF regeneration requirement for

20 minutes.

The Sankey diagrams in Fig. 3.17 show the energy distribution in all three systems for the conditions in Fig. 3.16. This figure shows the results for keeping the generator output (i.e. 0.76 GJ) the same, while the required fuel supply is reduced by including WHR and using EMPC. Fig. 3.17(a) shows the amount of fuel energy being converted to useful electrical energy when RBC is applied to ICE system without WHR. This electrical energy input is considered as the baseline requirement. Fig. 3.17(b) shows that when RBC is applied to the combined ICE and WHR system, the baseline electrical energy output is obtained by using 3.5% less fuel energy, when compared to RBC applied to ICE system without WHR. This is due to the aid of WHR system, whose output is added to the output of the ICE though a gearbox. Finally, Fig. 3.17(c) shows that when the designed optimal EMPC is applied to the combined ICE and WHR system, the baseline electrical energy output is obtained by using 2.6% less fuel energy, when compared to RBC applied to the combined ICE and WHR system. This is because the designed EMPC optimally coordinates the values of MAP, SOI, $DIPr$, DSR, and $\dot{m}_{WF}$ to:

† maximize the ICE brake thermal efficiency (i.e., efficiency in converting fuel chemical energy to ICE mechanical energy);

† maximise the available exhaust thermal energy in the ICE whenever desirable; and

(a) RBC for ICE

ICE Mechanical Energy
0.84 GJ (41.6%)

System Electrical Energy
0.76 GJ (37.6%)

Fuel Energy
2.02 GJ (100%)

ICE + TC

ICE Exhaust Energy
0.62 GJ (30.7%)

Generator

Generator Energy Losses
0.08 GJ (4%)

ICE Energy Losses
0.56 GJ (27.7%)

(b) RBC for ICE+WHR

ICE Mechanical Energy
0.81 GJ (41.6%)

Gear Box

ICE+WHR Mechanical Energy
0.84 GJ (43%)

Generator

System Electrical Energy
0.76 GJ (39%)

Fuel Energy
1.95 GJ (100%)

ICE + TC

ICE Exhaust Energy
0.6 GJ (30.7%)

WHR

WHR Mechanical Energy
0.04 GJ (2.1%)

Gear Box Energy Losses
0.02 GJ (0.9%)

Generator Energy Losses
0.08 GJ (4.1%)

ICE Energy Losses
0.54 GJ (27.7%)

(c) EMPC for ICE+WHR

ICE Mechanical Energy
0.81 GJ (42.7%)

Gear Box

ICE+WHR Mechanical Energy
0.84 GJ (44.2%)

Generator

System Electrical Energy
0.76 GJ (40%)

Fuel Energy
1.9 GJ (100%)

ICE + TC

ICE Exhaust Energy
0.59 GJ (31.1%)

WHR

WHR Mechanical Energy
0.05 GJ (2.6%)

Gear Box Energy Losses
0.02 GJ (1.1%)

Generator Energy Losses
0.08 GJ (4.2%)

ICE Energy Losses
0.5 GJ (26.3%)

Figure 3.17: Energy distribution of the three designed controllers. The energy distribution is shown for the conditions in Fig. 3.16. The abbreviations used are ICE: Internal Combustion Engine, TC:Turbo-Charger, and WHR: Waste Heat Recovery.

† maximise the efficiency of the WHR system.

Furthermore, Appendix A shows the details needed for the computation of energy balance of the three systems studied in Fig 3.17.

3.5.3 Summary and Conclusions

Section 3.5 presented the design of an energy based model predictive controller (EMPC) to (i) minimize the fuel consumption, and (ii) meet time-varying exhaust gas temperature constraint for a combined ICE and WHR system to provide auxillary power in buildings. The exhaust gas temperature constraint represents light-off temperature requirements of the exhaust aftertreatment systems and also the required temperature for efficient DPF regeneration. For this section, control-oriented models for ICE system and WHR system were developed and then incorporated into an EMPC framework to optimally coordinate the ICE and WHR systems in accordance with the reference power demand. The main findings from Section 3.5 show that the designed EMPC framework:

† with <u>constant</u> exhaust gas temperature (T_{exh}) constraint provides up to 6.7% fuel saving compared to the baseline experimentally calibrated rule based controller (RBC) for the ICE system without WHR;

† with <u>time-varying</u> T_{exh} constraint provides up to 6.3% fuel saving compared to the applied RBC for the ICE system without WHR;

† improves the fuel saving by 2.5%, compared to the RBC for the combined ICE and WHR system when RBC is calibrated to <u>maximize fuel efficiency</u>;

† improves the fuel saving by 2.7%, compared to the RBC for the combined ICE and WHR system when RBC is calibrated to <u>minimize T_{exh} constraint violation</u>;

† reduces the calibration effort required of the ICE by at least a few thousand operating points compared to the applied RBC; and

† meets both constant and time-varying exhaust gas temperature (T_{exh}) constraints without any violations, while the RBC failed to meet T_{exh} constraints in over 33% of the tested conditions.

3.6 Exergy Based Model Predictive Control (XMPC) for Automotive Applications - Framework Design, Results and Analysis

3.6.1 Structure of the Designed Exergy Based Model Predictive Control (XMPC)

According to SLT, the second law efficiency (η_{II}) is defined as:

$$\eta_{II} = \frac{\dot{X}_{Rec}}{\dot{X}_{Supp}} = 1 - \frac{\dot{X}_{Dest}}{\dot{X}_{Supp}} \tag{3.26}$$

where, $\dot{X}_{Rec}$, $\dot{X}_{Supp}$ and $\dot{X}_{Dest}$ are the rate of exergy recovered, supplied, and destroyed, respectively.

From Equation (3.26), it is clear that reducing the exergy destruction or increasing the exergy recovered when the exergy supplied is constant will increase the second law efficiency of the system. Therefore, in this study, the optimizer decreases the ratio of exergy destruction in the ICE + TC ($\dot{X}_{Dest}^{Engine}$) to the exergy supplied to the ICE + TC ($\dot{X}_{Supp}^{Engine}$) while increasing the ratio of exergy recovered in the WHR ($\dot{X}_{Rec}^{WHR}$) to

the exergy supplied to the WHR ($\dot{X}_{Supp}^{WHR}$), along with meeting system the constraints.
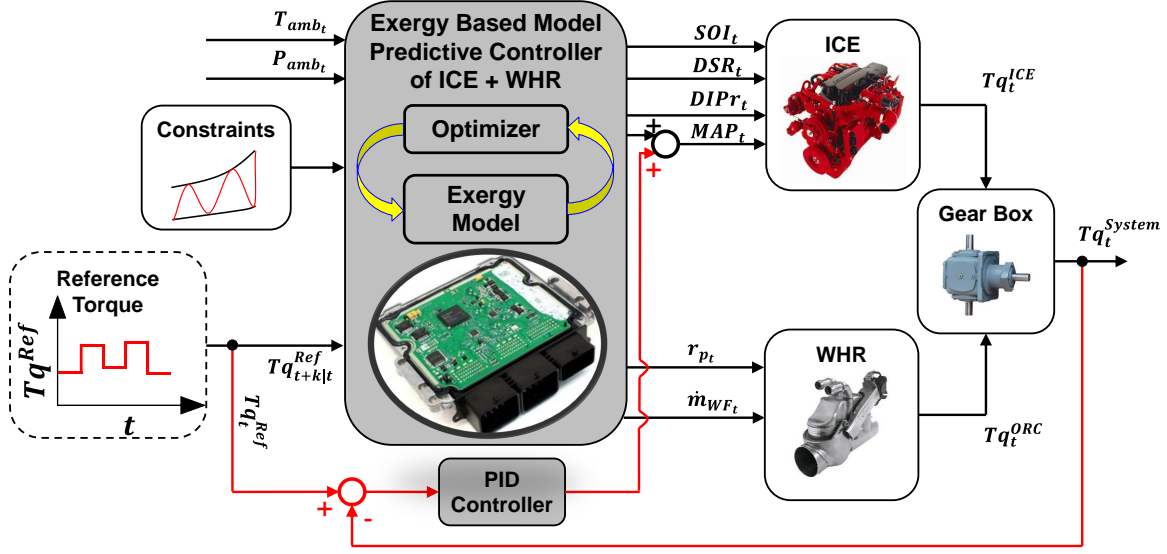
Figure 3.18: Structure of the designed XMPC for the combined ICE and WHR system.

Fig. 3.18 shows the structure of the exergy based MPC (XMPC) framework designed to (a) minimize the ICE fuel consumption; and (b) enforce the exhaust gas temperature constraint of the ICE when integrated with a WHR system. The objective function in Equation (3.27) is formulated to maximize the second law efficiency of the system. The system is subject to the constraints listed in Equations (3.28a) through (3.28l). The optimization problem is solved at each time step, to find the current and future values of diesel injection pressure ($DIPr$), diesel substitution ratio (DSR), diesel start of injection (SOI), manifold absolute pressure (MAP), operating pressure ratio (r_p) of the ORC, and mass flow rate of the WF ($\dot{m}_{WF}$) in the ORC. The input for the MPC optimization model is the required torque (Tq^{Ref}).

$$\min_{MAP,SOI,DIPr,DSR,\dot{m}_{WF},r_p} \left(\begin{bmatrix} \dot{X}_{Dest}^{Engine} \\ \dot{X}_{Supp}^{Engine} \end{bmatrix} - \begin{bmatrix} \dot{X}_{Rec}^{WHR} \\ \dot{X}_{Supp}^{WHR} \end{bmatrix} \right) \tag{3.27}$$

Subject to the following constraints:

$$\dot{X}_{Dest_{t+k|t}}^{Engine} = \alpha(p_{amb_{t+k|t}}, T_{amb_{t+k|t}}, MAP_{t+k|t}, SOI_{t+k|t}, DIPr_{t+k|t}, DSR_{t+k|t}) \tag{3.28a}$$

$$\dot{X}_{Supp_{t+k|t}}^{Engine} = \beta(p_{amb_{t+k|t}}, T_{amb_{t+k|t}}, MAP_{t+k|t}, DSR_{t+k|t}) \tag{3.28b}$$

$$\dot{X}_{Rec_{t+k|t}}^{WHR} = \lambda(\dot{m}_{WF_{t+k|t}}, r_{p_{t+k|t}}) \tag{3.28c}$$

$$\dot{X}_{Supp_{t+k|t}}^{WHR} = \Lambda(p_{amb_{t+k|t}}, T_{amb_{t+k|t}}, MAP_{t+k|t}, SOI_{t+k|t}, DIPr_{t+k|t}, DSR_{t+k|t}) \tag{3.28d}$$

$$Tq_{t+k|t}^{ICE} = \Upsilon(MAP_{t+k|t}, SOI_{t+k|t}, DIPr_{t+k|t}, DSR_{t+k|t}) \tag{3.28e}$$

$$Tq_{t+k|t}^{ORC} = \Pi(\dot{m}_{WF_{t+k|t}}, r_{p_{t+k|t}}) \tag{3.28f}$$

$$Tq_{t+k|t}^{Ref} = Tq_{t+k|t}^{Engine} + Tq_{t+k|t}^{ORC} \tag{3.28g}$$

$$\underline{x_i} \leq x_{i_{t+k|t}} \leq \overline{x_i} \tag{3.28h}$$

$$-\widehat{x_i} \leq \frac{d(x_{i_{t+k|t}})}{dt} \leq +\widehat{x_i} \tag{3.28i}$$

$$\underline{T_{exh_{t+k|t}}} \leq \Omega(MAP_{t+k|t}, SOI_{t+k|t}, DIPr_{t+k|t},$$

$$DSR_{t+k|t}, \dot{m}_{WF_{t+k|t}}, r_{p_{t+k|t}}) \leq \overline{T_{exh_{t+k|t}}} \tag{3.28j}$$

$$\underline{\omega} \leq \omega_{t+k|t} \leq \overline{\omega} \tag{3.28k}$$

$$\underline{Tq^{Engine}} \leq Tq_{t+k|t}^{Engine} \leq \overline{Tq^{Engine}} \tag{3.28l}$$

$$\underline{Tq^{ORC}} \leq Tq_{t+k|t}^{ORC} \leq \overline{Tq^{ORC}} \tag{3.28m}$$

Equation (3.28a) and Equation (3.28b) represent the rate of exergy destruction in the ICE + TC and the supplied exergy to the ICE + TC, respectively; Equation (3.28c) and Equation (3.28d) show the rate of exergy recovered by the WHR and the exergy supplied to the WHR, respectively; (3.28e) and (3.28f) constitute the torque of the ICE and ORC, respectively; (3.28g) is the constraint to keep the system output torque equal to the reference (required) torque; (3.28h) limits the control variables (represented by x_i) between their minimum and maximum values; (3.28i) represents the ramp limits of all the control variables; (3.28j) limits the temperature of the exhaust gas after the WHR system within the lower and higher exhaust gas temperature bounds; (3.28k) limits the angular speed of the system; (3.28l) and (3.28m) limit the ICE torque and ORC output torque in the WHR, respectively. In addition, Fig. 3.18 shows that a PID controller is designed in parallel to the designed XMPC. The XMPC provides the optimum trajectory for the engine control inputs (SOI, DSR, $DIPr$, MAP) and WHR control input (r_p, $\dot{m}_{WF}$). The XMPC mainly acts as a feedforward optimal controller. Then, the PID controller is added as a feedback controller for Tq^{Ref} tracking. The PID controller adjusts MAP because it is the dominant variable affecting the total system torque (Tq^{System}).

3.6.2　Control Results

The plant models and desired controllers are implemented in MATLAB®. The system synchronous speed was fixed at 1200 rpm and simulations were done for 10 seconds (i.e., 100 engine cycles). For the XMPC formulation, YALMIP Toolbox [107] is used for a symbolic interface with MATLAB® solvers. The prediction horizon of 1 second is applied, and the FMINCON solver is utilized. The simulation time to real time ratio was 5.2 when the optimization problem was run in a computer with Intel® Core™ i7-8700K CPU @ 3.7 GHz with 32 GB of RAM. Further reduction in the computation cost is needed for the designed XMPC to run in real time on the engine control module (ECM). This can be done by using methods of explicit MPC [63] and fast MPC [65].

3.6.2.1　Rule Based Control (RBC)

An RBC framework is designed to provide a baseline for comparison against the designed MPC framework. The control flow of the designed RBC is shown in Fig. 3.19. The RBC represents a fully calibrated engine operation done by the engine test cell calibration engineer. Fig. 3.19 shows that the torque from the ICE (Tq^{ICE}) is calculated as the difference of the torque from ORC (Tq^{ORC}) and the total requested

reference torque (Tq^{Ref}). But, Tq^{ORC} is proportional to the mass flow rate of the WF to the ORC ($\dot{m}_{WF}$). In addition, $\dot{m}_{WF}$ and the operating pressure of the ORC (r_p) is set to 0 if the system does not have a WHR system. If the system has a WHR, then r_p is set to a nominal value to maximise the efficiency of the ORC. The required $\dot{m}_{WF}$ is calibrated to maximise the fuel conversion efficiency; while satisfying the exhaust aftertreatment system temperature requirement as mush as possible. For a given ICE speed and Tq^{ICE}; SOI, $DIPr$, and DSR are set to nominal values from the calibration tables populated from the ICE test bench data. Finally, for a given Tq^{ICE}, SOI, $DIPr$, and DSR; MAP is obtained using a 1-D table. It should be noted that, measurements from at least 3000 operating points were recorded to populate the ICE calibration tables.
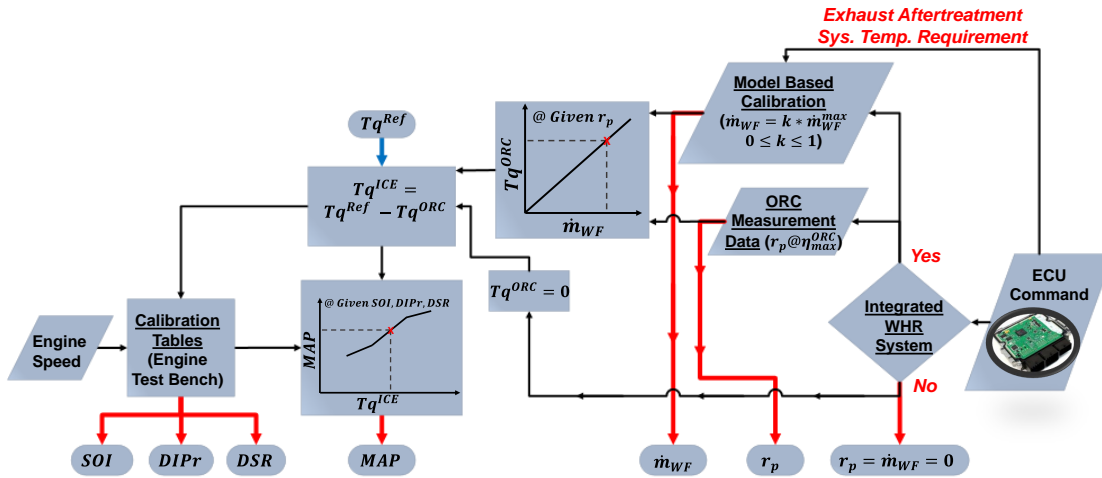
Figure 3.19: Control flow of the baseline rule based controller. The calibration tables are populated with the measurements from a fully calibrated engine.
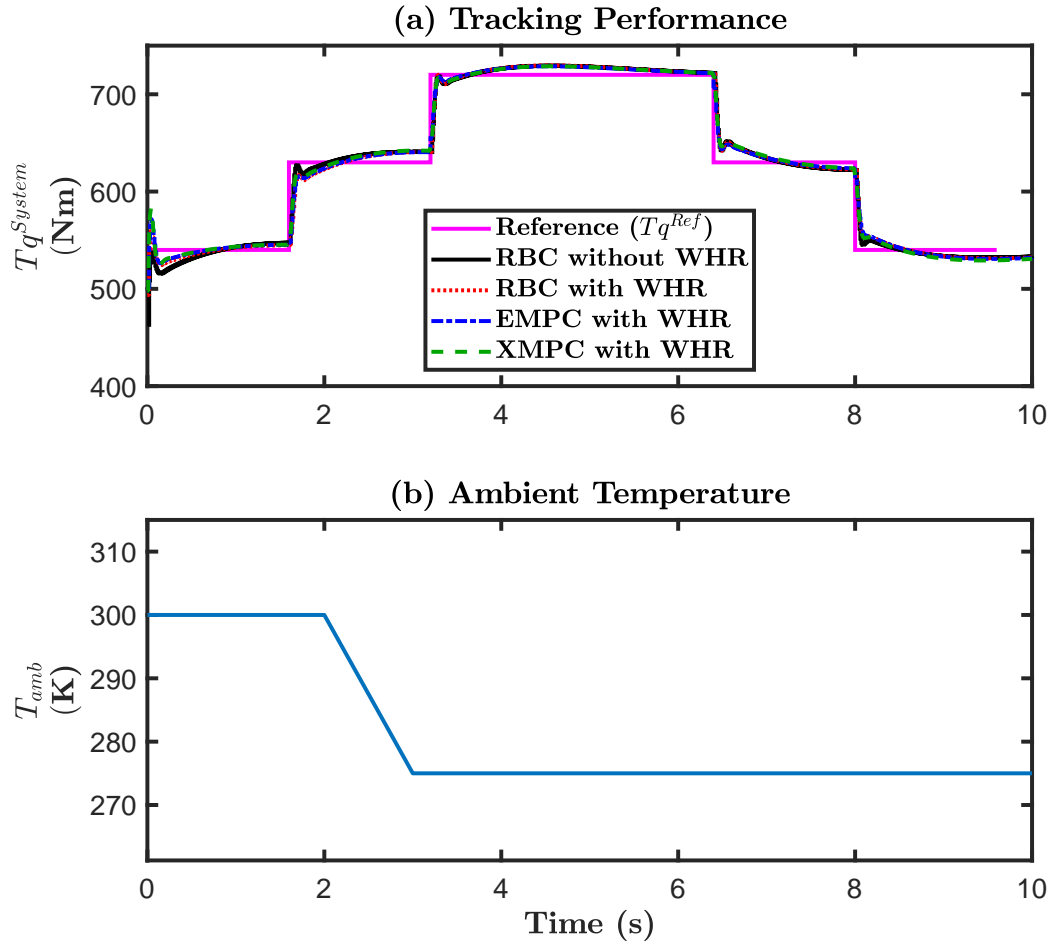
Figure 3.20: Tracking performance the four designed controllers. The torque tracking error of all controllers is similar and the maximum tracking error is less than 3%. Ambient Pressure = 96 kPa, ICE speed = 1200 rpm, and EGR = 0%.

3.6.2.2 Fuel Saving

In this section, the fuel saving potential of the designed control framework is discussed. Here, the controller performance is evaluated by demanding the same reference torque (Tq^{Ref}) and comparing the outputs from four controllers including (i) the designed

XMPC framework when applied to the combined ICE and WHR system, (ii) the energy based MPC (EMPC) framework when applied to the combined ICE and WHR system, (iii) the RBC when applied to the ICE system without WHR, and (iv) the RBC when applied to the combined ICE and WHR system. It should be noted that the details of EMPC are given in Section 3.4. Fig. 3.20(a) shows the tracking performance of all the four controllers to meet requested torque. Furthermore, Fig. 3.20(a) shows that the tracking of Tq^{Ref} is similar in all controllers; thus, their performance for saving fuel and meeting constraints can be compared. Additionally, Fig. 3.20(b) shows ambient temperature (T_{amb}) input to all the four controllers. Reduction in T_{amb} will lead to a decrease in the exergy destruction of the system (or increase in available exergy of the system).

Fig. 3.21 shows a comparison of the most sensitive control outputs among the four designed control systems. Fig. 3.21(a) shows the MAP because it is the dominant variable affecting the engine torque (Tq^{ICE}), considering a constant fuel-air equivalence ratio remains constant. Fig. 3.21(b) shows the $\dot{m}_{WF}$ because it is the dominant variable the affecting ORC torque (Tq^{ORC}). In RBC, the values for r_p, $\dot{m}_{WF}$, $DIPr$, DSR, and SOI are based on the test cell calibration for the required steady-state torque (Fig. 3.19); while the value of MAP is interpolated (Fig. 3.19) in accordance to the required ICE torque (Tq^{ICE}). EMPC adjusts the control inputs to the engine and WHR to maximize the first law (or energy conversion) efficiency of the combined ICE and WHR system. In other words, EMPC does not react to changes in the ambient

142
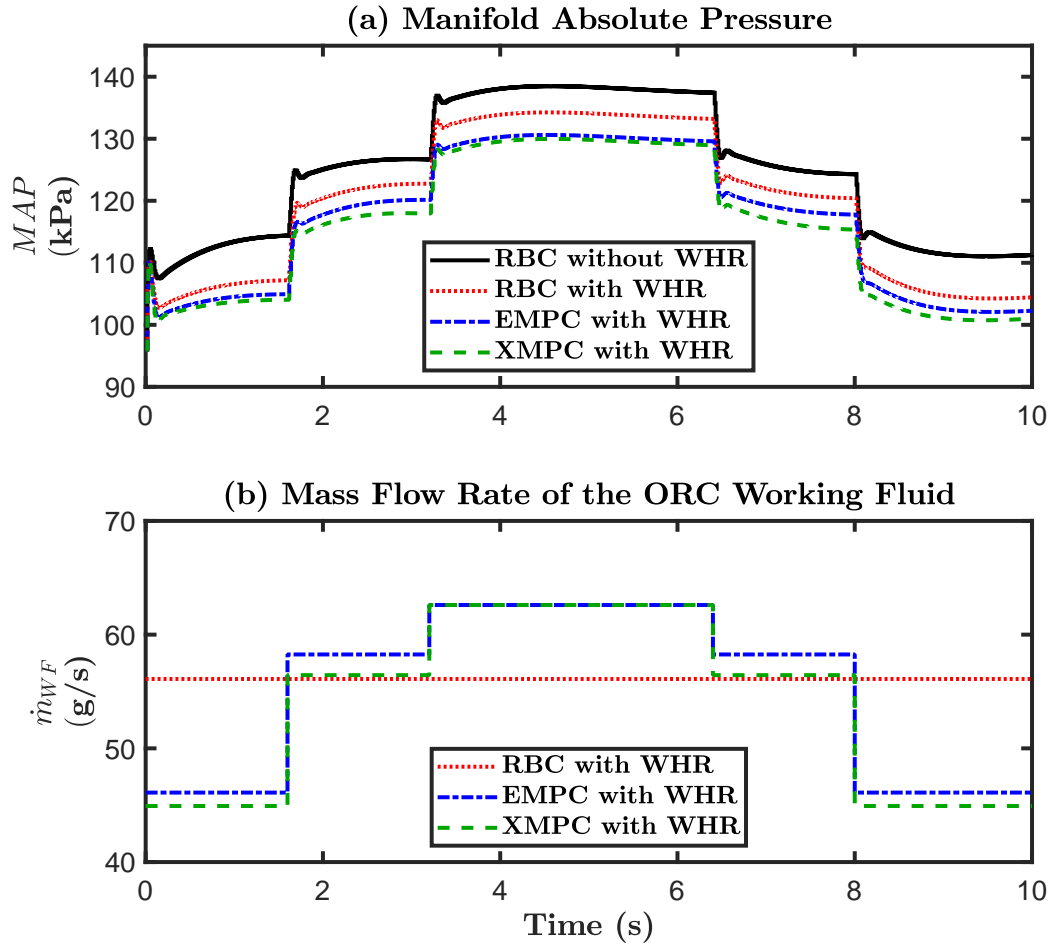
Figure 3.21: Controller outputs when the designed MPC is applied to the combined ICE and WHR system. The controller outputs are compared with the EMPC and the two RBCs for the same conditions as those in Fig. 3.20.

conditions. However, the designed XMPC optimally chooses the values of the control variables for the engine and WHR to maximize the second law (or exergy) efficiency of the combined ICE and WHR system. In other words, XMPC in real-time:

1. reduces the sources of irreversibilities (i.e., defficiency) in the combined ICE and WHR system (e.g., heat loss from ICE to ambient); and

2. reacts to the changes in the ambient conditions, since it affects the exergy

destruction and the system potential to do work (e.g., ORC work output from the thermal energy of exhaust gases).

Fig. 3.22(a) shows a reduction in fuel consumption of the ICE as a result of three factors: (i) adding WHR, (ii) changing from RBC to EMPC and (iii) changing from EMPC to XMPC. The fuel consumed by the ICE over the simulation time for the four control systems is shown in Table 3.6. This is calculated by integrating the fuel consumption rate of the ICE (Fig. 3.22(a)) over the simulation time. Fig. 3.22(b) shows
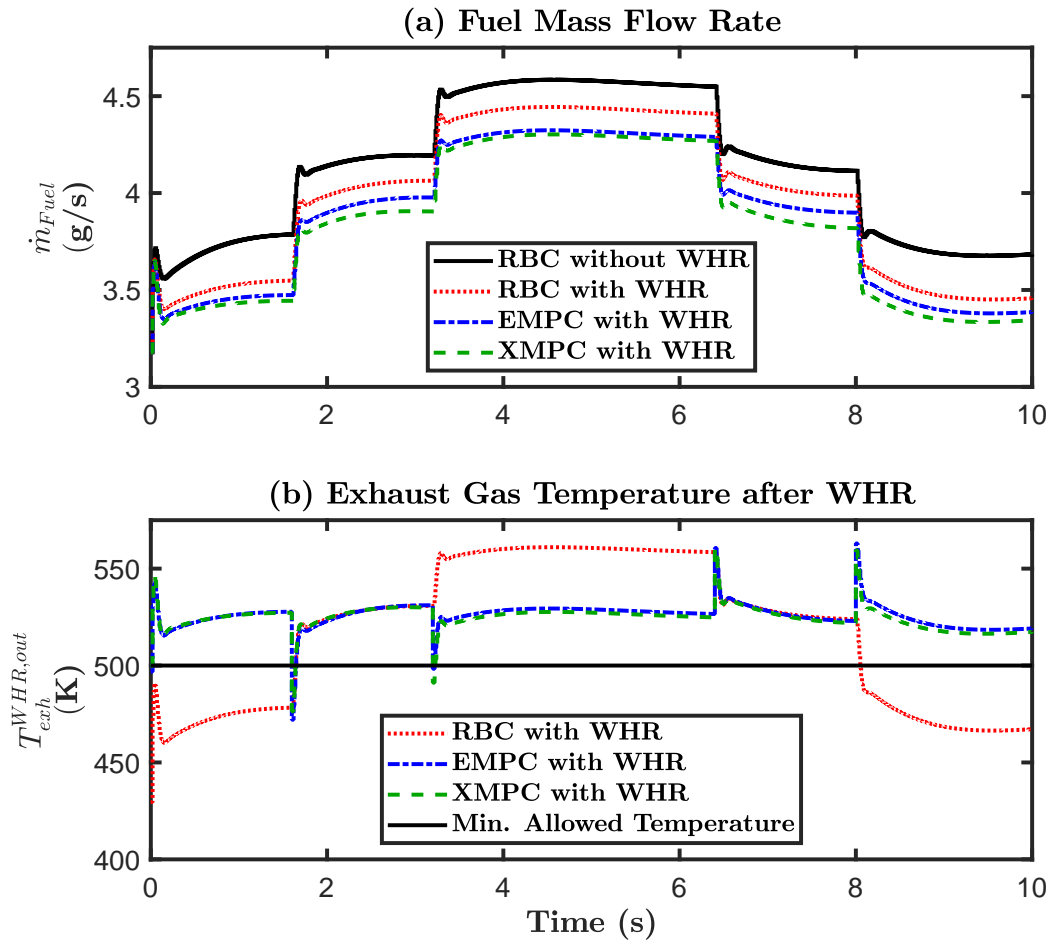
Figure 3.22: Comparison of the system outputs for the same conditions as those in Fig. 3.20.

that the EMPC and designed XMPC are able to meet the exhaust gas temperature

constraint and controls $T_{exh}^{WHR,out}$ such that it is above the minimum required limit in

over 98% of the tested conditions. The violations in $T_{exh}^{WHR,out}$ occur at 1.6 and 3.2

s for short periods of time (< 0.1 s) when demand torque (Tq^{Ref}) changes from one

steady-state value to another and the feedback PID controller dominates the feedfor-

ward MPC. The exhaust gas temperature constraint is determined by adding 25 K

to the minimum temperature for exothermic reactions to take place in the catalyst

(i.e., 473 K) for a typical diesel ICE [147]. Fig. 3.22(b) shows that $T_{exh}^{WHR,out}$ by RBC

violates the minimum allowed temperature at least 34% of the times.

3.6.2.3   Exhaust Gas Temperature Constraint

This section discusses the ability of the designed XMPC to satisfy the temperature

demand of a different exhaust aftertreatment system than what was discussed in

Section 3.6.2.2. The exhaust gas temperature constraint to the optimal EMPC and

Table 3.6
Comparing the engine fuel consumption among the four control
configurations studied in Section 3.6.2.2.

System	Control	Fuel Consumed (g)	Fuel Savings* (%)
ICE	RBC	41.3	-
ICE + WHR	RBC	39.7	4
ICE + WHR	EMPC	38.8	6.2
ICE + WHR	XMPC	38.3	7.2

* Percentages are calculated by comparing with the
baseline RBC without WHR.

XMPC are modified and it is obtained by adding 25 K to the minimum temperature required for exothermic reactions to take place in the methane oxidation catalyst (i.e., 575 K) used for a typical natural and diesel dual fuel ICE [150]. Fig. 3.23 shows that the optimal EMPC and the designed optimal XMPC are able to control the exhaust gas temperature such that the exhaust gas temperature is above the minimum required limit in over 99% of the tested conditions. Fig. 3.23 also shows that the applied RBC failed to meet $T_{exh}^{WHR,out}$ constraints in over 36% of the tested conditions. Finally, Table 3.7 shows the reduction in the fuel consumed by the ICE by adding WHR and/or by adding optimal MPC. Comparison of Table 3.7 with Table 3.6 shows the following.

1. The fuel reduction capability of the WHR system is reduced in Table 3.7. This is due to the need to increase the exhaust gas temperature.

2. The ratio of

   † the fuel saving percentage obtained by changing from RBC to the designed XMPC for the combined ICE + WHR system
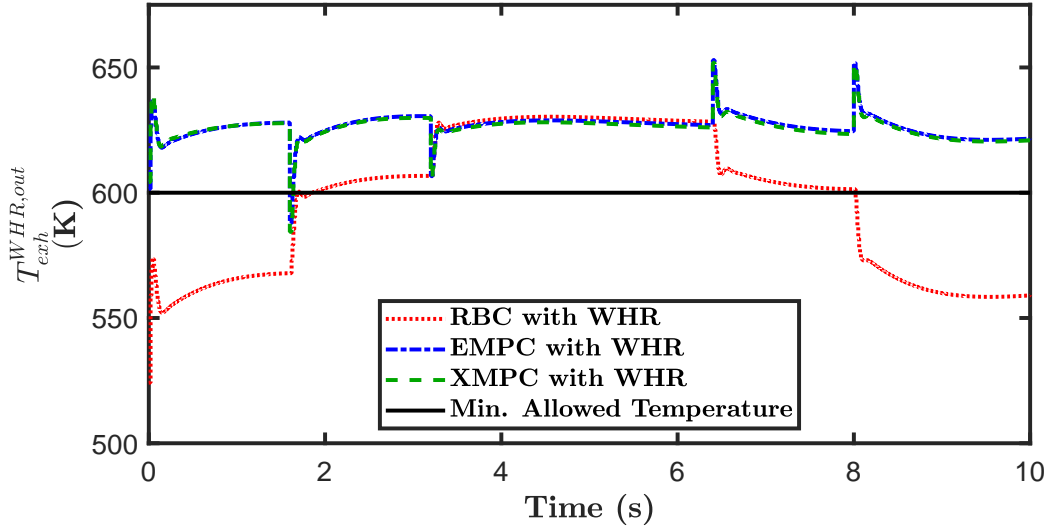
   to

   † the fuel saving percentage obtained by adding WHR to ICE controlled by RBC

   gives the fuel reduction capability of XMPC relative to adding WHR. Tables 3.6

and 3.7 show that the fuel reduction capability of XMPC relative to adding WHR is almost constant in both the cases and is 80% and 81%, respectively[2].

Figure 3.23: Comparison of the ICE exhaust gas temperature after the WHR system for the four control systems studied in Section 3.6.2.3.

Table 3.7

Comparing the engine fuel consumption among the four control configurations studied in Section 3.6.2.3.

System	Control	Fuel Consumed (g)	Fuel Savings* (%)
ICE	RBC	41.3	-
ICE + WHR	RBC	40	3.2
ICE + WHR	EMPC	39.2	5.1
ICE + WHR	XMPC	38.9	5.8

* Percentages are calculated by comparing with the baseline RBC without WHR.

---

[2]calculated as $\frac{FC_{ICE+WHR}^{XMPC} - FC_{ICE+WHR}^{RBC}}{FC_{ICE+WHR}^{RBC} - FC_{ICE}^{RBC}} \cdot 100$; where, FC_y^x is the fuel consumed by the ICE when x controller is applied to y system.

3.6.2.4 Energy and Exergy Analysis

In this section, energy and exergy based analyses are discussed for the combined ICE + WHR system when the designed XMPC is applied to the ICE + WHR system. The Sankey diagrams in Fig. 3.24 show the energy based analysis and the exergy based analysis for the conditions in Section 3.6.2.2. Appendix B shows the details needed for the computation of the energy and exergy balance in Fig 3.24. Fig. 3.24(a) shows that an energy based analysis only gives information on the amount of energy utilized for the final work delivery (i.e., 0.75 MJ), the amount of energy in the exhaust gas, and the amount of energy lost in converting the chemical energy from the fuel to the mechanical work delivery. But, exergy based analysis (Fig. 3.24(b)) shows the following.

1. The amount of exergy destroyed in all stages of energy conversion. These include exergy destroyed from converting the fuel chemical energy to mechanical work in the ICE and from converting the thermal energy from the exhaust gases to mechanical work in the WHR.

2. The amount of exergy recovered (i.e., energy utilized for useful work) from the fuel.

3. 67% of the exhaust gas energy has the potential to be converted to work in the WHR. This provides the ceiling of efficiency for WHR. However, the final

148

realised efficiency of the WHR is 11%.

4. Out of the 100% fuel energy (i.e., the ceiling of efficiency for ICE + WHR system), only 42% is converted to useful work.

5. The amount of not utilized exergy in the exhaust gas after WHR.

3.6.3 Summary and Conclusions

Section 3.6 presented the design of an exergy based model predictive controller (XMPC) to (i) minimize the fuel consumption, and (ii) meet exhaust gas temperature constraint for a combined ICE and WHR system. The exhaust gas temperature constraint represents light-off temperature requirements of the exhaust aftertreatment systems. Section 3.6 utilized the control-oriented models for the ICE system and WHR system (Section 3.3). These models were then incorporated into an XMPC framework to optimally coordinate the ICE and WHR systems in accordance with the reference torque demand. The main findings from Section 3.6 show that the designed XMPC framework:

† reduces the fuel consumption of the ICE by 7.2%; compared to the baseline RBC for the ICE system without WHR;
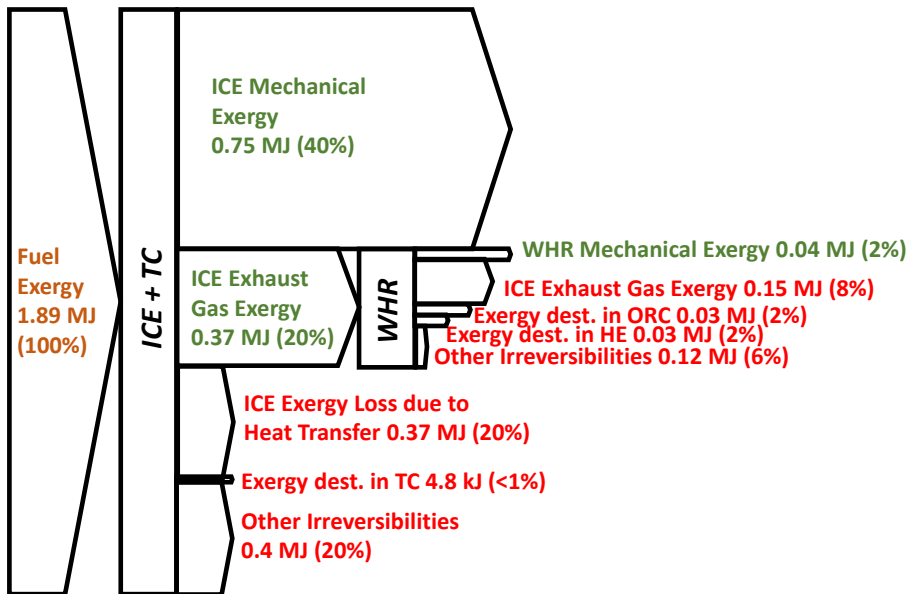
† improves the fuel saving by 3% and 1%, respectively; compared to the RBC

and EMPC for the combined ICE and WHR system;

(a) Energy Analysis
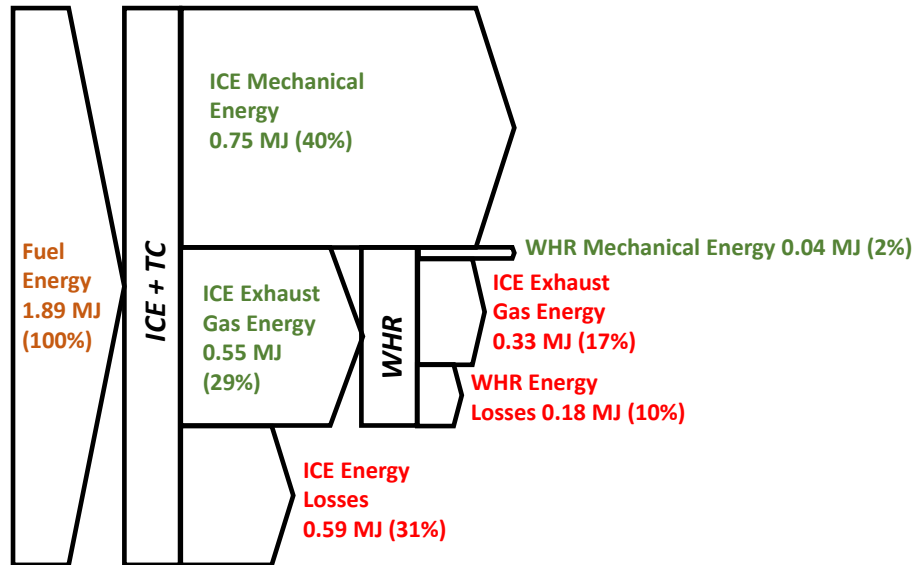
(b) Exergy Analysis

Figure 3.24: Energy and exergy distribution of the combined ICE and WHR System when the designed XMPC is applied. The abbreviations used are ICE: Internal Combustion Engine, TC: Turbo-Charger, WHR: Waste Heat Recovery, ORC: Organic Rankine Cycle, and HE: Heat Exchanger.

† reduces the calibration effort required of the ICE by at least a few thousand operating points compared to the applied RBC; and

† meets the exhaust gas temperature (T_{exh}) constraints without violations in over 98% of the tested conditions, while the RBC failed to meet T_{exh} constraints in over 35% of the tested conditions.

Chapter 4

Conclusions and Future Work

4.1   Summary and Conclusions

This dissertation presented the design of optimal model predictive control (MPC) frameworks for:

1. the building heating, ventilation, and air-conditioning (HVAC) system integrated with the micro-scale concentrated solar power (MicroCSP) system; and

2. the internal combustion engine (ICE) integrated with the waste heat recovery (WHR) system.

Chapter 2 of this dissertation shows that the design of optimal MPC for the combined building HVAC system and MicroCSP system reduces the energy consumption and the energy cost of the building HVAC system. Additionally, Chapter 3 shows that the design of optimal MPC for the combined ICE and WHR system reduces the fuel consumption of the ICE. Chapter 3 explores the application the ICE + WHR system for the transportation sector and electricity generation in buildings. Hence, Chapters 2 and 3 of this dissertation make important contributions to improving the energy efficiency of energy systems in heat and power applications.

In Chapter 2 of this PhD dissertation, MPC frameworks are designed based on either the energy, operational cost or the exergy of the combined MicroCSP and building HVAC system. The MPC frameworks are termed as energy based MPC (EMPC), energy cost based MPC (CMPC) and exergy based MPC (XMPC), respectively. EMPC is designed to minimize the energy consumption of the building HVAC system. CMPC is designed to minimize the energy cost of the building HVAC system in cases where the power grid has dynamic pricing (i.e., locational marginal pricing (LMP)). Finally, XMPC is designed to maximise the second law of thermodynamic efficiency of the combined MicroCSP and building HVAC system. In other words, XMPC is designed to maximise energy available in the MicroCSP system while minimising the irreversibilities (e.g. heat lost to the environment) in the combined MicroCSP and building HVAC system. Each of the designed MPC frameworks are evaluated by comparing them with a rule based controller (RBC). RBC is the simplest and most used

control technique for HVAC systems in buildings. It is based on a pre-determined set of rules that are implemented to control the behavior of a system.

The major findings and conclusions from Chapter 2 are:

Designed MPC vs. RBC

† The results of study for a sample sunny and cold day in Houghton, MI show that the building energy reduces by 38% when EMPC is applied instead of using the RBC. Furthermore, the application of CMPC reduces the building energy cost by 70%, compared to that in the RBC. Finally, XMPC reduces the building energy by 45%, compared to when RBC is applied.

Storage Sizing Effects

† It is critical to properly size the thermal energy storage (TES) capacity for a given building. For the conditions studied in Chapter 2, the maximum energy saving of the building is found to be at 38 kWh when EMPC is applied and 48 kWh when XMPC is applied, respectively instead of using the RBC. Furthermore, the building energy cost saving by applying CMPC instead of RBC reaches its maximum value starting from 114 kWh capacity. Overall, the capacity of TES needs to be chosen carefully to avoid unnecessary oversizing since after reaching the optimal capacity, the cost and energy savings do not change

any more even if the capacity is increased.

Prediction Uncertainty Effects

† In order to evaluate the effects of uncertainty in the future prediction of the solar irradiation, the ambient temperature, and/or LMP for the sample day, a Monte Carlo simulation (MCs) study was carried out. The results show that, by applying EMPC instead of the RBC, the building energy saving ranges from 34% to 42%. The building energy cost saving varies between 68% and 72% when CMPC is applied, compared to using RBC. Finally, when XMPC is applied instead of the RBC, the exergy savings of the system vary from 16% to 18%, which results in a building energy reduction from 44% to 47%.

Furthermore, the results from Chapter 2 show that XMPC offers the maximum building energy savings; but, the highly nonlinear exergy functions make XMPC the most computational expensive among the optimal controllers discussed.

In Chapter 3 of this PhD dissertation, EMPC and XMPC frameworks are designed and applied to the combined ICE and WHR system. It should be noted that, EMPC is designed for the combined ICE and WHR system as applied to transportation and building electricity generation applications; where as, XMPC is designed for the combined ICE and WHR system as applied to the transportation application. The effect of adding WHR and the effect of the designed MPC frameworks are evaluated

156

by comparing them with RBC applied to both the ICE system without WHR and the combined ICE and WHR system. RBC represents a fully calibrated engine operation done by the engine test cell calibration engineer.

The major findings and conclusions from Chapter 3 are:

Fuel Savings

† EMPC and XMPC when applied to the combined ICE and WHR system can provide 6% and 7% fuel saving, respectively; compared to the baseline RBC for the ICE system without WHR; and

† EMPC and XMPC improves the fuel saving by 2% and 3%, respectively; compared to the RBC for the combined ICE and WHR system.

Meeting Exhaust Gas Temperature Requirements

† The designed controller will encounter situations dictated by exhaust aftertreatment system conditions. More particularly, the controller should be capable of maintaining the exhaust gas temperature at the inlet of the aftertreatment system to be greater than the required catalyst light off temperature. The designed EMPC and XMPC meet the exhaust gas temperature (T_{exh}) constraints, while the RBC failed to meet T_{exh} constraints in over 33% of the tested conditions.

Controller Calibration Efforts

† The designed EMPC and XMPC reduces the calibration effort required of the ICE by at least a few thousand operating points compared to the applied RBC.

Further analyses of Chapter 3 shows that XMPC outperforms EMPC w.r.t. fuel savings in the ICE. Offline exergy based analysis on the system gives more sub-system optimization opportunity when compared to energy based analysis; but, XMPC is more computational expensive when compared to EMPC. In addition, the application of offline exergy based analysis (and XMPC) is more challenging than offline energy based analysis (and EMPC) due to difficulty in developing high-fidelity exergy based models.

4.2 Suggestions for Future Work

Despite the promising results of the proposed methodology presented in chapters of this dissertation, there is room for improvement and expanding the study. Here is the list of some research areas worthy of further investigation:

Controller Implementation

† Real-time implementation of the designed MPC on a building HVAC + MicroCSP test cell and an ICE + WHR test-cell represents the next steps to

realize the designed controllers from this PhD dissertation.

MPC for ICE + WHR with Noise and Emission Constraints

† In this dissertation, the effects of ICE on combustion noise and engine-out emission were not investigated when designing optimal MPCs for the combined ICE and WHR system. Noise and emissions can be included in the optimization problem as constraints.

MPC for ICE + WHR + Exhaust Aftertreatment System

† This dissertation showed the capability of the designed optimal MPCs for the combined ICE and WHR system to meet the exhaust temperature required for exothermic reactions in the exhaust aftertreatment system. However, meeting the exhaust temperature requirement does not fully satisfy the requirements of the exhaust aftertreatment system to meet the tail-pipe emissions requirements. Hence optimal MPC for the ICE + WHR + exhaust aftertreatment system can be designed to meet both the required power demand and tail-pipe emissions.

MPC for Building HVAC + MicroCSP with Grid Optimization

† This PhD dissertation briefly showed that the MicroCSP integration to the building can be extended to benefit the power grid via ancillary services. Indeed, CMPC, when applied to building HVAC + MicroCSP system, showed how the

MicroCSP allowed the building to react to the variable electricity pricing. This paves the way for more in-depth investigations of the potentials of MicroCSP to other types of ancillary services such as frequency regulation, and voltage control.

MPC for the Combined Building HVAC + MicroCSP + ICE + WHR

† Chapter 2 of this dissertation shows that the building HVAC system uses the combined heat and power from MicroCSP system when thermal energy is available in the thermal energy storage (TES) but relies on the power grid when thermal energy is not available in the TES. However, Chapter 3 shows that the building electricity needs can be met by the combined ICE and WHR system. Hence, it would be of interest to design MPC for the combined building HVAC, MicroCSP, ICE, and WHR system for optimal energy solutions in the building. This approach is imperative particularly in regions with less accessibility to the power grid.

Reduce Computational Cost of Exergy based MPC

† Chapters 2 and 3 of this dissertation show that the exergy based MPC control of the combined building HVAC + MicroCSP system and the combined ICE + WHR system is very computationally expensive, as compared to the application of energy based MPC. This is because of the non-linearity of exergy based

formulation of the energy systems. The computational cost of exergy based MPC can be reduced by using the control techniques of neuro fuzzy inference system [151, 152], reinforcement learning [153, 154] and imitation control [155, 156].

Integrate Exergy Effects of the System into Energy Based MPC Objective

† Another way to reduce the computational cost of exergy based MPC is by integrating the exergy effects of the system into the objective function of a energy based MPC. For example, if analysis of the system shows that first law efficiency of the system increases with the decrease in ambient temperature. Then, the first law efficiency of the system can be multiplied by the ambient temperature to form the objective function of the MPC. Such an approach will reduce the computational cost of the designed MPC compared to the exergy based MPC while improving the performance of the designed MPC compared to the energy based MPC.

References

[1] M. Toub, C. R. Reddy, M. Razmara, M. Shahbakhti, R. D. Robinett, and G. Aniba, "Model Predictive Control for MicroCSP integration into a building HVAC system," in *2018 IEEE 14th International Conference on Control and Automation (ICCA)*, pp. 890–895, IEEE, 2018.

[2] C. R. Reddy, M. Toub, M. Razmara, M. Shahbakhti, R. D. Robinett III, and G. Aniba, "Modeling and optimal control of Micro-CSP and a building HVAC system to minimize electricity cost," in *Dynamic Systems and Control Conference*, vol. 51906, 10 pages, American Society of Mechanical Engineers, 2018.

[3] M. Toub, C. R. Reddy, M. Razmara, M. Shahbakhti, R. D. Robinett III, and G. Aniba, "Model-based predictive control for optimal MicroCSP operation integrated with building HVAC systems," *Energy Conversion and Management*, vol. 199, 16 pages, 2019.

[4] C. R. Reddy, M. Razmara, M. Shahbakhti, and R. D. Robinett, "Optimal

exergy-wise predictive control for a combined MicroCSP and HVAC system in a building," in *2019 American Control Conference (ACC)*, pp. 235–240, IEEE, 2019.

[5] C. Reddy, M. Shahbakhti, R. Robinett, and M. Razmara, "Exergy-wise predictive control framework for optimal performance of MicroCSP systems for HVAC applications in buildings," *Energy Conversion and Management*, vol. 210, 15 pages, 2020.

[6] M. Toub, C. R. Reddy, R. D. Robinett III, and M. Shahbakhti, "Integration and Optimal Control of MicroCSP with Building HVAC Systems: Review and Future Directions," *Energies*, vol. 14, no. 3, 41 pages, 2021.

[7] C. R. Reddy, V. B. Vinhaes, R. D. Robinett, J. D. Naber, and M. Shahbakhti, "Model Predictive Control of a Waste Heat Recovery System Integrated with a Dual Fuel Natural Gas-Diesel Engine," in *2021 American Control Conference (ACC)*, pp. 1842–1847, IEEE, 2021.

[8] C. R. Reddy, V. B. Vinhaes, J. D. Naber, R. D. Robinett, and M. Shahbakhti, "Model Predictive Control of a Dual Fuel Engine Integrated with Waste Heat Recovery used for Electric Power in Buildings," *Optimal Control Application and Methods*, 20 pages, 2022.

[9] Y.-H. Lee, S. Bae, S.-s. Hwang, J.-H. Kim, K.-N. Kim, Y.-H. Lim, M. Kim,

S. Jung, and H.-J. Kwon, "Association between air conditioning use and self-reported symptoms during the 2018 heat wave in korea," *Journal of preventive medicine and public health*, vol. 53, no. 1, 11 pages, 2020.

[10] R. M. Trigo, J. M. Pereira, M. G. Pereira, B. Mota, T. J. Calado, C. C. Dacamara, and F. E. Santo, "Atmospheric conditions associated with the exceptional fire season of 2003 in portugal," *International Journal of Climatology: A Journal of the Royal Meteorological Society*, vol. 26, no. 13, pp. 1741–1757, 2006.

[11] R. E. Godagnone and C. Juan, "Soils of the argentine antarctica," in *The Soils of Argentina*, pp. 195–207, Springer, 2019.

[12] H. Ritchie and M. Roser, "Urbanization," *Our World in Data*, 2018. Available at *https: // ourworldindata. org/ urbanization* (Accessed on 15 November 2021).

[13] IEA (2020), "Tracking buildings 2020," Available at *https: // www. iea. org/ reports/ tracking-buildings-2020* (Accessed on 18 October 2020).

[14] J. Jazaeri, R. L. Gordon, and T. Alpcan, "Influence of building envelopes, climates, and occupancy patterns on residential hvac demand," *Journal of Building Engineering*, vol. 22, pp. 33–47, 2019.

[15] Energy Information Administration, "Annual energy outlook 2020," Available at *https: // www. eia. gov/ outlooks/ aeo/ pdf/ AEO2020. pdf* (Accessed on 18 January 2021).

[16] B. Soudan and A. Darya, "Autonomous smart switching control for off-grid hybrid pv/battery/diesel power system," *Energy*, vol. 211, 16 pages, 2020.

[17] D. Wang, S. Govindan, A. Sivasubramaniam, A. Kansal, J. Liu, and B. Khessib, "Underprovisioning backup power infrastructure for datacenters," pp. 177–192, 19th International Conference on Architectural Support for Programming Languages and Operating Systems, 2014.

[18] P. M. Chakalian, L. C. Kurtz, and D. M. Hondula, "After the lights go out: Household resilience to electrical grid failure following hurricane irma," *Natural Hazards Review*, vol. 20, no. 4, 14 pages, 2019.

[19] Fortune Business Insights, "Diesel generator market size," Available at `https://www.fortunebusinessinsights.com/industry-reports/diesel-generator-market-100587` (Accessed on 18 February 2021).

[20] W. Luo, Z. Yang, Z. Li, J. Zhang, J. Liu, Z. Zhao, Z. Wang, S. Yan, T. Yu, and Z. Zou, "Solar hydrogen generation from seawater with a modified bivo4 photoanode," *Energy & Environmental Science*, vol. 4, no. 10, pp. 4046–4051, 2011.

[21] A. Steinfeld and R. Palumbo, "Solar thermochemical process technology," *Encyclopedia of physical science and technology*, vol. 15, no. 1, pp. 237–56, 2001.

[22] M. Razmara, G. R. Bharati, D. Hanover, M. Shahbakhti, S. Paudyal, and R. D. Robinett, "Enabling demand response programs via predictive control

of building-to-grid systems integrated with PV panels and energy storage systems," pp. 56–61, 2017 American Control Conference (ACC), May 2017.

[23] M. Razmara, G. Bharati, D. Hanover, M. Shahbakhti, S. Paudyal, and R. Robinett III, "Building-to-grid predictive power flow control for demand response and demand flexibility programs," *Applied Energy*, vol. 203, pp. 128–141, 2017.

[24] A. Ramos, M. A. Chatzopoulou, I. Guarracino, J. Freeman, and C. N. Markides, "Hybrid photovoltaic-thermal solar systems for combined heating, cooling and power provision in the urban environment," *Energy Conversion and Management*, vol. 150, pp. 838–850, 2017.

[25] M. Herrando, A. M. Pantaleo, K. Wang, and C. N. Markides, "Solar combined cooling, heating and power systems based on hybrid PVT, PV or solar-thermal collectors for building applications," *Renewable Energy*, vol. 143, pp. 637–647, 2019.

[26] Y. Gu, X. Zhang, J. A. Myhren, M. Han, X. Chen, and Y. Yuan, "Techno-economic analysis of a solar photovoltaic/thermal (PV/T) concentrator for building application in Sweden using Monte Carlo method," *Energy Conversion and Management*, vol. 165, pp. 8–24, 2018.

[27] J. Osborne, "Developing the australian solar cooling market: status update and lessons from the solar thermal industry," in *Proceedings of the Australian Solar Cooling 2013 Conference, North Ryde, Australia*, 11 pages.

[28] R. Dickes, O. Dumont, S. Declaye, S. Quoilin, I. Bell, and V. Lemort, "Experimental investigation of an orc system for a micro-solar power plant," in *2014 International Compressor Engineering Conference*.

[29] M. Ragheb, "Solar thermal power and energy storage historical perspective," Available at *http://mragheb.com/NPRE%20498ES%20Energy%20Storage% 20Systems/Solar%20Thermal%20Power%20and%20Energy%20Storage% 20Historical%20Perspective.pdf* (Accessed on 18 February 2019).

[30] J. Nayak, S. Kedare, R. Banerjee, S. Bandyopadhyay, N. Desai, S. Paul, and A. Kapila, "A 1 MW national solar thermal research cum demonstration facility at Gwalpahari, Haryana, India," *Current Science*, pp. 1445–1457, 2015.

[31] A. Maccari, D. Bissi, G. Casubolo, F. Guerrini, L. Lucatello, G. Luna, A. Rivaben, E. Savoldi, S. Tamano, and M. Zuanella, "Archimede Solar Energy Molten Salt Parabolic Trough Demo Plant: A Step Ahead towards the New Frontiers of CSP," *Energy Procedia*, vol. 69, pp. 1643–1651, May 2015.

[32] M. Orosz *et al.*, "Small scale solar ORC system for distributed power in Lesotho," in *Johannesburg, South Africa: Solar World Congress*, 2009.

[33] S. Quoilin, M. Orosz, H. Hemond, and V. Lemort, "Performance and design optimization of a low-cost solar organic Rankine cycle for remote power generation," *Solar Energy*, vol. 85, pp. 955–966, May 2011.

[34] M. Mitterhofer and M. Orosz, "Dynamic simulation and optimization of an

experimental micro-csp power plant," in *Energy Sustainability*, vol. 56840, 14 pages, American Society of Mechanical Engineers, 2015.

[35] S. Mishra, A. K. Jain, T. Singh, and R. Gupta, "Optimising Energy Dependency of VIT University," *Int. J. Sci. Eng. Res*, vol. 4, no. 7, 2013.

[36] A. Bianchini, A. Guzzini, M. Pellegrini, and C. Saccani, "Performance assessment of a solar parabolic dish for domestic use based on experimental measurements," *Renewable Energy*, vol. 133, pp. 382–392, 2019.

[37] M. Idrometano and A. S. A. Urbani, "66 congresso nazionale ati–rende (cosenza), 5-9 settembre 2011," in *Congresso Nazionale ATI–Rende (Cosenza)*, vol. 5, 9 pages, 2011.

[38] Y. Grosu, I. Ortega-Fernández, L. González-Fernández, U. Nithiyanantham, Y. F. Baba, A. Al Mers, and A. Faik, "Natural and by-product materials for thermocline-based thermal energy storage system at CSP plant: Structural and thermophysical properties," *Applied Thermal Engineering*, vol. 136, pp. 185–193, 2018.

[39] M. Kane, "Small hybrid solar power system," *Energy*, vol. 28, pp. 1427–1443, Nov. 2003.

[40] E. Xu, Q. Yu, Z. Wang, and C. Yang, "Modeling and simulation of 1 MW DAHAN solar thermal power tower plant," *Renewable Energy*, vol. 36, pp. 848–857, Feb. 2011.

[41] Q. Ha, "Data acquisition, monitoring and control for hybrid solar air-conditioners," *Gerontechnology*, vol. 11, no. 2, 2012.

[42] V. Vakiloroaya, Q. Ha, and M. Skibniewski, "Modeling and experimental validation of a solar-assisted direct expansion air conditioning system," *Energy and Buildings*, vol. 66, pp. 524–536, Nov. 2013.

[43] A. H. H. Ali, P. Noeres, and C. Pollerberg, "Performance assessment of an integrated free cooling and solar powered single-effect lithium bromide-water absorption chiller," *Solar Energy*, vol. 82, pp. 1021–1030, Nov. 2008.

[44] A. Pongtornkulpanich, S. Thepa, M. Amornkitbamrung, and C. Butcher, "Experience with fully operational solar-driven 10-ton LiBr/H2O single-effect absorption cooling system in Thailand," *Renewable Energy*, vol. 33, pp. 943–949, May 2008.

[45] F. Agyenim, I. Knight, and M. Rhodes, "Design and experimental testing of the performance of an outdoor LiBr/H2O solar thermal absorption cooling system with a cold store," *Solar Energy*, vol. 84, pp. 735–744, May 2010.

[46] M. Ortiz, H. Barsun, H. He, P. Vorobieff, and A. Mammoli, "Modeling of a solar-assisted HVAC system with thermal storage," *Energy and Buildings*, vol. 42, pp. 500–509, Apr. 2010.

[47] A. Mammoli, P. Vorobieff, H. Barsun, R. Burnett, and D. Fisher, "Energetic,

economic and environmental performance of a solar-thermal-assisted HVAC system," *Energy and Buildings*, vol. 42, pp. 1524–1535, Sept. 2010.

[48] M. C. R. Hidalgo, P. R. Aumente, M. I. Millán, A. L. Neumann, and R. S. Mangual, "Energy and carbon emission savings in Spanish housing air-conditioning using solar driven absorption system," *Applied Thermal Engineering*, vol. 28, pp. 1734–1744, Oct. 2008.

[49] S. Rosiek and F. J. Batlles, "Integration of the solar thermal energy in the construction: Analysis of the solar-assisted air-conditioning system installed in CIESOL building," *Renewable Energy*, vol. 34, pp. 1423–1431, June 2009.

[50] O. Marc, F. Lucas, F. Sinama, and E. Monceyron, "Experimental investigation of a solar cooling absorption system operating without any backup system under tropical climate," *Energy and Buildings*, vol. 42, pp. 774–782, June 2010.

[51] A. Mueller, M. Orosz, A. K. Narasimhan, R. Kamal, H. F. Hemond, and Y. Goswami, "Evolution and feasibility of decentralized concentrating solar thermal power systems for modern energy access in rural areas," *MRS Energy & Sustainability*, vol. 3, 2016.

[52] A. Giovannelli, "State of the art on small-scale concentrated solar power plants," *Energy Procedia*, vol. 82, pp. 607–614, 2015.

[53] O. A. Oyewunmi, C. J. Kirmse, A. M. Pantaleo, and C. N. Markides, "Performance of working-fluid mixtures in orc-chp systems for different heat-demand

segments and heat-recovery temperature levels," *Energy Conversion and Management*, vol. 148, pp. 1508–1524, 2017.

[54] A. Ramos, M. A. Chatzopoulou, J. Freeman, and C. N. Markides, "Optimisation of a high-efficiency solar-driven organic Rankine cycle for applications in the built environment," *Applied energy*, vol. 228, pp. 755–765, 2018.

[55] H. Luo, R. Wang, and Y. Dai, "The effects of operation parameter on the performance of a solar-powered adsorption chiller," *Applied Energy*, vol. 87, no. 10, pp. 3018 – 3022, 2010.

[56] Y. M. Kim, D. G. Shin, C. G. Kim, and G. B. Cho, "Single-loop organic Rankine cycles for engine waste heat recovery using both low and high-temperature heat sources," *Energy*, vol. 96, pp. 482–494, Feb. 2016.

[57] F. Chiara and M. Canova, "A review of energy consumption, management, and recovery in automotive systems, with considerations of future trends," *Proceedings of the Institution of Mechanical Engineers, Part D: Journal of Automobile Engineering*, vol. 227, pp. 914–936, June 2013.

[58] M. Jiménez-Arreola, C. Wieland, and A. Romagnoli, "Direct vs indirect evaporation in Organic Rankine Cycle (ORC) systems: A comparison of the dynamic behavior for waste heat recovery of engine exhaust," *Applied Energy*, vol. 242, pp. 439–452, May 2019.

[59] G. Shu, J. Zhao, H. Tian, X. Liang, and H. Wei, "Parametric and exergetic

analysis of waste heat recovery system based on thermoelectric generator and organic rankine cycle utilizing R123," *Energy*, vol. 45, pp. 806–816, Sept. 2012.

[60] G. Shu, Y. Liang, H. Wei, H. Tian, J. Zhao, and L. Liu, "A review of waste heat recovery on two-stroke IC engine aboard ships," *Renewable and Sustainable Energy Reviews*, vol. 19, pp. 385–401, Mar. 2013.

[61] S. Kouro, P. Cortés, R. Vargas, U. Ammann, and J. Rodríguez, "Model predictive control—a simple and powerful method to control power converters," *IEEE Transactions on industrial electronics*, vol. 56, no. 6, pp. 1826–1838, 2008.

[62] M. A. Velasquez, J. Barreiro-Gomez, N. Quijano, A. I. Cadena, and M. Shahidehpour, "Distributed model predictive control for economic dispatch of power systems with high penetration of renewable energy resources," *International Journal of Electrical Power & Energy Systems*, vol. 113, pp. 607–617, 2019.

[63] H. J. Ferreau, H. G. Bock, and M. Diehl, "An online active set strategy to overcome the limitations of explicit MPC," *International Journal of Robust and Nonlinear Control: IFAC-Affiliated Journal*, vol. 18, no. 8, pp. 816–830, 2008.

[64] Y. Xie, R. Ghaemi, J. Sun, and J. S. Freudenberg, "Implicit model predictive control of a full bridge DC–DC converter," *IEEE Transactions on Power Electronics*, vol. 24, no. 12, pp. 2704–2713, 2009.

[65] R. Quirynen, S. Gros, and M. Diehl, "Inexact Newton based lifted implicit integrators for fast nonlinear MPC," *IFAC-PapersOnLine*, vol. 48, no. 23, pp. 32–38, 2015.

[66] B. Pluymers, J. Rossiter, J. Suykens, and B. De Moor, "A simple algorithm for robust MPC," *IFAC Proceedings Volumes*, vol. 38, no. 1, pp. 257–262, 2005.

[67] S. Di Cairano, D. Bernardini, A. Bemporad, and I. V. Kolmanovsky, "Stochastic MPC with learning for driver-predictive vehicle control and its application to HEV energy management," *IEEE Transactions on Control Systems Technology*, vol. 22, no. 3, pp. 1018–1031, 2013.

[68] G. Pannocchia, M. Gabiccini, and A. Artoni, "Offset-free MPC explained: novelties, subtleties, and applications," *IFAC-PapersOnLine*, vol. 48, no. 23, pp. 342–351, 2015.

[69] V. Adetola and M. Guay, "Robust adaptive MPC for constrained uncertain nonlinear systems," *International Journal of Adaptive Control and Signal Processing*, vol. 25, no. 2, pp. 155–167, 2011.

[70] J. Vada, O. Slupphaug, T. A. Johansen, and B. A. Foss, "Linear MPC with optimal prioritized infeasibility handling: application, computational issues and stability," *Automatica*, vol. 37, no. 11, pp. 1835–1843, 2001.

[71] H. Van Essen and H. Nijmeijer, "Non-linear model predictive control for constrained mobile robots," in *European Control Conference (ECC)*, pp. 1157–1162, IEEE, 2001.

[72] G.-Y. Zhu and M. A. Henson, "Model predictive control of interconnected linear and nonlinear processes," *Industrial & engineering chemistry research*, vol. 41, no. 4, pp. 801–816, 2002.

[73] A. N. Venkat, J. B. Rawlings, and S. J. Wright, "Plant-wide optimal control with decentralized MPC," *IFAC Proceedings Volumes*, vol. 37, no. 9, pp. 589–594, 2004.

[74] F. Kennel, D. Görges, and S. Liu, "Energy management for smart grids with electric vehicles based on hierarchical MPC," *IEEE Transactions on industrial informatics*, vol. 9, no. 3, pp. 1528–1537, 2012.

[75] V. Chandan and A. G. Alleyne, "Decentralized predictive thermal control for buildings," *Journal of Process Control*, vol. 24, no. 6, pp. 820–835, 2014.

[76] M. Maasoumy and A. Sangiovanni-Vincentelli, "Total and peak energy consumption minimization of building HVAC systems using model predictive control," *IEEE Design Test of Computers*, vol. 29, no. 4, pp. 26–35, 2012.

[77] M. S. Elliott and B. P. Rasmussen, "Model-based predictive control of a multi-evaporator vapor compression cooling cycle," pp. 1463–1468, 2008 American Control Conference (ACC), 2008.

[78] B. Mu, Y. Li, T. I. Salsbury, and J. M. House, "Extremum seeking based control strategy for a chilled-water plant with parallel chillers," ASME 2015 Dynamic Systems and Control Conference, 2015.

[79] C. Sun, F. Sun, and S. J. Moura, "Data enabled predictive energy management of a PV-battery smart home nanogrid," pp. 1023–1028, 2015 American Control Conference (ACC), 2015.

[80] K. C. Wong, C. E. Whitney, A. Bemporad, and D. Bernardini, "System and method for managing the period of a control loop for controlling an engine using model predictive control," 2016. US Patent No. 9,435,274.

[81] M. He, X. Zhang, K. Zeng, and K. Gao, "A combined thermodynamic cycle used for waste heat recovery of internal combustion engine," *Energy*, vol. 36, no. 12, pp. 6821–6829, 2011.

[82] M. Huang, K. Zaseck, K. Butts, and I. Kolmanovsky, "Rate-based model predictive controller for diesel engine air path: Design and experimental evaluation," *IEEE Transactions on Control Systems Technology*, vol. 24, no. 6, pp. 1922–1935, 2016.

[83] D. Zhao, C. Liu, R. Stobart, J. Deng, E. Winward, and G. Dong, "An explicit model predictive control framework for turbocharged diesel engines," *IEEE Transactions on Industrial Electronics*, vol. 61, no. 7, pp. 3540–3552, 2014.

[84] A. Solouk and M. Shahbakhti, "Energy optimization and fuel economy investigation of a series hybrid electric vehicle integrated with diesel/RCCI engines," *Energies*, vol. 9, no. 12, 23 pages, 2016.

[85] R. D. Robinett III and D. G. Wilson, *Nonlinear Power Flow Control Design: Utilizing Exergy, Entropy, Static and Dynamic Stability, and Lyapunov Analysis*, ch. 2 Thermodynamics. Springer Science & Business Media, 2011.

[86] M. Razmara, M. Bidarvatan, M. Shahbakhti, and R. Robinett, "Innovative Exergy-Based Combustion Phasing Control of IC Engines," SAE Technical Paper 2016-01-0815, SAE 2016 World Congress and Exhibition, 2016.

[87] A. Yildiz and A. Güngör, "Energy and exergy analyses of space heating in buildings," *Applied Energy*, vol. 86, no. 10, pp. 1939–1948, 2009.

[88] F. Zabihian, "Educating undergraduate mechanical engineering students about exergy analysis," in *ASEE Annual Conference & Exposition*, pp. 26–570, 2015.

[89] US Energy Information Administration, "International energy outlook 2018," Available at *https://www.eia.gov/outlooks/aeo/pdf/AEO2018.pdf* (Accessed on 19 April 2019).

[90] J. M. Rodríguez, D. Sánchez, G. S. Martínez, E. G. Bennouna, and B. Ikken, "Techno-economic assessment of thermal energy storage solutions for a 1 MWe CSP-ORC power plant," *Solar Energy*, vol. 140, pp. 206–218, 2016.

[91] Q. Li, C. Zheng, A. Shirazi, O. B. Mousa, F. Moscia, J. A. Scott, and R. A. Taylor, "Design and analysis of a medium-temperature, concentrated solar thermal collector for air-conditioning applications," *Applied Energy*, vol. 190, pp. 1159–1173, 2017.

[92] G. Bruni, S. Cordiner, V. Mulone, V. Rocco, and F. Spagnolo, "A study on the energy management in domestic micro-grids based on model predictive control strategies," *Energy Conversion and Management*, vol. 102, pp. 50–58, 2015.

[93] G. Huang, S. Wang, and X. Xu, "A robust model predictive control strategy for improving the control performance of air-conditioning systems," *Energy Conversion and Management*, vol. 50, no. 10, pp. 2650–2658, 2009.

[94] Enogia SAS, "Datasheet: Enogia'S ENO-10LT ORC System Fact Sheet," 2017. Available at *http://www.enogia.com/images/offer/datasheet-ENO10LT.pdf* (Accessed on 14 April 2019).

[95] Soltigua, "Soltigua - Parabolic Troughs PTMx." Available at *http://www.soltigua.com/ptmx-introduction/* (Accessed on 17 Apr. 2019).

[96] M. Shahidehpour, H. Yamin, and Z. Li, *Market Operations in Electric Power Systems: Forecasting, Scheduling and Risk Management.* Wiley Online Library, 2002.

[97] F. Burkholder and C. Kutscher, "Heat loss testing of Schott's 2008 PTR70

parabolic trough receiver." Technical Report of National Renewable Energy Lab. (NREL), Golden, CO (United States), 2009.

[98] Agenzia Nazionale per le Nuove tecnologie, l'Energia e lo Sviluppo economico sostenibile (ENEA), "Performance test report summary according to EN 12975-2:2006." Technical communication with SOLTIGUA. (Accessed on 22 March 2017).

[99] J. Drouineau. Technical communication with ENOGIA. (Accessed on 28 August 2017).

[100] M. Razmara, M. Maasoumy, M. Shahbakhti, and R. Robinett III, "Optimal exergy control of building HVAC system," *Applied energy*, vol. 156, pp. 555–565, 2015.

[101] M. Maasoumy, M. Razmara, M. Shahbakhti, and A. Sangiovanni-Vincentelli, "Selecting Building Predictive Control Based on Model Uncertainty," 2014 American Control Conference (ACC), 2014.

[102] M. Razmara, G. R. Bharati, M. Shahbakhti, S. Paudyal, and R. D. Robinett, "Bilevel optimization framework for smart building-to-grid systems," *IEEE Transactions on Smart Grid*, vol. 9, pp. 582–593, March 2018.

[103] Y. A. Cengel and M. A. Boles, *Thermodynamics: An Engineering Approach*, ch. 12. McGraw Hill, 5th ed., 2006.

[104] American Society of Heating, Refrigerating and Air-Conditioning Engineers, "ANSI/ASHRAE STANDARD 62.1-2007." Available at *https://www.ashrae.org/File%20Library/Technical%20Resources/ Standards%20and%20Guidelines/Standards%20Intepretations/IC_ 62-1-2007-1.pdf* (Accessed on 9 January 2019).

[105] Air-Conditioning, Heating and Refrigeration Institute, "2014 standard for performance rating of air-to-air exchangers for energy recovery ventilation equipment." Available at *http://www.ahrinet.org/App_Content/ahri/ files/STANDARDS/ANSI/ANSI_AHRI_Standard_1060_I-P_2014.pdf* (Accessed on 9 January 2019).

[106] MISO, "Midcontinent independent system operator." Available at *https:// www.misoenergy.org/MarketsOperations/Prices/Pages/Prices.aspx* (Accessed on 18 September 2018).

[107] J. Lofberg, "YALMIP: A Toolbox for Modeling and Optimization in MATLAB," pp. 284–289, IEEE International Symposium on Computer Aided Control Systems Design, 2004.

[108] A. Wächter and L. T. Biegler, "On the implementation of an interior-point filter line-search algorithm for large-scale nonlinear programming," *Mathematical Programming*, vol. 106, no. 1, pp. 25–57, 2006.

[109] Gurobi, "Gurobi Optimizer Reference Manual." Available at *https:*

//www.gurobi.com/wp-content/plugins/hd_documentations/ documentation/9.0/refman.pdf (Accessed on 5 March 2019).

[110] Intellovations, LLC., "Weather forecast accuracy details for Hancock, Michigan." Available at http://forecastadvisor.com/detail/Michigan/ Houghton/49931/ (Accessed on 26 May 2018).

[111] M. Shahidehpour, H. Yamin, and Z. Li, *Market operations in electric power systems: forecasting, scheduling, and risk management.* John Wiley & Sons, 2003.

[112] F. Wang, Z. Mi, S. Su, and H. Zhao, "Short-term solar irradiance forecasting model based on artificial neural network using statistical feature parameters," *Energies*, vol. 5, no. 5, pp. 1355–1370, 2012.

[113] M. Maasoumy, M. Razmara, M. Shahbakhti, and A. S. Vincentelli, "Handling model uncertainty in model predictive control for energy efficient buildings," *Energy and Buildings*, vol. 77, pp. 377–392, 2014.

[114] NREL, "NSRDB Data Viewer." (Accessed on 9 Mar. 2019). [Online]. Available: https://maps.nrel.gov/nsrdb-viewer/.

[115] X. Wang, G. Shu, H. Tian, P. Liu, X. Li, and D. Jing, "Dynamic Response Performance Comparison of Ranking Cycles with Different Working Fluids for Waste Heat Recovery of Internal Combustion Engines," *Energy Procedia*, vol. 105, pp. 1600–1605, May 2017.

[116] X. Wang, H. Tian, and G. Shu, "Part-Load Performance Prediction and Operation Strategy Design of Organic Rankine Cycles with a Medium Cycle Used for Recovering Waste Heat from Gaseous Fuel Engines," *Energies*, vol. 9, p. 527, July 2016.

[117] R. Shi, T. He, J. Peng, Y. Zhang, and W. Zhuge, "System design and control for waste heat recovery of automotive engines based on Organic Rankine Cycle," *Energy*, vol. 102, pp. 276–286, May 2016.

[118] L. Shi, G. Shu, H. Tian, and S. Deng, "A review of modified Organic Rankine cycles (ORCs) for internal combustion engine waste heat recovery (ICE-WHR)," *Renewable and Sustainable Energy Reviews*, vol. 92, pp. 95–110, Sept. 2018.

[119] S. Zou, W. Huang, L. Wang, X. Yan, and K. Wang, "Performance Analysis of an Organic Rankine Cycle with Different Working Fluids for Heat Recovery from an Internal Combustion Engine," pp. 1–9, 2018 2nd IEEE Conference on Energy Internet and Energy System Integration (EI2).

[120] S. Seyedkavoosi, S. Javan, and K. Kota, "Exergy-based optimization of an organic rankine cycle (orc) for waste heat recovery from an internal combustion engine (ice)," *Applied Thermal Engineering*, vol. 126, pp. 447–457, 2017.

[121] G. Valencia, A. Fontalvo, Y. Cárdenas, J. Duarte, and C. Isaza, "Energy and exergy analysis of different exhaust waste heat recovery systems for natural gas engine based on orc," *Energies*, vol. 12, no. 12, p. 2378, 2019.

[122] A. Naeimi, M. Bidi, M. H. Ahmadi, R. Kumar, M. Sadeghzadeh, and M. A. Nazari, "Design and exergy analysis of waste heat recovery system and gas engine for power generation in tehran cement factory," *Thermal Science and Engineering Progress*, vol. 9, pp. 299–307, 2019.

[123] J. Jannatkhah, B. Najafi, and H. Ghaebi, "Energy and exergy analysis of combined orc–erc system for biodiesel-fed diesel engine waste heat recovery," *Energy Conversion and Management*, vol. 209, p. 112658, 2020.

[124] B. Xu, D. Rathod, A. Yebi, and Z. Filipi, "A comparative analysis of real-time power optimization for organic Rankine cycle waste heat recovery systems," *Applied Thermal Engineering*, vol. 164, p. 114442, Jan. 2020.

[125] F. Yang, H. Cho, H. Zhang, J. Zhang, and Y. Wu, "Artificial neural network (ANN) based prediction and optimization of an organic Rankine cycle (ORC) for diesel engine waste heat recovery," *Energy Conversion and Management*, vol. 164, pp. 15–26, May 2018.

[126] R. Scaccabarozzi, M. Tavano, C. M. Invernizzi, and E. Martelli, "Comparison of working fluids and cycle optimization for heat recovery ORCs from large internal combustion engines," *Energy*, vol. 158, pp. 396–416, Sept. 2018.

[127] J. Peralez, M. Nadri, P. Dufour, P. Tona, and A. Sciarretta, "Organic Rankine Cycle for Vehicles: Control Design and Experimental Results," *IEEE Transactions on Control Systems Technology*, vol. 25, pp. 952–965, May 2017.

[128] J. Song, X. Li, K. Wang, and C. N. Markides, "Parametric optimisation of a combined supercritical CO2 (S-CO2) cycle and organic Rankine cycle (ORC) system for internal combustion engine (ICE) waste-heat recovery," *Energy Conversion and Management*, vol. 218, p. 112999, Aug. 2020.

[129] B. Xu, D. Rathod, S. Kulkarni, A. Yebi, Z. Filipi, S. Onori, and M. Hoffman, "Transient dynamic modeling and validation of an organic Rankine cycle waste heat recovery system for heavy duty diesel engine applications," *Applied Energy*, vol. 205, pp. 260–279, 2017.

[130] D. Luong and T.-C. Tsao, "Linear Quadratic Integral control of an Organic Rankine Cycle for waste heat recovery in heavy-duty diesel powertrain," pp. 3147–3152, 2014 American Control Conference, IEEE.

[131] G. Hou, S. Bi, M. Lin, J. Zhang, and J. Xu, "Minimum variance control of organic Rankine cycle based waste heat recovery," *Energy Conversion and Management*, vol. 86, pp. 576–586, Oct. 2014.

[132] E. Feru, F. Willems, B. de Jager, and M. Steinbuch, "Modeling and Control of a Parallel Waste Heat Recovery System for Euro-VI Heavy-Duty Diesel Engines," *Energies*, vol. 7, pp. 6571–6592, Oct. 2014.

[133] J. Peralez, P. Tona, M. Nadri, P. Dufour, and A. Sciarretta, "Optimal control for an organic rankine cycle on board a diesel-electric railcar," *Journal of Process Control*, vol. 33, pp. 1–13, Sept. 2015.

[134] R. Zhao, H. Zhang, S. Song, Y. Tian, Y. Yang, and Y. Liu, "Integrated simulation and control strategy of the diesel engine–organic Rankine cycle (ORC) combined system," *Energy Conversion and Management*, vol. 156, pp. 639–654, Jan. 2018.

[135] F. Payri, J. Luján, C. Guardiola, and B. Pla, "A Challenging Future for the IC Engine: New Technologies and the Control Role," *Oil & Gas Science and Technology – Revue d'IFP Energies nouvelles*, vol. 70, no. 1, pp. 15–30, 2015.

[136] J. Zhang, Y. Zhou, S. Gao, and G. Hou, "Constrained predictive control based on state space model of Organic Rankine Cycle system for waste heat recovery," pp. 230–234, 2012 24th Chinese Control and Decision Conference (CCDC).

[137] Yebi A, Xu B, Liu X, Shutty J, Anschel P, Filipi Z, Onori S, Hoffman M, "Estimation and Predictive Control of a Parallel Evaporator Diesel Engine Waste Heat Recovery System," *IEEE Transactions on Control Systems Technology*, vol. 27, pp. 282–295, Jan. 2019.

[138] M. C. Esposito, N. Pompini, A. Gambarotta, V. Chandrasekaran, J. Zhou, and M. Canova, "Nonlinear Model Predictive Control of an Organic Rankine Cycle for Exhaust Waste Heat Recovery in Automotive Engines," *IFAC-PapersOnLine*, vol. 48, no. 15, pp. 411–418, 2015.

[139] P. Petr, C. Schröder, J. Köhler, and M. Gräber, "Optimal Control of Waste Heat Recovery Systems Applying Nonlinear Model Predictive Control (NMPC),"

pp. 12–14, Proceedings of the 3rd Seminar on ORC Systems, Brussels, Belgium, 2015.

[140] B. Zhu, H. Tazvinga, and X. Xia, "Switched Model Predictive Control for Energy Dispatching of a Photovoltaic-Diesel-Battery Hybrid Power System," *IEEE Transactions on Control Systems Technology*, vol. 23, no. 3, pp. 1229–1236, 2015.

[141] A. Raut, B. Irdmousa, and M. Shahbakhti, "Dynamic modeling and model predictive control of an RCCI engine," *Control Engineering Practice*, vol. 81, pp. 129–144, Dec. 2018.

[142] M. Razmara, M. Bidarvatan, M. Shahbakhti, and R. Robinett III, "Optimal exergy-based control of internal combustion engines," *Applied energy*, vol. 183, pp. 1389–1403, 2016.

[143] H. Teng, J. Klaver, T. Park, G. L. Hunter, and B. van der Velde, "A Rankine Cycle System for Recovering Waste Heat from HD Diesel Engines - WHR System Development," SAE Technical Paper No. 2011–01–0311, Apr. 2011.

[144] T. Park, H. Teng, G. L. Hunter, B. van der Velde, and J. Klaver, "A Rankine Cycle System for Recovering Waste Heat from HD Diesel Engines - Experimental Results," SAE Technical Paper No. 2011–01–1337, Apr. 2011.

[145] B. Sayin Kul and A. Kahraman, "Energy and exergy analyses of a diesel engine

186

fuelled with biodiesel-diesel blends containing 5% bioethanol," *Entropy*, vol. 18, no. 11, 18 pages, 2016.

[146] F-Chart Software, LLC, "Engineering Equation Solver." Available at *https: // fchartsoftware. com/ ees/* (Accessed on 19 April 2021).

[147] S. Ye, Y. H. Yap, S. T. Kolaczkowski, K. Robinson, and D. Lukyanov, "Catalyst 'light-off' experiments on a diesel oxidation catalyst connected to a diesel engine—Methodology and techniques," *Chemical Engineering Research and Design*, vol. 90, pp. 834–845, June 2012.

[148] Z. Meng, C. Chen, J. Li, J. Fang, J. Tan, Y. Qin, Y. Jiang, Z. Qin, W. Bai, and K. Liang, "Particle emission characteristics of DPF regeneration from DPF regeneration bench and diesel engine bench measurements," *Fuel*, vol. 262, p. 116589, Feb. 2020.

[149] C. Ruehl, J. D. Smith, Y. Ma, J. E. Shields, M. Burnitzki, W. Sobieralski, R. Ianni, D. J. Chernich, M.-C. O. Chang, and J. F. Collins, "Emissions During and Real-World Frequency of Heavy-Duty Diesel Particulate Filter Regeneration," *Environmental science & technology*, vol. 52, no. 10, pp. 5868–5874, 2018.

[150] D. J. Worth, M. E. Stettler, P. Dickinson, K. Hegarty, and A. M. Boies, "Characterization and evaluation of methane oxidation catalysts for dual-fuel diesel

and natural gas engines," *Emission Control Science and Technology*, vol. 2, no. 4, pp. 204–214, 2016.

[151] M. Toub, M. Shahbakhti, R. D. Robinett, and G. Aniba, "MPC-trained ANFIS for Control of MicroCSP Integrated into a Building HVAC System," in *2019 American Control Conference (ACC)*, pp. 241–246, IEEE, 2019.

[152] E. Essien, H. Ibrahim, M. Mehrandezh, and R. Idem, "Adaptive neuro-fuzzy inference system (ANFIS)–based model predictive control (MPC) for carbon dioxide reforming of methane (CDRM) in a plug flow tubular reactor for hydrogen production," *Thermal Science and Engineering Progress*, vol. 9, pp. 148–161, 2019.

[153] G. Williams, N. Wagener, B. Goldfain, P. Drews, J. M. Rehg, B. Boots, and E. A. Theodorou, "Information theoretic MPC for model-based reinforcement learning," in *2017 IEEE International Conference on Robotics and Automation (ICRA)*, pp. 1714–1721, IEEE, 2017.

[154] S. Gros and M. Zanon, "Reinforcement learning for mixed-integer problems based on MPC," *IFAC-PapersOnLine*, vol. 53, no. 2, pp. 5219–5224, 2020.

[155] A. Reske, J. Carius, Y. Ma, F. Farshidian, and M. Hutter, "Imitation learning from MPC for quadrupedal multi-gait control," in *2021 IEEE International Conference on Robotics and Automation (ICRA)*, pp. 5014–5020, IEEE, 2021.

[156] M. Novak and F. Blaabjerg, "Supervised imitation learning of FS-MPC algorithm for multilevel converters," in *2021 23rd European Conference on Power Electronics and Applications (EPE'21 ECCE Europe)*, IEEE, 2021.

[157] Engineering ToolBox, "Fuels – Higher and Lower Calorific Values." Available at *https://www.engineeringtoolbox.com/ fuels-higher-calorific-values-d_169.html* (Accessed on 19 September 2021).

[158] Engineering ToolBox, "Air – Specific Heat at Constant Pressure and Varying Temperature." Available at *https://www.engineeringtoolbox.com/ air-specific-heat-capacity-d_705.html* (Accessed on 19 September 2021).

[159] Y. A. Cengel, *Heat Transfer: A Practical Approach*, ch. 13. Mcgraw-Hill, 2002.

Appendix A

Details of the Energy Balance in

Fig. 3.17

The fuel energy (E_{Fuel}) is calculated as:

$$E_{Fuel} = m_{Fuel} \cdot (DSR \cdot HV_{NG} + (1 - DSR) \cdot HV_{Diesel}) \qquad \text{(A.1)}$$

where, m_{Fuel} is the fuel consumed by the ICE; DSR is the diesel substitution ratio; and HV_{NG} and HV_{Diesel} are heating values of natural gas and diesel fuel, respectively.

The mechanical energies from the ICE (E_{Mech}^{ICE}) and WHR (E_{Mech}^{WHR}) are calculated by:

$$E_{Mech}^{ICE} = \omega_{ICE} \cdot Tq_{ICE} \cdot t \qquad (A.2a)$$

$$E_{Mech}^{WHR} = \omega_{ORC} \cdot Tq_{ORC} \cdot t \qquad (A.2b)$$

where, ω_{ICE} and ω_{ORC} are the angular speeds of the ICE and ORC, respectively; Tq_{ICE} and Tq_{ORC} are the torques produced by the ICE and ORC, respectively; and t is the time. Additionally, the mechanical energy out of the gear box (E_{Mech}) and the electrical energy out of the generator (E_{Elec}) is calculated by:

$$E_{Mech} = \eta_{GB} \cdot (E_{Mech}^{ICE} + E_{Mech}^{WHR}) \qquad (A.3a)$$

$$E_{Elec} = \eta_{Gen} \cdot E_{Mech} \qquad (A.3b)$$

The thermal energy from the exhaust ($E_{exh}^{WHR,in}$) is obtained using:

$$E_{exh}^{WHR,in} = m_{exh} \cdot c_p \cdot T_{exh}^{WHR,in} \qquad (A.4)$$

where, m_{exh} is the mass of exhaust gases of the ICE; c_p is the specific heat at constant pressure of the exhaust gases; and $T_{exh}^{WHR,in}$ is the temperature of the exhaust gas

before the WHR system. Furthermore, m_{exh} is calculated using m_{Fuel} and the air-fuel ratio (AFR) of the ICE is:

$$m_{exh} = (AFR + 1) \cdot m_{Fuel} \tag{A.5}$$

The values used for the constants and variables in Equations A.1-A.5 are tabulated in Table A.1.

Table A.1
Values of the constants and variables used in Equations A.1-A.5.

Constants	Heating value of natural gas (HV_{NG}) [157]		45.3	MJ/kg
	Heating value of diesel (HV_{Diesel}) [157]		43	MJ/kg
	ICE angular speed (ω_{ICE})		40π	rad/s
	ORC angular speed (ω_{ORC})		40π	rad/s
	Time (t)		3	h
	Specific heat at constant pressure of exhaust gases (c_p) [158] [Assuming exhaust gas has the same properties as air]		1.03	kJ/kg.K
	Air-fuel ratio (AFR)		15	-
	Gear box efficiency (η_{GB})		0.98	-
	Generator efficiency (η_{Gen})		0.9	-
Variables	Average diesel substitution ratio (DSR)	RBC for ICE	90	%
		RBC for ICE+WHR	90	%
		MPC for ICE+WHR	95	%
	Average torque from ICE (Tq_{ICE})	RBC for ICE	619	Nm
		RBC for ICE+WHR	598	Nm
		MPC for ICE+WHR	601	Nm
	Average torque from ORC (Tq_{ORC})	RBC for ICE	-	Nm
		RBC for ICE+WHR	27.3	Nm
		MPC for ICE+WHR	33.6	Nm
	Average temperature of the exhaust gas before WHR ($T_{exh}^{WHR,in}$)	RBC for ICE	871	K
		RBC for ICE+WHR	870	K
		MPC for ICE+WHR	877	K
	Mass of the consumed fuel by the ICE (m_{Fuel})	RBC for ICE	44.8	kg
		RBC for ICE+WHR	43.2	kg
		MPC for ICE+WHR	42	kg

Appendix B

Details of the Energy and Exergy Balance in Fig. 3.24

The input fuel energy is assumed to be pure exergy. The fuel exergy (X_{Fuel}) is calculated as:

$$X_{Fuel} = m_{Fuel} \cdot (K_{NG} \cdot DSR \cdot HV_{NG} + K_{Diesel} \cdot (1 - DSR) \cdot HV_{Diesel}) \qquad \text{(B.1)}$$

where, m_{Fuel} is the fuel consumed by the ICE; DSR is the diesel substitution ratio; HV_{NG} and HV_{Diesel} are heating values of natural gas and diesel fuel, respectively; and K_{Diesel} and K_{NG} are the chemical exergy factors of diesel and natural gas fuels, respectively.

The output mechanical energy (i.e., work delivery) is assumed to be pure exergy. The mechanical exergy (X_{Mech}^{System}) from the combined ICE and WHR system is calculated by:

$$X_{Mech}^{System} = \eta_{GB} \cdot \omega_{System} \cdot (Tq_{ICE} + Tq_{ORC}) \cdot t \tag{B.2}$$

where, η_{GB} is the efficiency of the gear box; ω_{System} is the angular speed of the system; Tq_{ICE} and Tq_{ORC} are the torques produced by the ICE and ORC, respectively; and t is the time. The heat lost in the ICE (Q_{HL}^{ICE}) is calculated as:

$$Q_{HL}^{ICE} = h_{he} \cdot A_{he} \cdot (T_{Wall}^{ICE} - T_{amb}) \cdot t \tag{B.3}$$

where, h_{he} is the heat transfer coefficient between the ICE wall and the ambient air; A_{he} is the heat transfer area between the ICE wall and the ambient air; T_{Wall}^{ICE} is the wall temperature of the ICE; and T_{amb} is the ambient air temperature; The thermal energy of the exhaust gas before $(E_{exh}^{WHR,in})$ and after $(E_{exh}^{WHR,out})$ the WHR system is obtained using:

$$E_{exh}^{WHR,in} = m_{exh} \cdot c_p \cdot T_{exh}^{WHR,in} \tag{B.4a}$$

$$E_{exh}^{WHR,out} = m_{exh} \cdot c_p \cdot T_{exh}^{WHR,out} \tag{B.4b}$$

where, m_{exh} is the mass of exhaust gases of the ICE; $T_{exh}^{WHR,in}$ and $T_{exh}^{WHR,out}$ are the

temperatures of the exhaust gas before and after the WHR system, respectively; and

c_p is the specific heat at constant pressure of the exhaust gases. The thermal exergy of

the exhaust gas before $(X_{exh}^{WHR,in})$ and after $(X_{exh}^{WHR,out})$ the WHR system is obtained

using:

$$X_{exh}^{WHR,in} = m_{exh} \cdot [(h_{WHR,in} - h_{amb}) + T_{amb} \cdot (s_{WHR,in} - s_{amb})] \qquad \text{(B.5a)}$$

$$X_{exh}^{WHR,out} = m_{exh} \cdot [(h_{WHR,out} - h_{amb}) + T_{amb} \cdot (s_{WHR,out} - s_{amb})] \qquad \text{(B.5b)}$$

where, T_{amb} is the ambient air temperature; $h_{WHR,in}$ and $s_{WHR,in}$ are the specific

enthalpy and the specific entropy of the exhaust gas before the WHR system, respec-

tively; $h_{WHR,out}$ and $s_{WHR,out}$ are the specific enthalpy and the specific entropy of the

exhaust gas after the WHR system, respectively; and h_{amb} and s_{amb} are the specific

enthalpy and the specific entropy of the ambient air, respectively.

The exergy destructions in the TC (X_{Dest}^{TC}), HE (X_{Dest}^{HE}), and ORC (X_{Dest}^{ORC}) are given

by Eqs. (B.6a), (B.6b) and (B.6c), respectively as shown below:

$$X_{Dest}^{TC} = T_{amb} \cdot (m_{int} \cdot (s_{int}^{c,out} - s_{int}^{c,in}) + m_{exh} \cdot (s_{exh}^{tb,out} - s_{exh}^{tb,in})) \qquad \text{(B.6a)}$$

$$X_{Dest}^{HE} = T_{amb} \cdot m_{exh} \cdot (s_{exh}^{WHR,out} - s_{exh}^{WHR,in}) \qquad \text{(B.6b)}$$

$$X_{Dest}^{ORC} = T_{amb} \cdot (\frac{Q_{Lost}}{T_{con,m}} - \frac{Q_{ORC}}{T_{ev,m}}) \qquad \text{(B.6c)}$$

where, m_{int} is the mass of the intake air; $s_{int}^{c,in}$ and $s_{int}^{c,out}$ are the specific entropies of the

intake air entering and leaving the compressor of the TC, respectively; $s_{exh}^{tb,in}$ and $s_{exh}^{tb,out}$ are the specific entropies of the exhaust gas entering and leaving the turbine of the TC, respectively; $s_{exh}^{WHR,in}$ and $s_{exh}^{WHR,out}$ are the specific entropies of the exhaust gas entering and leaving the HE, respectively; Q_{Lost} and Q_{ORC} are the heat transferred from the condersor of the ORC to the ambient and the heat input from the exhaust gas to the ORC, respectively; and $T_{ev,m}$ and $T_{con,m}$ are the arithmetic mean temperatures of the evaporator and condenser of the ORC, respectively.

The specific enthalpy (h_x) and the specific entropy (s_x) for the fluid at state "x" is calculated as a function of the Temperature (T_x) and pressure (p_x) of the fluid at state "x" as shown below.

$$h_x = f(T_x, p_x) \tag{B.7a}$$

$$s_x = g(T_x, p_x) \tag{B.7b}$$

It is worth noting that, the intake air and exhaust gas are assumed to behave as an ideal gas. Finally, m_{int} and m_{exh} are calculated using m_{Fuel} and the air-fuel ratio (AFR) of the ICE:

$$m_{int} = (AFR) \cdot m_{Fuel} \tag{B.8a}$$

$$m_{exh} = (AFR + 1) \cdot m_{Fuel} \tag{B.8b}$$

The values used for the constants and variables in Equations B.1-B.8 are tabulated in Table B.1.

Table B.1

Values of the constants and variables used in Equations B.1-B.8.

Constants	Heating value of natural gas (HV_{NG}) [157]	45.3	MJ/kg
	Heating value of diesel (HV_{Diesel}) [157]	43	MJ/kg
	Exergy factor of natural gas (K_{NG})	1.09	-
	Exergy factor of diesel (K_{Diesel})	1.07	-
	System angular speed (ω_{System})	40π	rad/s
	Heat transfer coefficient between ICE wall and ambient air (h_{he}) [159]	190	W/m^2.K
	Heat transfer area [159] (A_{he})	0.97	m^2
	Time (t)	10	s
	Specific heat at constant pressure of exhaust gas (c_p) [158] [Assuming exhaust gas has same properties as air]	1.03	kJ/kg.K
	Air-fuel ratio (AFR)	15	-
	Gear box efficiency (η_{GB})	0.98	-
	Ambient pressure (p_{amb})	96	kPa
Variables	Average diesel substitution ratio (DSR)	95	%
	Average torque from ICE (Tq_{ICE})	595.5	Nm
	Average torque from WHR (Tq_{ORC})	32.6	Nm
	Average temperature of ICE wall (T_{Wall}^{ICE})	485	K
	Average ambient temperature (T_{amb})	281.3	K
	Average temperature of the exhaust gas before WHR ($T_{exh}^{WHR,in} = T_{exh}^{tb,out}$)	872.4	K
	Average temperature of the exhaust gas after WHR ($T_{exh}^{WHR,out}$)	524.7	K
	Average pressure of the exhaust gas before WHR ($p_{exh}^{WHR,in} = p_{exh}^{tb,out}$)	97.2	kPa
	Average pressure of the exhaust gas after WHR ($p_{exh}^{WHR,out}$)	97.2	kPa
	Average pressure of the intake air out of the compressor ($p_{int}^{c,out}$)	115.7	kPa
	Average temperature of intake air out of the compressor ($T_{int}^{c,out}$)	294.3	K
	Average temperature of the exhaust gas out of the ICE ($T_{exh}^{tb,in}$)	951.5	K
	Average pressure of the exhaust gas out of the ICE ($p_{exh}^{tb,in}$)	139.7	kPa
	Cumulative heat lost from the ORC (Q_{Lost})	0.11	MJ
	Cumulative heat input to the ORC (Q_{ORC})	0.21	MJ
	Average arithmetic mean temperature of the ORC condenser ($T_{con,m}$)	315	K
	Average arithmetic mean temperature of the ORC evaporator ($T_{ev,m}$)	465	K
	Mass of the fuel consumed by the ICE (m_{Fuel})	38.3	g

Appendix C

PhD Publications

C.1 Peer Reviewed Journal Papers

C.1.1 Published Journal Papers

† C. R. Reddy, V. B. Vinhaes, J. D. Naber, R. D. Robinett, M. Shahbakhti., "Model Predictive Control of a Dual Fuel Engine Integrated with Waste Heat Recovery used for Electric Power in Buildings", 20 pages, *Optimal Control Applications and Methods*, 2022. (Ref. [8])

† C. Reddy, M. Shahbakhti, R. Robinett, M. Razmara, "Exergy-wise Predictive Control Framework for Optimal Performance of MicroCSP Systems for HVAC

Applications in Buildings", *Energy Conversion and Management*, Vol. 210, 15 pages, 2020. (Ref. [5])

† M. Toub, C. R. Reddy, R. D. Robinett III, M. Shahbakhti, "Integration and Optimal Control of MicroCSP with Building HVAC Systems: Review & Future Directions", *Energies*, Vol. 14, Issue 3, 41 pages, 2021. (Ref. [6])

† M. Toub, C. Reddy, M. Razmara, M. Shahbakhti, R. Robinett, G. Aniba, "Model-Based Predictive Control for Optimal MicroCSP Operation Integrated with Building HVAC Systems", *Energy Conversion and Management*, Vol. 199, 16 pages, 2019. (Ref. [3])

C.1.2   Journal Paper in Preparation

† C. R. Reddy, V. B. Vinhaes, J. D. Naber, R. D. Robinett, M. Shahbakhti., "Exergy Based Model Predictive Control of a Dual Fuel Engine Integrated with Waste Heat Recovery". Prepared for *Control Engineering Practice.*

C.2   Refereed Conference Papers

† C. R. Reddy, V. B. Vinhaes, R. D. Robinett III, J. D. Naber, M. Shahbakhti "Model Predictive Control of a Waste Heat Recovery System Integrated with a

Dual Fuel Natural Gas-Diesel Engine", American Control Conference, 6 pages (pp. 1842-1847), May 26-28, 2021, New Orleans, LA, USA. (Ref. [7])

† C. Reddy, M. Razmara, M. Shahbakhti, R. Robinett, "Optimal Exergy-wise Predictive Control for a Combined MicroCSP and HVAC System in a Building", American Control Conference, 6 pages (pp. 235-240), Jul. 10-12, 2019, Philadelphia, PA, USA. (Ref. [4])

† C. R. Reddy, M. Toub, M. Razmara, M. Shahbakhti, R. D. Robinett III, G. Aniba, "Modeling and Optimal Control of Micro-CSP and a Building HVAC System to Minimize Electricity Cost", ASME 2018 Dynamic Systems and Control Conference, 10 pages, Sep. 30 - Oct. 3, 2018, Atlanta, GA, USA. (Ref. [2])

† M. Toub, C. R. Reddy, M. Razmara, M. Shahbakhti, R. D. Robinett III, G. Aniba, "Model Predictive Control for MicoCSP Integration into a Building HVAC System", 14th IEEE International Conference on Control and Automation, 6 pages (pp. 890-895), Jun. 12-15, 2018, Anchorage, AK, USA. (Ref. [1])

Appendix D

Program and Data File Summary

D.1   Chapter 1

Table D.1

Chapter 1 figure files.

File name	File description
ICE_Energy.pdf	Figure 1.1
ICE_Energy1.pdf	Figure 1.1
hot.pdf	Figure 1.3
cold.pdf	Figure 1.3
hotcold1.pdf	Figure 1.3
hotcold2.pdf	Figure 1.3
DissertationArea_ICE.pdf	Figure 1.4
DissertationArea_MPC0.pdf	Figure 1.5
DissertationArea_MPC.pdf	Figure 1.5
Thesis_organization.vsdx	Figure 1.7

D.2 Chapter 2

Table D.2

Chapter 2 figure files.

File name	File description
System.svg	Figure 2.1
PTC_Validation	Figure 2.2
ORC_Schematic.svg	Figure 2.3
ORC_rp.fig	Figure 2.4
MPC_Structure_Energy_CSP.pdf	Figure 2.5
Solar_Input.pdf	Figure 2.6
rbc11.pdf	Figure 2.7
rbc12.pdf	Figure 2.7
rbc13.pdf	Figure 2.7
rbc14.pdf	Figure 2.7
rbc15.pdf	Figure 2.7
ce11.pdf	Figure 2.8
ce12.pdf	Figure 2.8
ce13.pdf	Figure 2.8
ce14.pdf	Figure 2.8
ce15.pdf	Figure 2.8
cc11.pdf	Figure 2.9
cc12.pdf	Figure 2.9
cc13.pdf	Figure 2.9
cc14.pdf	Figure 2.9
cc15.pdf	Figure 2.9
TES_Sizing.pdf	Figure 2.10
Fig_RBC_MC_e.pdf	Figure 2.11
Fig_RBC_MC_c.pdf	Figure 2.11
MPC_Structure.svg	Figure 2.12
Sample_Day_Cold_Sunny.fig	Figure 2.13
RBC_Cold_Sunny.fig	Figure 2.14
MPC_Ex_Cold_Sunny.fig	Figure 2.15
SankeyDiagram_CSP_v2.vsd	Figure 2.16
Sizing.fig	Figure 2.17
MCS_Daily.fig	Figure 2.18
MCS_Seasonal.fig	Figure 2.19

Table D.3

Chapter 2 data files.

File name	File description
Disturbance_Matrix_21_March_2015.mat	Experimental temperature data
Building_Other_Load	Electrity consumption
Dyn_Pricing.xls	LMP
Houghton_2016.xlsx	Sample day measurements
Houghton_ProductionV4.mat	PTC output

Table D.4

Chapter 2 MATLAB scripts and SIMULINK models.

File name	File description
RuleBased_HVAC_18_March_2016.m	Script to run RBC
Optimal_Energy.m	Script to run EMPC
Optimal_Cost.m	Script to run CMPC
Optimal_Exergy.m	Script to run XMPC

D.3 Chapter 3

Table D.5

Chapter 3 figure files.

File name	File description
ICE_Schematic.pptx	Figure 3.2
Engine_test_bed.pptx	Figure 3.2
Test_Bed.pptx	Figure 3.3
Eng_SS.fig	Figure 3.4
Eng_Transient.fig	Figure 3.5
Control_Structure_EMPC_Automotive.pdf	Figure 3.6
Tq_Dem_EMPC_Automotive.pdf	Figure 3.7
Control_Output_EMPC_Automotive.pdf	Figure 3.8
Plant_Output_EMPC_Automotive.pdf	Figure 3.9
Control_Outputs_Dy_T_EMPC_Automotive.pdf	Figure 3.10
Control_Structure.pptx	Figure 3.11
RBC.pptx	Figure 3.12
Power_tracking.fig	Figure 3.13
Control_Output.fig	Figure 3.14
Plant_Output.fig	Figure 3.15
Control_Output_2.fig	Figure 3.16
Sankey_RBC_ICE.pdf	Figure 3.17
Sankey_RBC_ICE_WHR.pdf	Figure 3.17
Sankey_MPC_ICE_WHR.pdf	Figure 3.17
Structure_XMPC_ICE.pptx	Figure 3.18
XMPC_ICE_RBC.pptx	Figure 3.19
XMPC_ICE_ModelInput.fig	Figure 3.20
XMPC_ICE_ControlOutput.fig	Figure 3.21
XMPC_ICE_PlantOutput.fig	Figure 3.22
XMPC_ICE_PlantOutput2.fig	Figure 3.23
XMPC_ICE_Sankey_Energy.pdf	Figure 3.24
XMPC_ICE_Sankey_Exergy.pdf	Figure 3.24

Table D.6

Chapter 3 engine measurement files.

File name
DOE.Dual.Fuel.Engine.Test.Results.20190929.xlsx
DOE.Dual.Fuel.Engine.Test.Results.20191004.xlsx
DOE.Dual.Fuel.Engine.Test.Results.20191115.xlsx
1123.log
1123.csv
1145.log
1145.csv
1155.log
1155.csv
1200.log
1200.csv

Table D.7

Chapter 3 MATLAB scripts and SIMULINK models.

File name	File description
SS_fit.slx	Model Validation
Transient1.slx	Model Validation
Transient2.slx	Model Validation
ICE_Project_RBC.slx	Model to simulate RBC for ICE only
WHR_Project_RBC.slx	Model to simulate RBC for ICE + WHR
WHR_Project_EMPC.slx	Model to simulate EMPC for ICE + WHR
WHR_Project_XMPC.slx	Model to simulate XMPC for ICE + WHR
SlowestEMPCController.m	Script with EMPC formulation
SlowestXMPCController.m	Script with XMPC formulation

Appendix E

Letters of Permission

Model Predictive Control for MicroCSP Integration into a Building HVAC System

Requesting permission to reuse content from an IEEE publication

Conference Proceedings:
2018 IEEE 14th International Conference on Control and Automation (ICCA)

Author: Mohamed Toub

Publisher: IEEE

Date: June 2018

Copyright © 2018, IEEE

Figure E.1: Permission For [1].

RE: Author permission to reuse a ASME DSCC 2018 conference article for my PhD dissertation

Beth Darchi <DarchiB@asme.org>   Tue, Dec 7, 2021 at 3:05 PM
To: chethan reddy <chethan.reddy@gmail.com>

Dear Mr. Reddy,

It is our pleasure to grant you permission to use **all or any part of** the following ASME paper "Modeling and Optimal Control of Micro-CSP and a Building HVAC System to Minimize Electricity Cost," by Chethan R. Reddy, Mohamed Toub, Meysam Razmara, Mahdi Shahbakhti, Rush D. Robinett, III, Ghassane Aniba, Paper No: DSCC2018-9131, cited in your letter for inclusion in a PhD dissertation entitled Modeling and Optimal Control of Micro-CSP and a Building HVAC System to Minimize Electricity Cost to be published by Michigan Technological University.

Permission is granted for the specific use as stated herein and does not permit further use of the materials without proper authorization. Proper attribution must be made to the author(s) of the materials.   **Please note**: if any or all of the figures and/or Tables are of another source, permission should be granted from that outside source or include the reference of the original source. ASME does not grant permission for outside source material that may be referenced in the ASME works.

As is customary, we request that you ensure full acknowledgment of this material, the author(s), source and ASME as original publisher.

Many thanks for your interest in ASME publications.

Sincerely,

Beth Darchi

Publishing Administrator

ASME

2 Park Avenue

New York, NY 10016-5990

Figure E.2: Permission For [2].
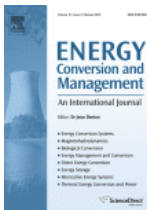
Model-based predictive control for optimal MicroCSP operation integrated with building HVAC systems

Author:
Mohamed Toub,Chethan R. Reddy,Meysam Razmara,Mahdi Shahbakhti,Rush D. Robinett,Ghassane Aniba

Publication: Energy Conversion and Management

Publisher: Elsevier

Date: 1 November 2019

Journal Author Rights

BACK   CLOSE WINDOW

Figure E.3: Permission For [3].

Figure E.4: Permission For [4].

215

Figure E.5: Permission For [5].

Figure E.6: Permission For [6].

Figure E.7: Permission For [7].

WILEY (/en-us)   🔍

Author of Work

As an author, you have certain legal rights to access and re-use your own work. For more information on publishing with Wiley, visit our Author Services site.

WILEY AUTHOR SERVICES →

To learn more about permissions requirements for self-archiving or depositing an article in an institutional repository, visit our Permissions information page.

ARTICLE REPOSITORIES →

Reuse My Published Work

As a Wiley author, you retain certain reuse rights when you sign your Copyright Transfer Agreement (CTA). Refer back to this agreement if you are seeking permission to:

- Republish an extract of your own published work.
- Include your article in your thesis.
- Use copies for your internal teaching purposes.

If you still require a formal permission license, please make the request through RightsLink and select "author of this Wiley work" and your appropriate reuse rights to download your license.

HOW TO MAKE A REQUEST →

If you are seeking permission for content that is not hosted on Wiley Online Library, you may still be able to license rights through CCC Marketplace.

START YOUR SEARCH HERE ▶(https://marketplace.copyright.com/rs-ui-web/mp)

Figure E.8: Permission For [8].

218